12-2007

Fabrication and a Study on the Wetting Properties of Nanostructured Surfaces

Meenaa Kalyanaraman
University of Tennessee - Knoxville

To the Graduate Council:

I am submitting herewith a thesis written by Meenaa Kalyanaraman entitled "Fabrication and a Study on the Wetting Properties of Nanostructured Surfaces." I have examined the final electronic copy of this thesis for form and content and recommend that it be accepted in partial fulfillment of the requirements for the degree of Master of Science, with a major in Electrical Engineering.

Jayne Wu, Major Professor

We have read this thesis and recommend its acceptance:

Brian R. D'Urso, John T. Simpson

Accepted for the Council:
Carolyn R. Hodges

Vice Provost and Dean of the Graduate School

(Original signatures are on file with official student records.)

To the Graduate Council:

I am submitting herewith a thesis written by Meenaa Kalyanaraman entitled "Fabrication and a Study on the Wetting Properties of Nanostructured Surfaces". I have examined the final electronic copy of this thesis for form and content and recommend that it be accepted in partial fulfillment of the requirements for the degree of Master of Science, with a major in Electrical Engineering.

Jayne Wu

Major Professor

We have read this thesis and
recommend its acceptance:

Brian R. D'Urso

John T. Simpson

Accepted for the Council:

Carolyn R. Hodges

Vice Provost and Dean of the
Graduate School

(Original signatures are on file with official student records.)

FABRICATION AND A STUDY OF THE WETTING PROPERTIES OF NANOSTRUCTURED SURFACES

A Thesis

Presented for the

Master of Science

Degree

The University of Tennessee, Knoxville

Meenaa Kalyanaraman

December 2007

Dedication

This thesis is dedicated to my husband Janak, my parents Kalyanaraman and Lalitha and my sisters Sukanya and Sowmya for their endless love and support.

Acknowledgements

None of this thesis work would have been possible without the complete guidance and support of my advisor Dr. Brian R. D'Urso. I am greatly indebted to my advisor for accepting me into his group and providing academic and financial assistantship through the course of my graduate studies. I would like to thank him for all his valuable explanations, which always had great clarity and depth, and innumerable ideas he provided while I was still learning and understanding concepts in my research. I am also thankful for his patience and support while teaching me the various experimental work involved in my thesis. He has provided me a lot of inspiration both through his own exceptional scientific abilities as well as in precisely guiding and mentoring me.

I would like to express my sincere thanks to Dr. John T. Simpson for providing me guidance and encouragement through the course of my study of superhydrophobic behavior at Oak Ridge National Labs. I have thoroughly enjoyed and benefited from all the useful discussions with him and am very grateful to him for giving me the learning experience. I would also like to express my sincere thanks to Dr. Jayne Wu for her valuable suggestions during my thesis. I am thankful to her for patiently reviewing the progress of my thesis and for teaching a course on nanotechnology, which was very useful and enjoyable. I am very thankful to Charles R. Schaich for his great work on the tools required for the drawing experiments. I am very thankful to Boyd M. Evans for the immense help he provided with the vapor deposition and the evaporation processes for the electrowetting experiments that could not have been done without his support. I am also thankful to Daniel Schaeffer for helping and giving good company through all the drawing, etching and SEM sessions.

I am grateful to my husband Janak for his unconditional love and support as well as his constant involvement in my progress towards a Master's degree. I am also thankful to my parents and sisters for encouraging in me, the freedom of choice and belief. Lastly, I would also like to thank all my friends from India who have always played a great role in my life. Sharing with them, an interest towards academics and an appreciation for art and music, has always kept me jubilant and motivated.

Abstract

Fluid behavior at the microscale exhibits large surface to volume ratios increasing the significance of interfacial phenomena. We have studied two microfluidic phenomena that utilize interplay between microstructure and chemical composition. The first one causes liquid droplets to roll off from surfaces with a very high contact angle. This phenomenon is called superhydrophobic behavior, can be controlled by several tuning parameters. The second one changes the wettability of liquids on a dielectric coated surface with electric potential. The experimental studies were done by first fabricating an ordered array of glass nanocones. Fiber drawing and differential glass etching processes were used to produce cone like structures with lattice constant of 40 μm down to 1.6 μm. The superhydrophobic behavior was first studied and modeled in a series of nanocone wafers of increasing aspect ratio from .3 to 15. The characterization was done by the measurement of the contact and rolling angles. The Wenzel to Cassie transition of wetting states was observed. The contact angles were calculated by using the 'axisymmetric drop shape analysis' approach. Next, the study of the electrowetting behavior of two broad categories of structured surfaces was done. One was a low aspect ratio surface exhibiting Wenzel wetting and the other was a high aspect ratio surface exhibiting Cassie wetting. The device for experimental study was prepared by coating additional layers, which included conductive gold and dielectric Parylene-C coatings. Studies were done using silicone oil and air as the ambient medium. Images of drops were taken at different voltages and the contact angles were calculated geometrically. Electrowetting on nanocone arrays was modeled using an energy-based approach and the obtained theoretical curves were compared to the experimental ones. Oil helped in achieving a large contact angle change. A qualitative analysis of the electrowetting properties of the surfaces was done based on the voltage-contact angle curves.

Table of Contents

List of Tables

List of Figures

List of Abbreviations

MEMS – Microelectromechanical Systems

BHF – Buffered Hydrofluoric Acid

DHF – Dilute Hydrofluoric Acid

CVD – Chemical Vapor Deposition

EW – Electrowetting

EDL – Electrical Double Layer

EWOD – Electrowetting on Dielectric

SEM – Scanning Electron Microscope

PECVD – Plasma Enhanced Chemical Vapor Deposition

HFCVD – High Flux Chemical Vapor Deposition

RIE – Reactive Ion Etching

OD – Outer Diameter

ID – Inner Diameter

SAM – Self-Assembled Monolayer

DEP – Dielectrophoresis

EO – Electro-osmosis

Chapter 1
Introduction

Motivation

Nature, over several billions of years of evolution by natural selection has presented itself as an amazing system in a constant trend of optimization. From a macroscopic scale down to molecular level biological structures have exhibited some very interesting properties. Studies from systematically ordered matter in a nanometer scale in biological systems have always been of great technological and scientific significance. One such revolution is based on the organization and control of matter on the nanometer scale. An example in a biological level is a protein, which is 1 to 20 nm in size.

The objective of achieving functionality at such a length-scale can be attributed to several factors. One of the factors relevant to this thesis is achieving very high surface areas and the other is handling the increased relative significance of properties like surface tension, diffusion, viscosity and local electrical effects compared to macroscopic entities. Apart from just scaling down the size, topography, which is specified here by the aspect ratio of surface features, is a critical factor in fabricating high surface area nanostructures.

Fabricating high aspect ratio features has been a limiting factor in the more popular and easily implementable MEMS lithography technologies. Several other methods have been put forward (which will be discussed in the next section) for producing vertically projecting features in a controlled manner. A good understanding of the properties of glass made it a suitable raw

material for such a nanofabrication process. The main properties of glass, which stand out in context of this thesis, are its excellent homogeneity in a variety of forms and sizes, and the flexibility of introducing variation in chemical composition. Glass proved to be an excellent material of choice for gaining control over the principal factors like feature size, uniformity and aspect ratio. The fabricated glass-based devices with aptly tuned parameters were extensively tested for the possibility of having finely tunable wetting properties. The property comes from twenty-five year old nature inspired SEM studies of water repellant outer plant surfaces, which revealed amazing microstructural diversity. The studies resulted in a theoretically well-accounted connection between the roughness of a surface and its repellency to water.

A similar connection was established in the thesis between the fabricated nanostructures and the resulting superhydrophobic behavior in them. Several randomly rough surfaces can be crudely made but a good control over its morphology is difficult to attain. For a surface that comes with micro/nano protrusions of similar shapes and dimensions that are regularly spaced the controllability is very well enhanced. This can be seen both in a fabrication as well as in a characterization point of view. Silicon micromachining is commonly used to produce such micro protrusions but for a glass based composite surface anisotropic wet chemical etching was the most effective in terms of time, cost effectiveness and controllability. The ease of controlling the aspect ratio through the etching process and the reproducibility of the process helped in the study of the correlation of the feature–defined parameters to the wettability-defined ones. The feature-defined parameters were governed by the nature of the fabrication and the etching process. The wettability-defined parameters were based on principles of interfacial free energies and the resulting contact angles of the water droplets.

The next step was in studying a similar correlation but with a different approach. The goal here was to dynamically adjust the same interfacial energies of a given water repellant surface unlike the previous case which used a slightly altered fabrication sequence to produce devices that repelled water to different degrees. The approach was based on an interfacial electrical phenomenon that causes redistribution of charges in an interface when an electrical potential is applied between the droplet sitting on a surface and an electrode underlying a dielectric layer. Electrowetting seemed to be an advantageous method of control especially on structured rough surfaces due to the bigger range of control they offer. A simple study on the general nature of the electrowetitng behavior of hydrophobic to superhydrophobic surfaces was carried out.

Organization and Summary of Thesis

This thesis has three broad sections. A literature review is given in the introduction of each chapter referencing the related work.

- The second chapter discusses the fabrication process of the nanocone glass surfaces. The fabrication involves glass drawing; bundling and redrawing processes until features of desired dimensions are obtained. The fabrication is followed by characterization of the etching process. The activities of the constituent ions of the etching solutions are calculated and a relationship is established between the solution concentration and the etch rate contrast of the core and the cladding glass. The dependence of the aspect ratio of the nanocones on the type of etching solution is analyzed.

- The third chapter discusses the superhydrophobic properties of the nanocone glass surfaces. A series of wafers etched to different aspect ratios are treated with a hydrophobic silane and tested for superhydrophobicity. A goniometric experimental setup is employed to image the advancing and receding contact angles of water drops dispensed on the surface of the wafers. An "axisymmetric drop shape analysis" approach is employed to calculate the contact angles of the drops. The rolling angles of the wafers are also measured. A relationship is established between the contact angles and the aspect ratio. A sharp transition of the wetting regime of the surface from "Wenzel" to "Cassie" as the aspect ratio is increased is also observed.

- The fourth chapter discusses the electrowetting behavior of similarly fabricated structures. The wafers are first prepared for the "electrowetting on dielectric" experiment by coating a conductive layer followed by a dielectric coating. An e-beam evaporation process deposits the gold layer and the Parylene-C dielectric is coated by vapor deposition. A low aspect ratio (which is treated as a surface that falls under the Wenzel wetting regime), a high aspect ratio (which is treated as a surface that falls under the Cassie wetting regime) and a plane surface are the test devices on which the experiments are performed. The theoretical evaluations for a voltage driven droplet on the various surfaces are done based on an energy minimization approach. The role of surface geometry and the effect of oil as the ambient medium around the droplet are also evaluated. Analyzing the voltage-current curves and the

voltage-contact angle curves of the droplet helped in the characterization of the wetting behavior. A qualitative comparison of the dynamic wetting behavior of the surfaces is done based on the electrowetting parameters.

- The final chapter briefly discusses the possible applications of the various results and the future work.

Chapter 2
Fabrication of Nanocone Glass Arrays

Background

Literature Review

In this thesis work nanocone glass arrays were fabricated using a glass drawing and differential etching process [1.1]. The fabrication technique of drawing, bundling and redrawing dissimilar glasses that show an etch rate contrast was inspired by the work on nanochannel array glass [1.2]. A similar manufacturing technology based on a glass drawing and differential etching process is present in the work on microchannel plate detectors [1.3]. The main difference between the nanochannel array glass and the fabrication process discussed in this chapter is the reversed degrees of etchability of the core and cladding glass and the different types of glasses used. Several works have been reported in fabricating vertically projecting sharp features in the nanometric scale and the challenge has been in gaining control over feature parameters like aspect ratio, tip sharpness, lattice spacing and alignment. Arrays of molybdenum cones with a height of 1.5 μm, lattice spacing of 12.7 μm and a tip radius of about 500 Å have been produced to serve as thin film field emission cathodes [1.4]. For a similar field emission application, vertically aligned carbon nanotubes were grown by a PECVD process [1.5]. A silicon-based focused ion beam milling process followed by a HFCVD process has also been used in producing diamond tips with an aspect ratio of 7.5 and a tip radius as small as 50 nm [1.6]. Sharp cones that are 40 μm tall have also been produced in silicon by a femtosecond laser irradiation [1.7]. Another work based on femtosecond laser irradiation is used controlled laser spot diameters to produces surfaces in silicon ranging from 30 μm - 250 μm in size [1.8]. An RIE - based 'Black Silicon' method has

also been introduced to produce high aspect ratio trenches in silicon and polymer [1.9]. Needle-like structures, which are 1 μm - 2μm tall and with a pitch of .5 μm - 1μm have been fabricated by a similar black silicon method [1.10]. Silicon and Germanium nanocones were fabricated by a metal-catalyzed CVD process where the apex angles were tuned by the catalyst size used [1.11].

A pair of alkali borosilicate glasses was used as the raw materials for the fabrication process. For a borosilicate glass the glassformer ratio (SiO_2: B_2O_3) has a direct implication on certain properties of the glass. It has been shown that the type, degree, rapidity and the final phase composition be determined by the temperature of heat treatment and the composition of the original glass [1.12, 1.13, 1.14, 1.15]. The drawn and fused glass bundle was sliced and etched to produce the nanocones. HF was used as the etching solution as it readily attacks glass. A very detailed review on wet chemical etching of silicate glasses in hydrofluoric acid based solutions has been reported [1.16]. A similar report on the mechanism of etching of SiO_2 with hydrofluoric acid has been reported [1.17]. In this chapter the etching mechanism is characterized by comparing the constituent ion activities of the etching solution with two parameters. One is the etch rate contrast of the two glasses and the other is the aspect ratio of the nanocones. An approach for analyzing the fluoride compositions of solutions with specific ranges of formal concentrations have from the activities of the solution species has been reported [1.18, 1.19].

The fabricated nanocone arrays have many possible applications. One of it has been to produce a tunable range of superhydrophobic surfaces [1.20].

Significant glass properties for the fabrication process

A careful analysis is required on the glasses for the drawing, fusion and etching process. There are several physical and chemical properties of glass, which have to be understood before making the right choice for fabrication. Most of the information in the following sections were obtained from textbooks on glass properties [1.21].

Definition

Glass is defined as an amorphous solid completely lacking in long-range periodic atomic structure and exhibiting a region of glass transformation behavior. It is formed by cooling a liquid, which is at a temperature well above the melting temperature of that substance down to a temperature below its melting temperature without crystallization.

Glass Melting

The glass making procedure involves selection of raw materials, calculation of the relative proportions of each to use in the batch, and weighing and mixing these materials to provide a homogeneous starting material. During the initial heating process these raw materials undergo a series of physical and chemical changes to produce the melt. The main batch material used to produce a specific type of glass is the glass former. This serves the primary source of structure. Glass formers in commercial oxide glasses are silica, boric oxide and phosphoric oxide that readily form single component glasses. A large number of several other compounds may also act as glassformers under certain circumstances. With the exception of germanium dioxide these oxides do not form glasses by themselves unless very rapidly quenched or vapor deposited, but can serve as glassformers when mixed with other oxides. A vast number of commercial glasses are based on silica. Due to the high melting temperature (>2000ºC) required to produce vitreous silica, production of silicate glasses requires the addition of a flux that serves to reduce the processing temperature to within practical limits. The most common fluxes are the alkali oxides like sodium oxide and lead oxide. Excessive addition of alkali oxides can result in serious degradation of glass. This is usually countered by the addition of property modifiers like alkaline earth and transition metal oxides and most importantly aluminum oxide. The glass transformation process is illustrated in *Fig. 1.1*.

Immiscibility

Phase separation due to the liquid-liquid immiscibility of glass melts is a common phenomenon. This separation of melts into two liquid phases can be explained by the behavior of the free energy of the system.

$\mathbf{\Delta G_m = \Delta H_m - T\Delta S_m}$

$= \alpha X_1 X_2 - T (- R [X_1 \ln X_1 + X_2 \ln X_2])$

$= \alpha X_1 X_2 + TR [X_1 \ln X_1 + X_2 \ln X_2],$

ΔH_m - enthalpy of mixing, ΔS_m - entropy of mixing, ΔG_m - free energy of the system

X_1 - concentration expressed as a mole fraction of phase 1, X_2 - concentration expressed as a mole fraction of phase 2, α - a constant related to the energies of the bonds among the various components, R - gas constant

Since X_1 and X_2 are fractions the term inside the brackets will always be negative. Therefore ΔG_m will be positive or negative based on the value of α. If α is negative ΔG_m will also be

negative with minimum at $X_1 = X_2$ and the system will not exhibit phase separation. However if α is positive the will be competition between the contributions of enthalpy and entropy of mixing and the sign on ΔG_m will be a function of temperature. At T = 0K the entropy term will be 0 and the free energy would be positive, resulting in phase separation if allowed by kinetics. At sufficiently high temperature, usually designated as the critical temperature T_c, the entropy term would dominate resulting in negative free energy and a homogeneous melt. Between 0 and T_c, competition between enthalpy and entropy results in a curve. Stable immiscibility occurs when glasses separate into two or more distinct phases above the critical temperature resulting in the glass showing distinct layers of different composition or milkiness under cooling *(Fig. 1.2)*. Metastable immiscibility occurs at temperatures below the critical temperature.

In the fabrication process that we discuss in this chapter glass phase separation plays a crucial role which will be discussed in detail in a later section.

Viscosity

Viscosity is a measure of resistance of a liquid to shear deformation.

V = F*d/A*v,

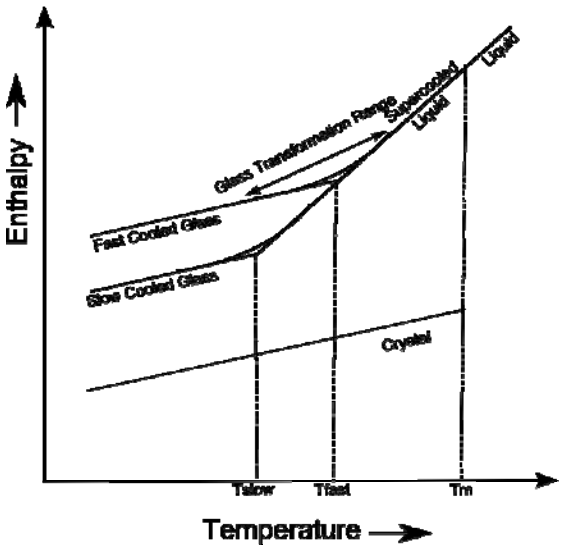

Fig. 1.1 – Temperature-Enthalpy relation - A glass transformation process

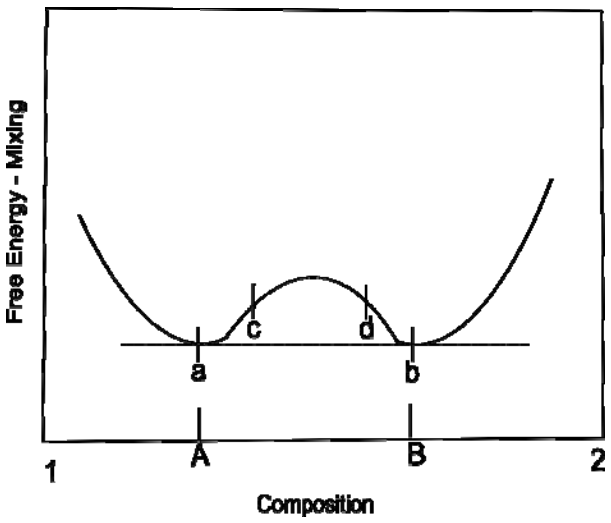

Fig. 1.2 - Composition and Free Energy - A binary immiscible system

F = tangential force applied to two parallel planes, A = area of the planes, d = distance between the planes, v = relative velocity of the two planes, V = Viscosity

Viscosity is useful in controlling the ease of glass formation and also important in determining the melting conditions necessary to form a bubble free homogeneous melt, the temperature of annealing to remove the internal stresses, and the temperature range used to form commercial products.

Temperature – Viscosity cycle

The section below discusses a range of temperatures and corresponding viscosities as the glass goes through the softening process (Fig 1.3). The viscosities given are for a soda-lime melt.

Melting Point - Temperature at which a typical melt is obtained with fining and homogeneity (Viscosity – 1-10 Pa s).

Working Point - Temperature at which the melt is delivered to a processing device (Viscosity – 10^3 Pa s).

Softening Point - Temperature at which the melt ceases to prevent its deformation under its own weight (Viscosity – $10^{6.6}$ Pa s).

Dilatometric Softening Point - Temperature at which the sample reaches the maximum length in a length versus temperature curve during heating of a glass (Viscosity – 10^8–10^9 Pa s).

Annealing Point - Temperature at which the stress is substantially relieved for a few minutes (Viscosity – 10^{12}–$10^{12.4}$ Pa s).

Strain Point = Temperature at which the stress is substantially relieved for several hours (Viscosity – $10^{13.5}$ Pa s).

Viscosity of the melt can be affected by several factors like temperature, composition, thermal history, phase separation and crystallization.

Thermal Expansion

The thermal expansion coefficient of a material is a measure of the rate of change of volume and therefore density with temperature.

The linear thermal expansion coefficient is defined as

$\alpha_L = (dL/dT)_p/L$

L = length of the sample

T = specified temperature

$(dL/dT)_p$ = slope of the curve at constant pressure

The thermal expansion curve for a glass indicates three important pieces of information: the thermal expansion coefficient, the glass transition temperature and the dilatometric softening temperature. Each of these properties is a strong function of glass composition. Thermal expansion coefficients of glasses with a few exceptions increase with increasing temperature. Vitreous silica and few other fully linked network glasses display negative thermal expansion coefficients over a limited temperature range. These glasses have high resistance to thermal shock. Addition of modifier ions to silica fills the small gaps preventing bond bending and hence increases the thermal expansion coefficient. The fabrication process of the nanocone arrays involves the drawing of two dissimilar glasses. The glasses must have similar coefficients of thermal expansion in order to survive together without stress development after melting and drawing together.

Diffusion

A number of properties of glass are controlled by diffusion. Diffusion or the transport of atoms or ions through a vitreous network is expressed in terms of the diffusion coefficient.

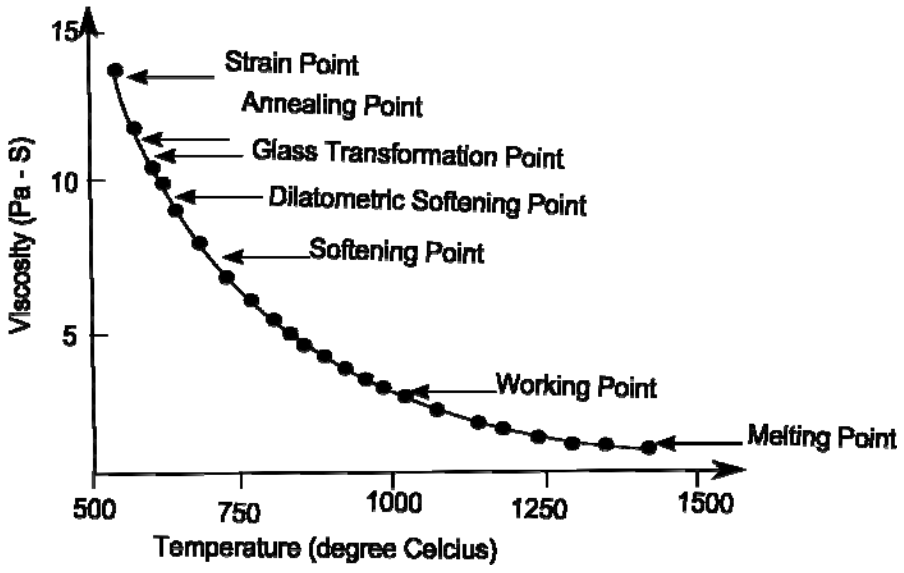

Fig. 1.3 - Viscosity Temperature relationship for Soda – Lime glass

$J = -D\partial c/\partial x$

J = flux of the diffusing species

$\partial c/\partial x$ = concentration gradient of the diffusing species in the direction x.

The majority of data for ionic diffusion deals with sodium whose diffusion coefficients in sodium silicate glasses increase with increasing sodium oxide concentrations.

Diffusion of an ion, which is a primary component of the glass, is referred to as self- diffusion. Inter diffusion or ion exchange occurs when a glass containing one mobile ion A is exposed to a source of a different mobile ion B. Ions from the glass diffuse out of the sample while ions from the source diffuse into the sample with different speeds in glass due to its different sizes. Since the faster ion will tend to outrun the slower ion an electric field will develop trying to accelerate the slower ion and slow down the faster ion until the fluxes of both the ions are identical.

The interdiffusion coefficient can be expressed as

$D = D_aD_b / (D_aC_a + D_bC_b)$,

D_a and D_b are the tracer diffusion coefficients of ions A and B and C_a and C_b are the fractional concentrations of ions A and B. Ion exchange can be used to alter the near surface properties of an existing glass and also to strengthen glasses in the near surface region. The interdiffusive nature of the borosilicate glasses was one of the limiting factors in achieving smaller and smaller regions of immiscibility. The fusion temperature of the drawn fibers and the desired feature size had to be carefully selected to preserve the features and avoid interdiffusion of the constituent ions from one region to the other to the other.

Chemical Durability

Silicate glasses are highly inert towards all liquids and gases at low temperatures (<300ºC) except hydrofluoric acid solutions and water. Ion exchange causes leaching of alkali ions from multicomponent silicate glasses leaving a surface layer on the glass depleted of these ions. Generally the composition of glassformers can affect the chemical durability of the glass. In this fabrication a pair of borosilicate glasses (Schott 8330 and Schott 8487) was used. The selection of the glasses was primarily based on the ratio of the glass formers (SiO_2: B_2O_3).

Alkali Borosilicate glasses

Since alkali borosilicate glasses seemed to have properties that suited the drawing and etching process they were used as the perform materials. This section briefly discusses alkali

borosilicate glasses and the technical properties of the two glasses that were used in the fabrication.

General Properties

Adding boron to the silica creates borosilicate glass. Adding alkali modifiers to borate glasses creates alkali borosilicate glasses. The two glassy phases of borosilicate glasses are the silica-rich and the borate phases. As mentioned earlier the type, degree, rapidity and the final phase composition be controlled by the temperature of heat treatment and the composition of the original glass [1.12, 1.13, 1.14, 1.15]. The final phase composition affects the etchability of the glasses. When an alkali oxide is added to a borosilicate glass it associates itself with the borate, silica or both. This can affect the resulting structure and hence the degree of phase separation. A sodium-lithium borosilicate system has shown increased phase separation when compared to a sodium-potassium borosilicate system. Addition of alumina reduces the phase separation. Pyrex is a phase alkali separated borosilicate glass. Its chemical durability is strongly dependent on its phase separation. If an interconnected microstructure of a chemically soluble phase is formed within a chemically durable phase then the more soluble phase will be preferentially attacked. This is the basic process behind the production of the microporous glass and the Vycor type processes. If a chemically durable phase is formed dispersed in a less durable phase then the resultant glass may have a lower durability over the parent glass whilst a lower durability phase disperse in a more durable phase would give an increased durability over the parent glass. Electrical conductivity depends on the diffusion of alkali ions under influence of electric field. It increases for glasses that separate to give an alkali rich matrix or an interconnected microstructure.

Technical Data

Two types of glasses are used glasses for the fabrication process. Duran® 8330 (*Table 1.1*) is manufactured by Schott glass and is available in tubes, capillaries, and rods. It has a low rate of thermal expansion and is resistant to corrosion.

Table 1.1 – Technical Data for Schott-8330 Glass

Property	**Value**
Thermal Coefficient of Expansion (0/300°C)	33 X 10^{-7}/°C
Transformation Temperature	525°C
Annealing Point	560°C
Softening Point	825°C
Strain Point	525°C
Working Point	1260°C
Density	2.23 g/cm^3
Poisson's Ratio	0.20
Refractive Index	1.473
Dielectric Constant	4.6
Hydrolytic Resistance	Class 1
Acid Resistance	Class 1 (High)
Alkali Resistance	Class 2
Chemical Composition (Main components in approx weight %)	SiO_2 (81%) B_2O_3(13%) Na_2O+K_2O(4%) Al_2O_3(2%)

Glass 8487 (*Table 1.2*) is manufactured by Schott glass has lower chemical durability and has a higher thermal expansion which makes it suitable for sealing with Tungsten.

Table 1.2 – Technical Data for Schott-8487 Glass

Property	**Value**
Thermal Coefficient of Expansion (0/300°C)	39 X 10^{-7}/°C
Transformation Temperature	525°C
Annealing Point	560°C
Softening Point	775°C
Working Point	1135°C
Density	2.25 g/cm^3
Refractive Index	1.479
Dielectric Constant	4.9
Hydrolytic Resistance	Class HGB4
Acid Resistance	Class S 3 (Low)
Alkali Resistance	Class A 3
Chemical Composition (Main components in approx weight %)	SiO_2 (75.5%) B_2O_3(16.5%) Na_2O+K_2O(1.5%) Al_2O_3(4%) CaO(.5%) MgO(.5%)

Fiber Fabrication

The Draw Tower

This section describes the draw tower and the drawing principle that is used to melt a rod of Schott-8330 glass (core) inside a tube of Schott-8487 glass (cladding) in the furnace, followed by drawing the molten glasses together into fibers. The fabrication methodology has been inspired by the nanochannel array glass [1.2].

Description

Advantek Engineering's custom engineered glass drawing tower was used to fabricate the required fibers. The drawing tower is based on a modular design. The main tower components included are a) the main structural frame b) computerized direct drive servo system with custom vacuum chucks for the feed c) 1100ºC oven with compact heat zones for maximum perform yield and very long life heating element d) 25 kg tractor draw system for the draw e) Zumbach laser micrometer system f) automatic carbide cutter g) computer automated touch control panel. A simple schematic (*Fig. 1.4*) and the technical data (*Table 1.3*) for the Advantek Engineering's glass drawing tower is given. The draw mechanism helps drawing fibers of relatively small dimensions with low to medium draw tension and fairly high draw speeds. Additionally a single stage dry scroll pump connects to the preform holder. A small laser micrometer stationed below the furnace measures the diameter of the fiber coming out of the furnace in real time. The cut fibers are collected in a grounded metal container to prevent the fibers from flying off due to static charge build up. The furnace temperature, feed rate, draw rate and preform dimensions can be programmed in through a touch control panel. The instantaneous fiber diameter, draw tension, preform-top position, and furnace temperature are indicated through the course of the drawing.

The Drawing Principle

The glass assembly consists typically of a rod in a tube perform which is suspended vertically above a cylindrical furnace into which it is slowly fed. A starting furnace temperature is set based on the kind of glass used. The two glasses used must have well matched thermal expansion coefficients to avoid stress build up and eventual breakage. The drawing process is relatively straightforward. Once the furnace reaches the preset temperature the glass softens and is pulled from below at a rate exceeding that of the feed. For a closed system like the furnace the ingoing preform feed mass must equal the out coming fiber mass. This implies a reduced cross sectional

area of the fiber, which is drawn faster than it is fed to allow for the increased length caused by the pull. This can be described mathematically and can be controlled by dictating the feed and the draw rates. Fibers of the desired diameters can be obtained by calculating the proper rates as a function of the desired reduction.

FS / DS = FA / PD → FS / DS = ($OD^2_{cladding} - ID^2_{cladding} + OD^2_{core}$)/ $OD^2_{fiber,}$

FS = feed speed in m/min - rate at which the preform is fed into the furnace, DS = draw speed in m/min – rate at which the fiber is pulled out of the furnace, PA = cross sectional area of the starting preform, FD = cross sectional area of the end fiber, OD = outer diameter, ID = inner diameter

Table 1.3 – Technical Specifications – Glass Draw Tower

Property	Value
Drawing Speed Range	.5-12 m/min
Feed Speed Range	.0005 – 1 m/min
Tower Height	3.6 m
Max. No. of Preforms	1
Max. Preform Length/ Diameter	1000/40 mm
Max. /Min. Fiber Diameter	18 / .2 mm
Draw Speed Accuracy	± .08%
Feed Speed Accuracy	± 0.0001 m/min
Max. Oven Temperature /Control after tuning	1100 / .25 ºC

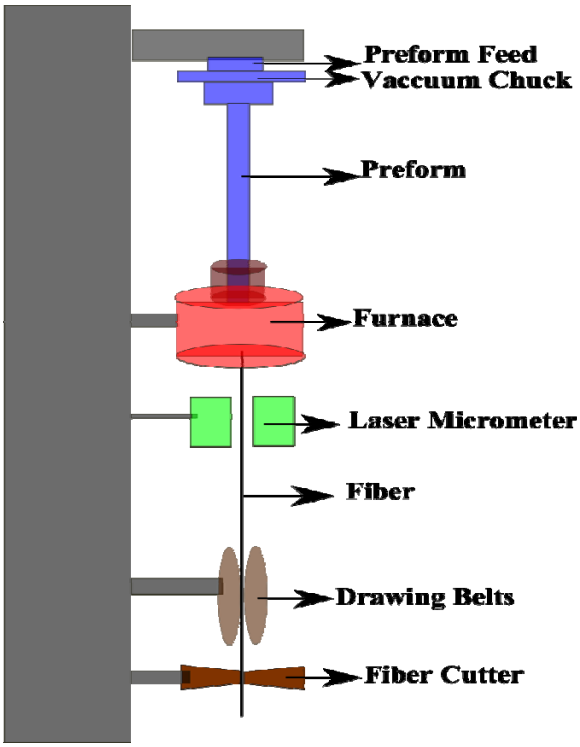

Fig. 1.4 – Functional Schematic of the Glass Draw Tower

The rod and tube dimensions, the desired target diameter and draw speed are fed into the control panel, which calculates the necessary feed speed. As the glass fiber comes out of the furnace it cools down by ambient air convection briefly before it reaches a pair of rubber belts whose speed directly control the draw rate. Manual draw speed adjustment can stabilize a fluctuating fiber diameter. If the diameter of the fiber increases above its target, the drawing speed is increased; if the fiber diameter starts falling below the target, the drawing speed is decreased. Heating the glass to a sufficient temperature that determines an optimal viscosity is the key to drawing glass as shown in *Fig. 1.5*.

The First Draw

The section below discusses each of the drawing steps that are implemented to attain feature sizes in a decremental fashion. The very first draw in this fabrication process always starts with a rod in tube preform. Following it each draw stage uses fibers from the previous draw, which are drawn together again to get scaled down features. The calculations for making rough estimates of the resulting feature sizes are also discussed.

Preform Preparation

The primary step in the glass drawing process is the preparation of the preform. The glasses chosen for the fabrication were a pair of borosilicate glasses. The technical specifications for the two glasses are given in the previous section. The glasses are thoroughly cleaned in an ultrasonic water bath. The core glass Schott 8330 serves as the rod and the cladding glass Schott 8487 serves as the tube. The rod in tube perform is prepared by using a set of clamps that tightly holds the glasses together. The vacuum fixtures help in providing sufficient clamping pressure to make sure the tubing does not fall when hung from the feed slide. The final perform as depicted in *Fig. 1.6* is attached directly to the preform holder of the draw tower.

Process

The final goal of every drawing process is to produce fibers of the desired size that are a good replication of the starting preform. In this draw two dissimilar glasses in the preform would form the core and cladding section in the final fiber. The preform is suspended in the draw tower. An adequate vacuum that helps close the interstitial spaces between the rod and the tube without affecting the size and shape of the fiber is necessary for uniformity. Very high temperatures can cause excessive softening and reduced viscosity making it hard to draw the fiber. Very low

temperature might increase the viscosity, which is again hard to draw. The tension on the drawing belts is a good indication of the viscosity of the glass that is being currently drawn.

Assembly

The temperature of the furnace is set above to the softening temperature of the glass, which is around 821ºC for Pyrex. The furnace heats up within a few minutes. The softened glass starts moving out of the furnace under gravity by stretching and forming an hourglass shape. The vacuum pump is activated and a minimal vacuum is maintained. This is sufficient for the sealing and stretching process of the glass that helps eliminating the gaps that may occur in the interface between the core and cladding. The fiber cutter is turned on and the laser micrometer is brought to position, the feed and draw process are started, and the out coming fiber is accommodated into the drawing assembly. A stabilized target fiber diameter and uniform features when looked in the optical microscope indicate equilibration.

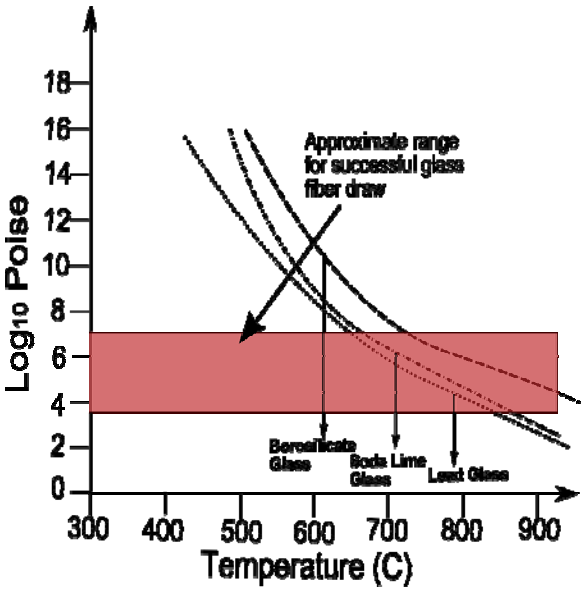

Fig. 1.5 – Optimal viscosity range for glass drawing

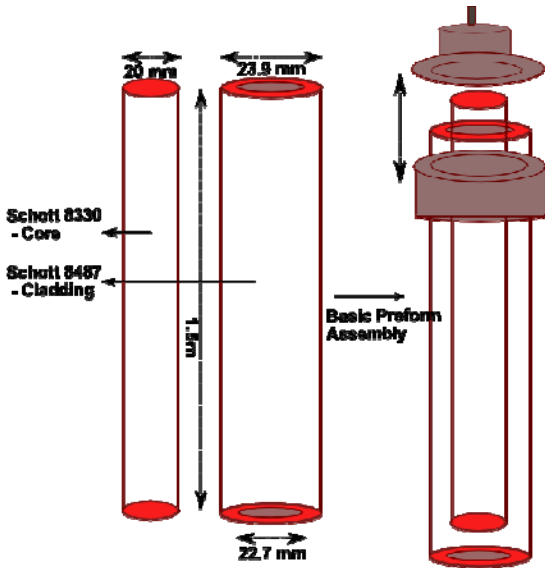

Fig. 1.6 – Preform assembly for the first draw

Typical Experiment Log

8: 50 am – Preform loaded. Staring preform position is 983.4 mm. Furnace set to 880 ºC. Iris partially closed.

9:25 am – Preform drops. Vacuum turned on (-5 inches of Hg). Feed started (Feed Speed = 7.247 mm/min). Draw started (Draw Speed = 8 m/min). Cutter turned on (Cut Length = 700 mm). Iris closed. Tension = .45 kg, Target Diameter = 1.08 mm, Yield ~ 1400 pieces of fiber

Calculations

Calculating the net reduction in surface area of the fibers when compared to the starting preform is a rough procedure for estimating the desired feature size. This indicates the required number of draws and the required target fiber diameters to reach to a desired lattice constant. Gaps in the perform collapse under vacuum and heat conditions during the drawing process thereby reduce the effective diameter. Hence the calculations in *Table 1.4* show the features sizes but are not exact.

Table1.4 - Approximate Feature Size Calculations

Draw No - Preform Type	Preform Diameter (mm)	Fiber Diameter (mm)	Feature Size (µm)	Surface Area ratio of Preform to Fiber	Lattice Constant (µm)
1 - Rod in Tube	Rod– 20.0 Tube– 23.9	1.08	903.75 (Core) 1080 (Cladding)	1:22.13	1080
2 – Hex Bundle	Bundle (End to End) – 25.4	1.154 (End to End)	41.06 (Core) 49.07 (Cladding)	1:22.01	49.07
3 – Hex Bundle	Bundle (End to End) – 25.4	1.016 (End to End)	1.64 (Core) 1.96 (Cladding)	1:25	1.96

The Second Draw

This section discusses the process of double drawing fibers in order to get down to a smaller feature size. It also discusses the hexagonal bundling process, which is crucial in getting a uniform array of features that are free of holes and gaps.

Bundling

In order to scale down to the required feature size the fibers are bundled together to make a preform for a second draw *(Fig. 1.7)*. The resulting lattice constant of the double drawn fibers would have to be approximately 40 μm. The chosen fibers for bundling were the best ones that were obtained after the complete equilibration of the draw under similar operating conditions and with minimally deviant diameters. The bundling was of hexagonal type and the resulting bundle was hexagonal in shape.

Packing Efficiency: Hexagonal close packing involves the stacking of fibers so that fibers in alternating layers overlie one another. Hexagonal packing provides maximal packing density. This holds for both circular fibers and hexagonal fibers. Dense packing helps in accommodating more number of fibers efficiently thereby eliminating gaps and non-uniformity.

Fiber area efficiency: The target diameter of the fibers used is chosen in the draw process so that an exact integer number can be accommodated in a hexagonal bundle of known size. They must also support easy manual bundling. Extremely thin fibers of sizes less than .5mm are very hard to bundle. A tradeoff on target feature size for a reasonable fiber thickness must be chosen for ease of bundling. Making the fiber diameter small also minimizes error due to small deviations in the fiber diameter. Apart from better packing density small fibers primarily help in getting to the desired small feature limit. Stacking of fibers is done carefully ensuring uniformity at every stage. This is achieved by periodic checks for gaps, missing fibers, short fibers, crossing fibers or rotated fiber domains.

Preform preparation

After the bundle is made it is prepared to serve as the preform for the second draw *(Fig. 1.8)*. One end section of the bundle is wrapped with Teflon tape. Metal clamps are attached to that portion thereby holding the entire bundle together. The Teflon tape serves as a good cushion between the clamps and fibers thereby eliminating gaps. The bundle is positioned vertically and

sliding hexagonal clamps are assembled along the length of the bundle. The hexagonal case is isolated from the bundle leaving it purely supported by the 5-tiered sliding clamps and choke ring. This type of assembly design greatly helped in the maintainability of the hexagonal bundle through the course of the preform preparation and drawing.

In this draw a hexagonal bundle of fibers from the first draw would form a fiber that has the profile of the entire bundle.

Typical Experiment Log

12:15 pm – Preform loaded. Staring preform position is 675 mm. Preform bottom just in furnace (~5 mm below the top of the furnace). Furnace set to 950ºC. Iris partially closed.

12:42 pm – Furnace temperature = 950ºC. Feed started (Feed Speed = 5.835 mm/min).

1:08 pm – Preform drops. Preform position = 529mm. Draw started (Draw Speed = 8 m/min). Cutter turned on (Cut Length = 700 mm). Iris closed.

1:29 pm – Drawing equilibrated

Tension = .78 kg, Target face to face distance of fiber = .686 mm, Yield ~ 1500 pieces of fiber

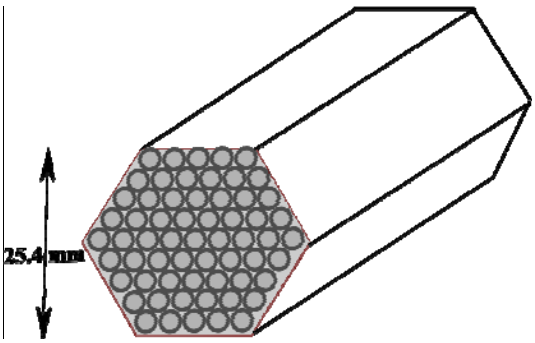

Fig. 1.7– Fiber Bundle Schematic

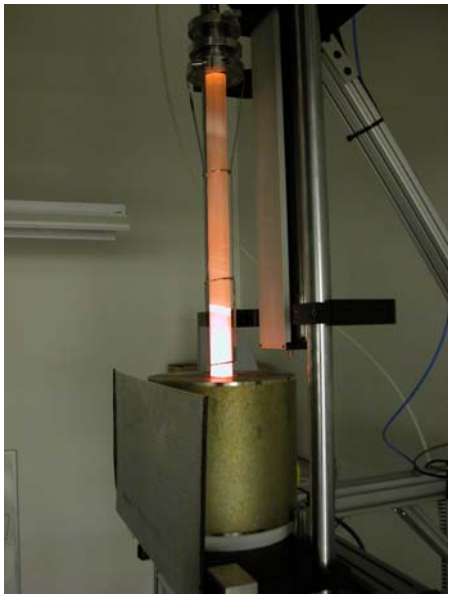

Fig. 1.8– Preform Assembly Feeding to Hot Furnace

The Third Draw

This is similar to the second draw and results in feature sizes of 1.6 μm. The end profiles of the fibers from each of the draws are shown in Fig. 1.9.

Bundling and Preform Preparation

The fibers are now bundled again for the third and final draw. This draw must still maintain minimum distortion of the shape of the double drawn bundle. The target lattice constant for the double drawn fiber would be approximately 1.6 μm. The bundling and preform preparation is exactly similar to described for the second draw.

Typical Experiment Log

11:35 am – Preform loaded. Staring preform position is 550 mm. Furnace set to 950ºC. Iris partially closed.

12:06 pm – Furnace temperature = 950ºC. Feed started (Feed Speed = 5.835 mm/min).

12:30 pm – Preform drops. Draw started (Draw Speed = 8 m/min). Cutter turned on (Cut Length = 100 mm). Iris closed. Furnace Temperature lowered to 850ºC.

12:40 – Furnace Temperature = 850ºC. Preform position = 365 mm.

1:29 pm – Drawing equilibrated, Tension = .78 kg, Target face to face distance of fiber = .686 mm, Yield ~ 1500 pieces of fiber

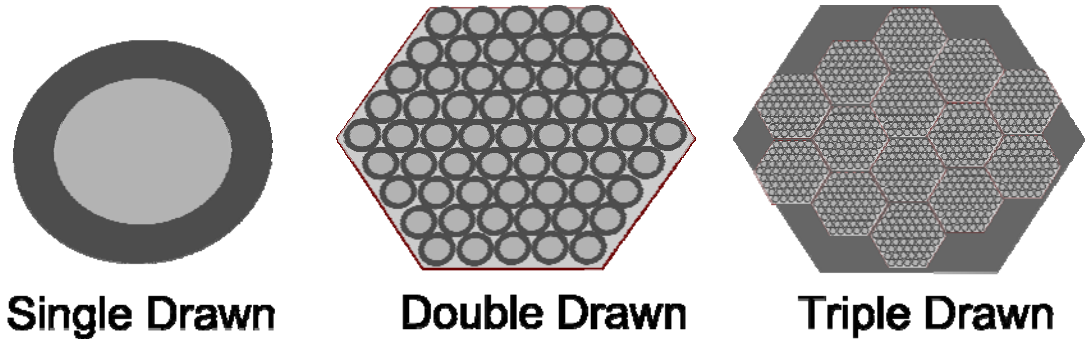

Fig. 1.9 - Fiber End Profiles at Various Draw Stages

Wafer Fabrication

Fusion

The experimental step that follows the drawing is the fusion process. Fusion involves the heating of a fiber bundle consisting of tiny features of glasses with different compositions. In this stage properties like phase separation and interdiffusion that play an important role are discussed.

The Fusion Furnace

A Lindberg Hinged 555000 Series tube furnace is used for the fusion process. The furnace is of vertical type and can process tube lengths from ¾ - 6". It operates on 50/60 Hz single phase 240V AC. The maximum operating temperature is 1200ºC. An alloy heating element, high temperature ceramic fiber insulation and a Platinel II thermocouple form the primary components. Temperature profiling is achieved by a three zone heated chamber system. The three zones are of equal length and power output. A three-zone type of temperature profiling helps achieve greater linear temperature uniformity. Several factors can affect the temperature uniformity like load, operating temperature and vacuum conditions. The intense heat softens the glass and burns off other unwanted constituents. Simple programs specifying the intended heating profile can be keyed into the controller. Profiles typically run through a ramp to high value, dwell, and ramp to low value style.

Fusion Bundle Preparation

A thoroughly cleaned tube made of Schott 8330 glass of 25.4 mm O.D and a 1.5 mm wall is typically used for making the fusion bundle. A smaller bundle is more robust for better heat distribution and hence more uniformity. One end of the tube is closed and the other end is flared. The fibers are uniformly packed in the tube. The final fusion bundle is always in a cylindrical tube. The same hexagonal packing process is employed to ensure that the bundle is well packed and uniform. The vacuum clamps are mounted on the flared side of the tube and fixed to the preform vacuum chuck of the furnace.

Fusion Process

The goal of the fusion process is to heat the bundle up to a point where the tube softens and just begins to collapse. This must eliminate gaps and interstitial spaces resulting in a continuous matrix. The fusion must thereby help maintain a fixed alignment of the fibers in a rigid rod.

Fusing a bundle of considerable size also helps in creating a fiber matrix which is easier to handle and useful for surface based experiments. A high quality fused perform in this case would consist of uniform and periodic hexagonal channels (each channel corresponding to a fiber in the bundle). This hexagon can have the double or the triple drawn fiber profile based on which was used for the fusion. The fusion perform is positioned in the middle zone which is the central point of heat distribution maintained at the highest temperature *(Fig. 1.10)*. The starting diameter of the tube was 25.4 mm, which reduced to 24 mm as a result of the collapse due to fusion. The highest temperature reached in the process must not be too much above the softening point of the glass causing it to stretch and lose its cylindrical shape. The vacuum system in the fusion furnace is an important feature. The vacuum plays a pivotal role in removing the air from the small spaces and keeping the fibers in place. An annealing process that avoids stress development in the heat-treated glasses follows the softening process. Several tries of fusion helped optimize temperature and other operating conditions. A fundamental advantage of keeping the fusion process completely independent of the draw is ease of tuning of parameters.

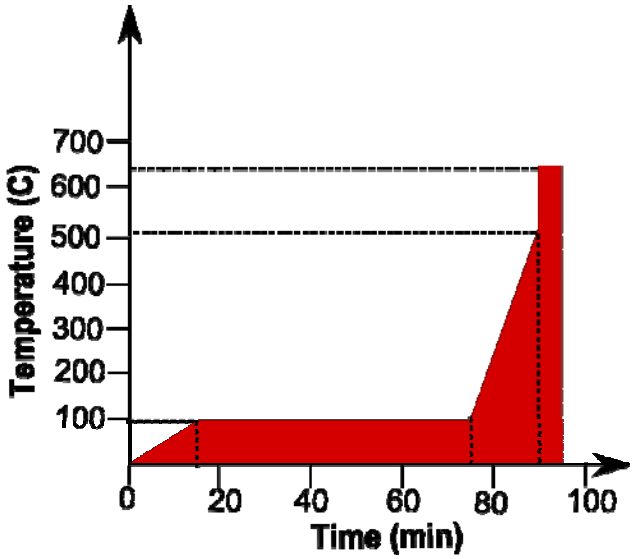

Fig. 1.10 –Temperature Profile - Fusion of the Triple Drawn Fibers

Phase separation and Interdiffusion

We have already discussed the theory of phase separation in borosilicate glasses which makes them separate into two distinct regions called phases. The degree of separation of the borate and silica phases of the glasses used depends on the initial chemical composition and also on heat treatment. This in turn affects the etch rate contrast of the glasses. In the immiscibility region of the Na_2O-B_2O_3-SiO_2 system present in the borosilicate glasses that were drawn there is a great tendency to phase separate. Phase separation implies micro structural changes after heat treatment. It can result from spinoidal decomposition (two interconnected interpenetrating networks) or nucleation (droplets of one phase of a matrix in the other). In the case of spinoidal decomposition, the borate-rich phase can be leached out by dilute acid, leaving a sponge consisting of about 96 % silica. The fundamental separation here involves that of the silica-rich and the alkali borate-rich phase. The degree of interconnection of the two phases depends on the constituent components present in the glass. The increased borate content in the 8487 glass causes increased connectivity of the easily etched phase. The scale phase separation can be increased by suitable heat treatment until the dimensions of the separated regions, as seen on an electron micrograph, are of one or more microns.

Interdiffusion of the glasses, which can occur at high temperatures, can cause reduced channel width and homogenization. This can completely destroy the feature uniformity. Additional phase separation can cause high degrees of heterogeneities in the fused bundle.

Slicing and Polishing

The sections below discuss the process of preparing the fused bundle for the etching process. For enhancing features in the order of a few microns by etching the surface roughness present in wafers has to be much lesser than the feature size to avoid non uniformity in the etching profile. Hence the wafers have to be polished to a very fine degree

Slicing - Once the fusion process is complete the bundle is sliced into wafers and polished. The slicing method must not introduce structural damage and defects to the area under analysis. The Isomet 1000 precision sectioning saw that can handle a wide range of materials including glass was used. The saw, which is a 7" blade, has a large cutting capacity. It is equipped with variable speed up to 975 rpm and position control to handle different substrates of various sizes. Fixtures supporting a sample holder attached to an externally controllable arm hold the fused bundle. Loads are applied on the arm based on a gravity feed design to adjust the counterbalancing weight

of the sample. The relative horizontal positioning of the fused bundle with respect to the can be controlled by the digital micrometer. It has a constant water-cooling system that keeps that sample from getting overheated due to friction. The assembly is completely encased in a transparent hood. An interlock system prevents the motion of the saw once the hood is opened.

The slicing process involves

- Careful mounting of the fused bundle in the sample holder with right orientation - The axis of the fused cylinder must be perpendicular to the plane of the diamond saw. This ensures parallel slices.
- Setting the thickness - The micrometer reading must take into account the blade thickness and the possible reduction in thickness due to polishing. The final wafer after slicing and polishing is 1.5 mm thick.
- Setting the speed of the diamond coated saw followed by the cutting - The sample holder must be held against the direction of the cutting towards the very end of the slicing process to ensure that the saw does not chip off the rest of the slice in an uneven fashion.

Polishing - Polishing creates a smooth, shiny, flat, and defect free surface. The sliced wafers were polished in an ULTRAPOL polisher that can make both flat and angled surfaces. A rotating wheel in the polisher holds polishing films. These diamond lapping films are coated with are 8" in diameter. The dimension of the diamond lapping indicates the minimum structure dimension that it can polish. The polishing films are changed periodically due to wear and tear. A built in tachometer helps control the speed of the wheel. The sample to be polished is wax mounted on a flat metal holder. This is attached to a movable arm in the polisher. The angular, vertical and horizontal alignment of the surface of the sample can be controlled by a set of micrometers. The surface to be polished must be kept as parallel as possible to the surface of the polishing area to ensure flatness and uniformity of the finished surface. The feed is gravity based allowing the sample to push against the rotating diamond lapping under the weight of its metal mount. An LED indicator driven by a touch sensor indicates whether the currently contacting surface has been polished. A water spraying system fed from a reservoir helps keep the sample from overheating due to friction.

A series of films were used to get down to a very fine polished surface. The sample was first hand polished to remove large burrs left from the slicing. The sample was then mounted on the polisher and ran through 30 μm, 15 μm, 6 μm, 3 μm and 1 μm lappings in that order. This

stepwise polishing helped eliminate scratches and unevenness of a range of dimensions down to a micron. The final polishing touch was given using an alumina lapping of .5 μm to make it smoother and shinier. The microstructure of the surface was examined in an optical microscope to check for a uniformly and evenly polished surface.

Structure Fabrication

Hydrofluoric Acid Solutions

This section explains the equilibration of different aqueous solutions containing HF that are used in the etching process. Knowledge on the constituent ions of the solutions is essential to understanding the etching chemistry of these solutions on the multicomponent borosilicate glass.

Glass and HF

HF or HF containing aqueous solutions at room temperature readily dissolves silicate glasses. Hydrofluoric acid is weak due to its incomplete dissociation. It however contains H^+, HF_2^- and F^- ions along with the un-dissociated HF molecules. The mechanism involved in the dissolution reaction of pure HF with borosilicate glasses is the same though the rate of etching may vary with different etchant compositions and glasses. Three primary reactive species are HF and HF_2^- and the catalytic species are the H^+ ions. HF_2^- ions are adsorbed by surface silanol groups, HF molecules by vicinal silanol groups and H^+ by surface bridging oxygen in siloxane units. However the reactivity of Fluoride is considered to be negligible though the concentration of the Fluoride ions play an important role in controlling the etch rate.

The dissolutions of vitreous SiO_2 in HF solution can be described by the following reaction

$$\mathbf{SiO_2 + 6HF \text{ ->> } H_2SiF_6 + 2H_2O}$$

Equilibria of HF solutions

Glass etching process involves the breaking of the covalently connected siloxane bond structure. This results in the release of silicon from the glass. The etching of silicate glasses in aqueous HF solutions has been discussed in detail in [1.16, 1.17]. The wafer consists of a matrix of core Schott 8330 and cladding Schott 8487 glass that underwent the drawing and fusion processes. Schott 8330 is an acid resistant glass with 13% B_2O_3 and the Schott 8487 is an easily etchable glass with an increased 16.5% B_2O_3. In borosilicate glasses, B_2O_3 forms an independent network forming oxide, which is incorporated into the silicate network. The change in etch rate of borosilicate glasses in BHF solutions can be positive negative or zero with the increase of B_2O_3 content in the glass. In contrast, the etch rate in HF etchants increases with B_2O_3 content. This is

because the B-O-Si and the B-O-B bonds are more rapidly attacked by H^+ ions, which are almost absent in the BHF solutions.

Several parameters were studied and the following two were chosen to control the etching mechanism

- Fluoride Ion concentration
- Concentration of Dimer (HF) and Bifluoride Ion (HF_2^-)

Dilute HF (DHF) solutions

The following equilibria can explain dilute HF solutions

$HF \leftrightarrow H^+ + F^-$

$HF + F^- \leftrightarrow HF_2^-$

The ionic strength of dilute HF solutions is very slow and calculations can be done with concentrations instead of activities.

The concentration of the solution can be expressed in terms of its constituent ions by the following equation

$[HF]_{added} = [HF] + [H^+] + [HF_2^-]$ ……..*(1.1)*

Concentrated HF solutions

HF solutions with concentrations above 1M HF have known to exhibit the presence of higher polymeric ions H_nF_{n+1}-. Such solutions exhibit higher acidity and greater etch rates due to enhanced reactivity towards the siloxane bonds. However, higher equilibrium must be considered.

$HF + HF_2\text{-} \leftrightarrow H_2F_3^-$

The concentration of the solution can be expressed in terms of its constituent ions by the following equation

$[HF]_{added} = [HF] + [H^+] + [HF_2^-]$ ……..*(1.2)*

Buffered HF solutions

Addition of NH_4F to HF solution shifts equilibria resulting in an increased HF_2^- concentration well as P_H. Etch rate of silicate glasses depend on HF_2^- ion concentrations and therefore addition of buffered NH_4F affects the etching behavior significantly.

The concentration of the solution can be expressed in terms of its constituent ions by the following equation

$[HF]_{added} + [F^-]_{added} = [HF] + [F^-] + 2[HF_2^-]$ ……..*(1.3)*

Etching

The etching of the constituent glasses is the crucial stage in producing the nanocones. The detailed etching experiment and the parameters set for a desired etching profile are discussed here.

Etching Parameters

Amorphous borosilicate glass is a good candidate for isotropic etching due to its microstructurability and diffusion properties. A functional structure on the composite wafer fabricated with the required morphology is obtained by selecting an appropriate etching process. Chemical solution based wet etching and vapor/reactive ion/ sputter based dry etchings are the two common forms of etching. Chemically strong bases and acids may etch glass. HF reacts with the silicates producing soluble silicon fluoride, which diffuses producing a groove. A multicomponent glass etches un-uniformly resulting in a jagged surface. As already seen in the section on glass properties, glass is easily etched by hydrofluoric acid solution.

The etching process is determined by the following parameters

a) Etching solution - The composition of the fluoride solutions used in the etching of borosilicate glass greatly determines factors in the process chemistry like the etch rate and the surface roughness.

b) Etching temperature – Temperature can speed up the chemical reaction causing increased etch rate.

c) Agitation – Ultrasonic stirring continuously exposes the surface of the sample to fresh volumes of acid resulting in enhanced uniformity and etch rate. However the stirring may not be favorable choice for extremely fine and delicate structure profiles.

The quality of the etched wafer was determined by the following parameters. SEM microscopy gave best results in the study of morphology of the etched sample.

a) Structure Accuracy – An under etched structure displays unfinished stunted cones and an over etched structure displays long thread like cones that may not stand upright on the base. This can be mostly controlled by tuning the time and in some cases the etchant.

b) Cone tip sharpness - Rounded tips functionally deviate from the desired sharp tipped cones indicating inappropriate etching parameters.

c) Cone wall roughness – In spite of fine polishing etching can cause a lot of surface roughness in multicomponent glasses. Smooth walls are the most desired feature and depend on the type of etching solution used.

d) Defect Density – Missing fibers in the bundle, poorly polished wafers, inconsistency in feature sizes can cause defects in the etched sample.

Choice of Solutions

A range of solutions chosen as given in *Table 1.5* for the etching of the multicomponent borosilicate glass wafers can be divided into two regions.

Region 1 – DHF - Simple dilute HF solutions

Region 2 – BHF - Buffered HF solutions that were mixed with NH_4F

The objective was to obtain a series of structures with differing aspect ratios. The formal concentrations of the solutions were tuned by several trial etches to obtain structures of the desired aspect ratio.

Procedure

Safety was of prime importance when dealing with HF solutions. The fluoride ion in HF readily penetrates into the skin causing destruction of deep tissues and bones and makes HF an extremely dangerous acid to work with. A high degree of familiarity with the hazards specific to HF is required. The following safety measures which are strictly recommended for the use of HF was implemented

- Experiments were done in a ventilated fume hood.
- Area of experiments were equipped with a safety shower and eye wash
- Use of Personal Protective equipments like goggles, face shields, double layered
- Nitrile + neoprene gloves, apron and completely covered clothing

Several sliced and polished samples were kept ready for a series of etching experiments. Each time the sample was placed in a HF resistant PTFE container its polished side facing up. The smallest one was chosen to reduce waste. The container was clamped such that it is partially immersed in an ultrasonic bath. The measured volume of the etching solution was dripped on to the sample using a pipette. All containers and devices that handled HF were HF resistant and were mostly made of Teflon. The timer was started at the same instant to keep track of the etching time. After the expiration of the set time the remaining HF in the sample was carefully removed in the hood. The sample was rinsed ultrasonically with water and isopropanol to get rid

of any etch reactants that may still be on the surface and finally was dried using a fresh jet of air. An optical microscope view of the sample gave a good idea of the degree of completion of the etch process for the desired aspect ratio.

Etch Rate Calculations

In this section the differential etching process is evaluated by calculating the etch rates of the individual core and cladding glass. Individual slices of Schott 8330 and Schott-8487 are etched together in various etching solutions and the etch rates are calculated from weight loss in the slices and the slice dimensions.

Etch Rates

The samples etched contained a matrix of 8330 cores surrounded by 8487 claddings. It is the differences in etching rates of these two types of glasses that result in the nanocone structure. The faster etching cladding glass must etch back faster relative to the slower etching core glass resulting in a tapered array of cones. Etch rate contrast is the fundamental concept of a differential etching process. So learning the etch rates of the independent glasses was useful estimate in determining the etch rate contrast of the two glasses.

Table 1.5 – Etching Test Series

Slice Number	Etchant	Etch Time (min)
275	1.5ml BHF + 3.5ml DHF	30
255	1 ml BHF + 4 ml DHF	30
256	.6 ml BHF + 4.4 ml DHF	15
257	.4 ml BHF + 4.6 ml DHF	15
258	.2 ml BHF + 4.8 ml DHF	15
259	.1 ml BHF + 4.9 ml DHF	10
278	5 ml DHF	10
261	4.7 ml DHF + .280 ml Water	15
271	4.85 ml DHF + .160 ml Water	30
290	4.9 ml DHF + .100 ml Water	60

It was useful to build a relationship between the etch rate ratios of the single glass wafers and the calculated aspect ratios of composite glass wafers samples.

The most common technique to calculate the etch rate is by measuring weight loss of the etched sample. Decrease in the wafer thickness of the unprocessed slices can be calculated by the measured mass loss for a known surface area. The slices were made from the original 8330-rod and 8487-tube that was used as the starting preform in the first drawing process. The 8330 slices were flat circular wafers and the 8487 slices were flat circular rings. This was to ensure faithful replication of the glass profile in the composite fabricated wafer. Flatness was obtained by a similar polishing procedure as described in the previous section. A series of 8330 and 8487 glass slices were weighed in an ultramicrobalance and the required parameters were measured. These slices were processed together through an exactly similar etching procedure as the previous processed wafers *(Fig 1.11)*.

The main conditions that were replicated are etched time, ultrasonic agitation and etching solution. The weight was measured again after the etching and the loss in weight was noted.

Etch rate (E.R) which is the rate at which the core and the cladding glass are etched by the etchant is given by the formula below

$E.R = \Delta d/t = \Delta m/\rho * SA * \Delta t$

Weight before Etching = m_initial

Weight after Etching = m_final

ρ = Density

Δt = Etch time

Δd = Thickness Change

Δm = Mass Change = m_final- m_initial

SA = Surface Area

Core Slice

Radius = r_{core} = 10mm

Thickness = t_{core}

Total Surface Area = $SA_{core} = 2(\pi * r_{core} * r_{core}) + 2*3.14* r_{core} * t_{core}$

Density = ρ_{core}= 2.23 g/cm^3

Core Etch Rate = $ER_{core} = \Delta d/t = \Delta m/\rho\_co*SA_{core}*\Delta t$

Cladding Slice

Outer Radius = $r_{cladding\_outer}$ = 23.9 mm

Inner Radius = $r_{cladding\_inner}$ = 22.7 mm

Thickness = $t_{cladding}$

Total Surface Area = $SA_{cladding} = 2(\pi * r_{cladding\_outer} * r_{cladding\_outer}) - 2(\pi * r_{cladding\_inner} * r_{cladding\_inner}) + 2 * \pi * r_{cladding\_outer} * t_{cladding} + 2 * \pi * r_{cladding\_inner} * t_{cladding}$

Density = $\rho_{cladding}$ = 2.21 g/cm^3

Cladding Etch Rate = $ER_{cladding} = \Delta d/t = \Delta m/\rho\_cl*SA_{cladding}*\Delta t$

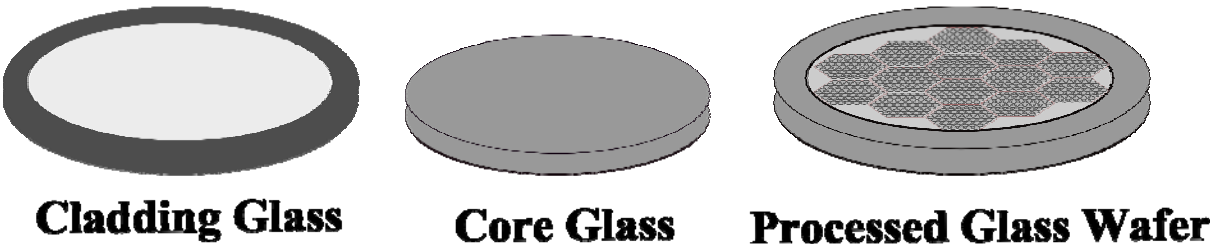

Fig. 1.11 – Wafers for Etch Rate Calculations

The dimensional parameters of each of the wafers used for the etch rate calculations is listed in *Table 1.6*. For a glass of known density and dimensions the calculations were done to calculate the etch rate and tabulated as shown in *Table 1.7.*

Table 1.6 – Wafer Parameters for Etch Tests

Test Number	Etch process replicated	Slice	Thickness (inches)	Surface Area(mm^2)
280	278	8330 8487	.0714 .08745	7.4189 4.128136
281	275	8330 8487	.0669 .0909	7.347 4.25636
282	255	8330 8487	.0721 .0937	7.43 4.3604
283	256	8330 8487	.0722 .08485	7.4316 4.0315
284	257	8330 8487	.0798 .0907	7.5529 4.2489
285	258	8330 8487	.0707 .08775	7.4077 4.139286
286	290	8330 8487	.0744 .09485	7.4667 4.40316
287	259	8330 8487	.0730 .09255	7.444 4.31768
288	261	8330 8487	.075 .0880	7.47634 4.128136
289	271	8330 8487	.0704 .09685	7.40296 4.47749

Table 1.7 – Etch Rates of Individual Core and Cladding Glass

Test Number	Slice	Weight Loss mg	Etch Time (min)	Etch Rate (µm/min)
280	8330 8487	2.2225 4.7346	10	.13433 .50973
281	8330 8487	3.0892 2.2677	30	.06285 .07893
282	8330 8487	4.5309 3.6268	30	.091152 .12322
283	8330 8487	3.3375 2.5534	15	.13425 .18766
284	8330 8487	2.8067 2.5795	15	.11109 .17988
285	8330 8487	2.8596 3.0706	15	.1154 .21979
286	8330 8487	2.6672 8.7632	15	.026697 .14742
287	8330 8487	2.2043 2.6093	10	.13278 .26859
288	8330 8487	2.4109 4.8621	15	.09640 .3472
289	8330 8487	2.0473 6.0127	30	.041338 .20373

Etching Characterization

Work has been reported in studying the etching mechanism by calculating the activities of the constituent ions used in the solutions based on the equilibria [1.18, 1.19]. This section uses a similar approach in calculating the values of the ion activities for varying solution molalities.

Activity of solution species

A good characterization of the fluoride solutions helps in understanding and controlling the etching mechanism. This involves the calculation of the solution species activities of different solutions of a range of concentrations. The activity of a substance is closely related to its concentration and is given by

$\mathbf{a_i = \exp[(\mu_i - \mu_i^o) / RT]}$

a_i = Activity of the species i

μ_i = Chemical Potential of species i in that phase

μ_i^o = Chemical potential of species i in its standard state

R = Standard gas constant.

T = Absolute temperature

A direct use of measured concentration of a substance may not give accurate indication of its chemical effectiveness and activity is used instead. For each solution type the activity is calculated by multiplying the calculated concentration by a known activity coefficient. The activity coefficient is a measure of how much the solution differs from the ideal solution i.e. one in which the effectiveness of each molecule is equal to its theoretical effectiveness. Since a range of concentrations of HF and NH_4F are used in both the pure DHF etchants as well as the BHF etchants the activities are calculated from the following equilibria.

$HF \leftrightarrow H^+ + F^-$	$Ka = a_{H+} * a_{F-} / a_{HF}$	$= \mathbf{b_{H+} * b_{F-} * \gamma^2_{\pm} / b_{HF} * \gamma_{HF}}$	*…….(1.4)*
$H^+ + F^- \leftrightarrow HF_2^-$	$K1 = a_{HF2-} / a_{HF} * a_{F-}$	$= \mathbf{b_{HF2-} / b_{HF} * b_{F-}}$	*…….(1.5)*
$HF + HF2^- \leftrightarrow H_2F_3$-	$K2 = a_{H2F3-} / a_{HF} * a_{HF2-}$	$= \mathbf{b_{H2F3-} / b_{HF} * b_{HF2}}$	*…….(1.6)*

$\mathbf{a_x}$ = Activity of species x

$\mathbf{b_x}$ = Molality of x

$\boldsymbol{\gamma_x}$ = Activity coefficient of x

$Ka = 6.84 * 10^{-4}$

K1 = 5

K2 = .58

Molalities of Basic Concentrations

The molality of a species in solution is the number of moles of that solute per kilogram of solvent. The molalities of the etching solutions are given in *Table 1.8*.

Molality = (Weight of Solute / Molecular Weight) / Weight of Solvent

HF in Concentrated HF

Weight percent = 49.1

Molecular weight = 20.01 * 10^{-3} g/mol

Molality = 48.2077 m

HF in Dilute HF (10:1 DHF)

Weight percent = 4.4635

Molecular weight = 20.01 * 10^{-3} g/mol

Molality = 2.33485 m

NH_4F in Buffered HF (10:1 BHF)

Weight percent = 36.6

Molecular weight = 37.04 * 10^{-3} g/mol

Molality = 16.80477 m

HF in Buffered HF (10:1 BHF)

Weight percent = 4.6

Molecular weight = 20.01 * 10^{-3} g/mol

Molality = 3.9096 m

Solvent Mass in Basic Concentrations

Mass of Water Solvent in Solution = Wt% of Water* Density

Concentrated HF

Weight percent = 50.9

Density = 1165 g/m^3

Solvent Mass = 592.985 g

Dilute HF (10:1 DHF)

Weight percent = 95.5363

Density = 1165 g/m^3

Solvent Mass = 1112.9978 g

Buffered HF (10:1 BHF)

Weight percent = 58.8

Density = 1100 g/m^3

Solvent Mass = 646.8 g

Species Concentrations

Since the etching solutions are a mixture of at most two different solutions the molalities are calculated by the formula below

For a solution AB containing species A and B

$$\textbf{Molality}_A = (C\_A_A * M\_Solvent_A + C\_A_B * M\_Solvent_B) / M\_Solvent_{AB}$$

$$\textbf{Molality}_B = (C\_B_A * M\_Solvent_A + C\_B_B * M\_Solvent_B) / M\_Solvent_{AB}$$

Table 1.8 – Molalities of Etching Solutions

Slice Number	NH4F Concentration (m)	HF Concentration (m)
275	3.35080	2.64884
255	2.13174	2.5346
256	1.2339	2.4504
257	.808352	2.410599
258	.3972888	2.37207
259	.196966	2.3533
278	-	2.33848
261	-	1.6449
271	-	.92496
290	-	.57642

Calculation of constituent ion concentration

Using *Eqns. 1.2 – 1.6* we get five linear equations with five unknowns

$Ka = a_{H+} * a_{F-} / a_{HF}$ .....*(1.7)*

$K1 = a_{HF2-} / a_{HF} * a_{F-}$ .....*(1.8)*

$K2 = a_{H2F3-} / a_{HF} * a_{HF2}$ .....*(1.9)*

$[[HF]_{added} = [HF] + [H^+] + [HF_2^-]$ .....*(1.10)*

$[HF]_{added} + [F^-]_{added} = [HF] + [F^-] + 2[HF_2^-]$ .....*(1.11)*

The required activities are then replaced with the ratio of the concentration to the activity coefficient. An activity coefficient is taken from the graph for a specific formal concentration of 2m pure HF. It is assumed that the activity coefficients remain unchanged with the addition of more NH_4F. The above set of equations can be written in terms of unknown variables. The activities of the constituent ions are given in *Table 1.9*.

Table 1.9 – Activities of Etching Species

Slice Number	Calculated H+ activity (mol/kg)	Calculated HF activity (mol/kg)	Calculated H2F3- activity (mol/kg)
275	.000118263	.211833	1.41147
255	.000563001	.388757	.998577
256	.0035422	.726322	.554027
257	.0107784	.991504	.339287
258	.0257632	1.20055	.208111
259	.0702727	1.39822	.10349
278	.1384777	1.652097	.055731407
261	.09512555	1.194624	.0194971
271	.05458255	.70839377	.00446944
290	.035087	.457552	.001650705

$.000684 = a*b/c$

$5 = b*d/c$

$.58 = e/c*d$

$C1 = a+c+d+2e$

$C1+C2 = b+c+2d+3e$

$\gamma_{\pm} = .79$

$\gamma_{HF} = .75$

a = Activity of H^+ ions = Concentration of H^+ ions / Activity coefficient $= [H^+]/.79$

b = Activity of F^- ions = Concentration of F^- ions / Activity coefficient $= [F^-]/.79$

c = Activity of HF ions = Concentration of HF ions / Activity coefficient $= [HF]/.75$

d =Activity of HF_2^- ions = Concentration of HF_2^- ions / Activity coefficient $= [HF_2^-]/.79$

e =Activity of $H_2F_3^-$ ions = Concentration of $H_2F_3^-$ ions / Activity coefficient $= [H_2F_3^-]/.79$

Solving the above linear equations the activities were obtained for the concentrations of the major ions.

Etching Profile vs. Time

A series of etch tests were done to understand the feature profiles at various stages of etching process. The successful completion of a nanocone etching process depends on the etching time. But it is necessary to note that while the etch time determines the completion of the etching; it does not affect the final aspect ratio. The etch time is decided based on material, the feature size, and etching conditions like ultrasonic agitation (which typically doubles the etch rate) but is not crucial in terms of determining the aspect ratio. Wafers from the fusion of the double drawn fibers were sliced and etched for a range of periods as shown in *Table 1.10.* The resulting structures were imaged with an SEM.

Table 1.10 – Etch Tests for Double Drawn Wafers

Slice Number	Etching Solution	Time (min)
291	DHF 10:1	15
292	DHF 10:1	75
293	DHF 10:1	135

Analysis and Interpretation of Results

Scanning electron microscope analysis was employed to analyze the feature profiles. The actual feature size and uniformity and the aspect ratio of the etched cones was calculated from the SEM images, which is discussed in this section.

Imaging

The structured wafers were imaged using a scanning electron microscope. An SEM uses an electron gun as its source to produce high resolution (nanometer to micrometer scale) and high magnification images (10X to 100000X) *(Fig. 1.12)*. An electron beam with an energy ranging from 100 to 30,000 eV is highly focused by a series of electromagnetic lenses to a spot size less than 10nm which scans point by point to form an image. It irradiates a micro volume of the sample and loses energy resulting in the emission of secondary electrons, which are collected and amplified. The specimen chamber is maintained at a clean, high vacuum in the order of 10^{-6}Torr.

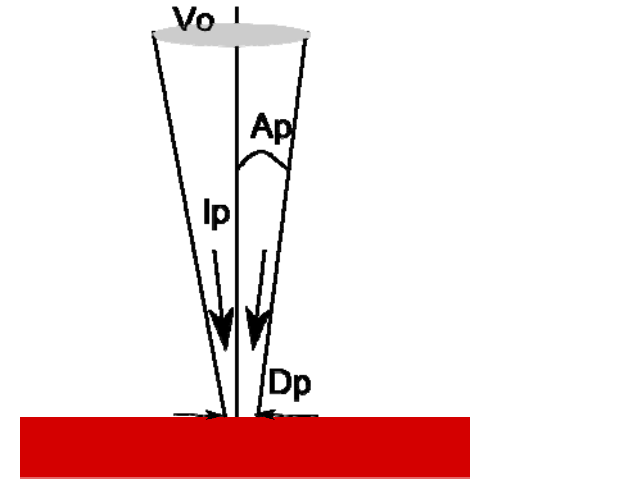

Fig. 1.12 – Electron Probe Parameters of the SEM

The samples have to be prepared in a manner that will make it suitable for viewing in the SEM. The surface is made conductive by coating a thin layer of gold in the order of a few hundred angstroms using the Sputter Coater.

Since the probe being used is an electron gun several control mechanisms can affect the quality of the imaging process. Based on the detail of interest the electron beam parameters are adjusted to get an appropriate scan of the image. The various electron bean parameters are the electron probe diameter, electron probe current, electron probe convergence and the electron bean accelerating voltage can be tuned to get the SEM operating in various imaging modes like the high resolution, high current, depth of focus and low voltage mode. For the etched wafers structural detail was of prime importance and the SEM was operated with a relatively high emission current setting and a good depth of focus. The structures were imaged at various levels of magnification and the feature sizes of the structures were noted.

Aspect Ratio

The aspect ratio of the nanocone features obtained here is defined as the ratio of the height and the width of each nanocone respectively. The aspect ratio control is useful for various applications. We can see that for a given multicomponent glass surface the aspect ratio obtained after etching depends on the etching concentration. The aspect ratios of the various structured surfaces were calculated from the SEM images taken. The samples were viewed with a 45º for best capture of topographic details. The samples were also rotated in order to avoid the features lining up. The tilt and rotation introduced in the cone was considered in the geometric calculation of the aspect ratio *(Fig. 1.13)*. The results are tabulated in *Table 1.11* and are from the measurements made from a 10X magnified image of each of the structures.

Etch rates and Aspect Ratio

The contrast in the etch rates of the individual core and cladding glass is given by the etch rate ratio which is expressed as the rate of the faster etching glass to the slower etching one. This is geometrically related to the slope of the nanocone and hence can be expressed in terms of the aspect ratio. The relationship given below geometrically relates the aspect ratio with the etch rate ratio of the nanocones.

$$\textbf{Etch\_rate\_ratio} = (1 + 4(\textbf{Aspect\_ratio})^2)^{1/2}$$

Aspect ratio = Height of nanocone/Width of nanocone

Etch rate ratio = Etch rate (Faster etching glass) / Etch rate (Slower etching glass)

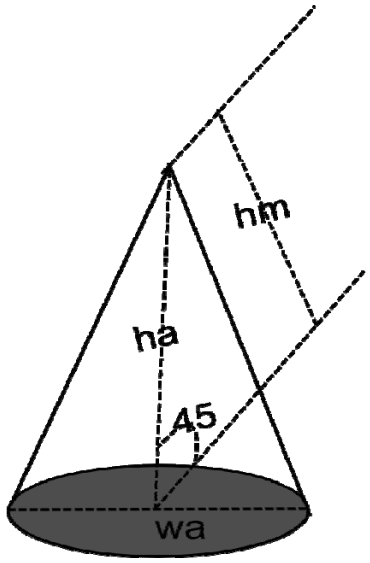

Fig. 1.13 – Aspect Ratio Geometry

Table 1.11 – Aspect Ratio Measurements

Slice No.	Actual Width (cm) – wa	Measured Height (cm) - (hm)	Actual Height (cm) - (ha)	Aspect Ratio (ha/wa)
275	1.824828	.5	.7071	.3874885
255	1.31529	.5	.7071	.5376000
256	1.258967	.7	.9899	.7863113
257	1.004987	.9	1.27278	1.26646
258	1.1	1.3	1.83846	1.671327
259	1	1.6	2.26272	2.26272
278	.6	2.2	3.11124	5.1854
261	.5	2.7	3.81834	7.63668
271	.45	3.6	5.09112	11.3136
290	.4	4.3	6.08106	15.20265

Images

The following SEM images (Fig. 1.14 – Fig. 1.23) correspond to each of the etched slices.

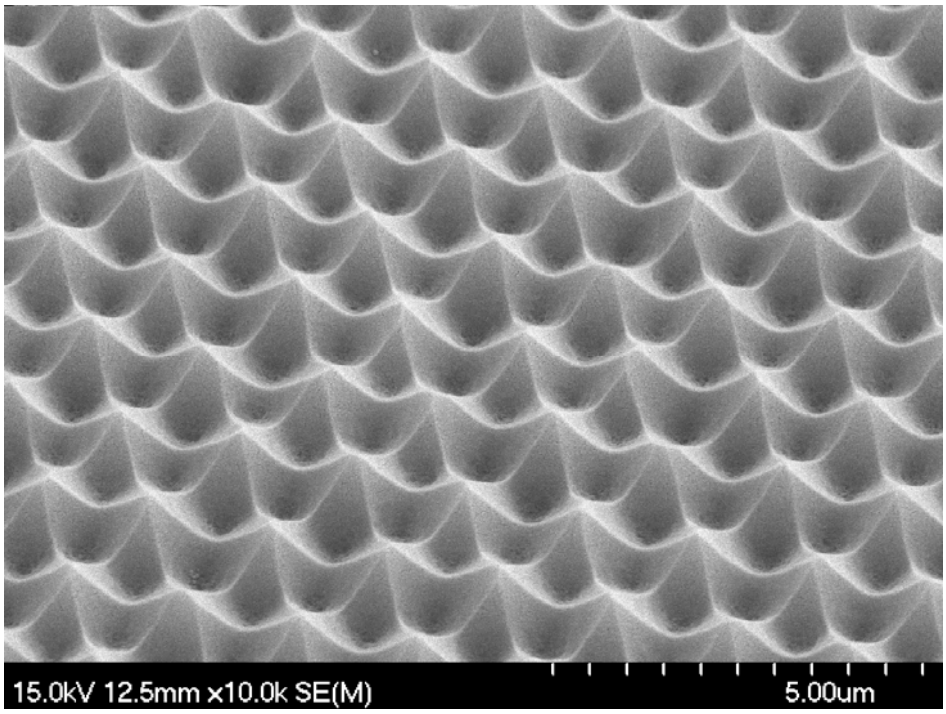

Fig. 1.14 – Slice 275 (Aspect Ratio - .38)

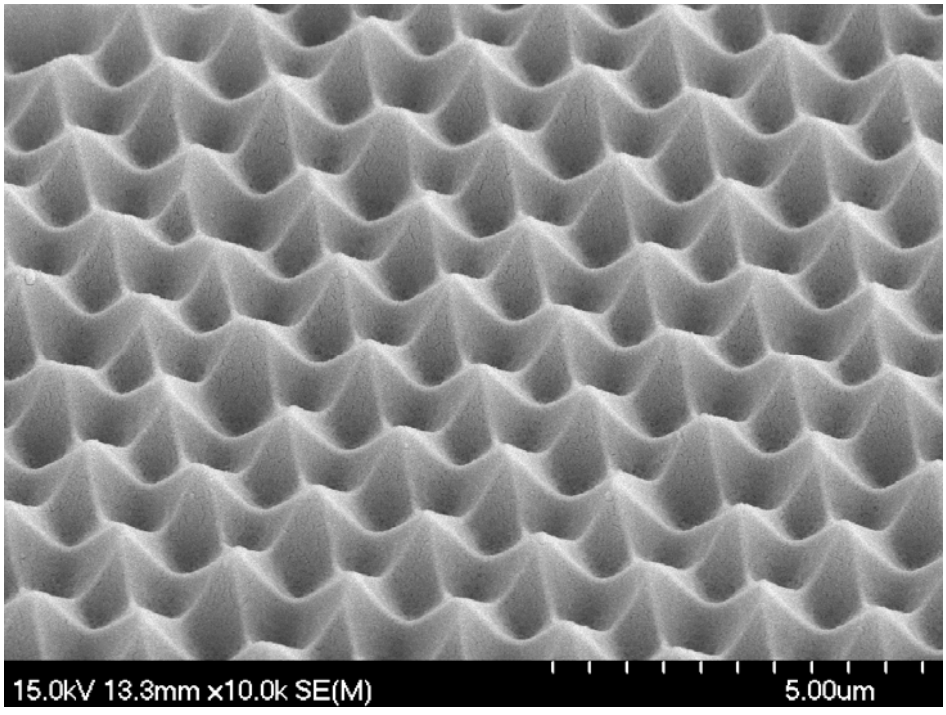

Fig. 1.15 – Slice 255 (Aspect Ratio - .53)

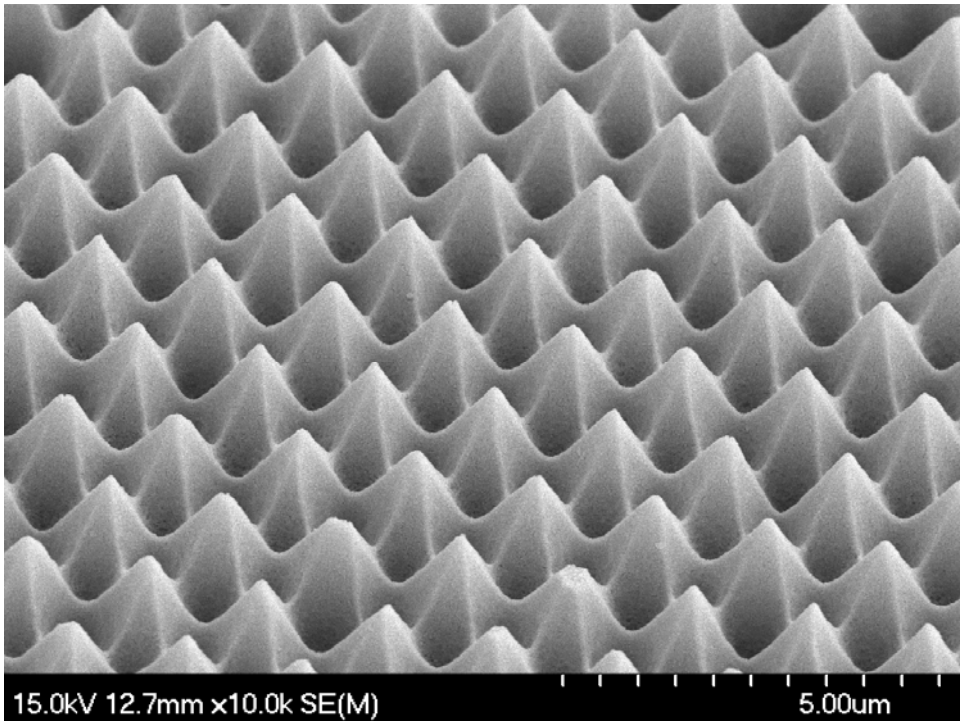

Fig. 1.16 – Slice 256 (Aspect Ratio - .78)

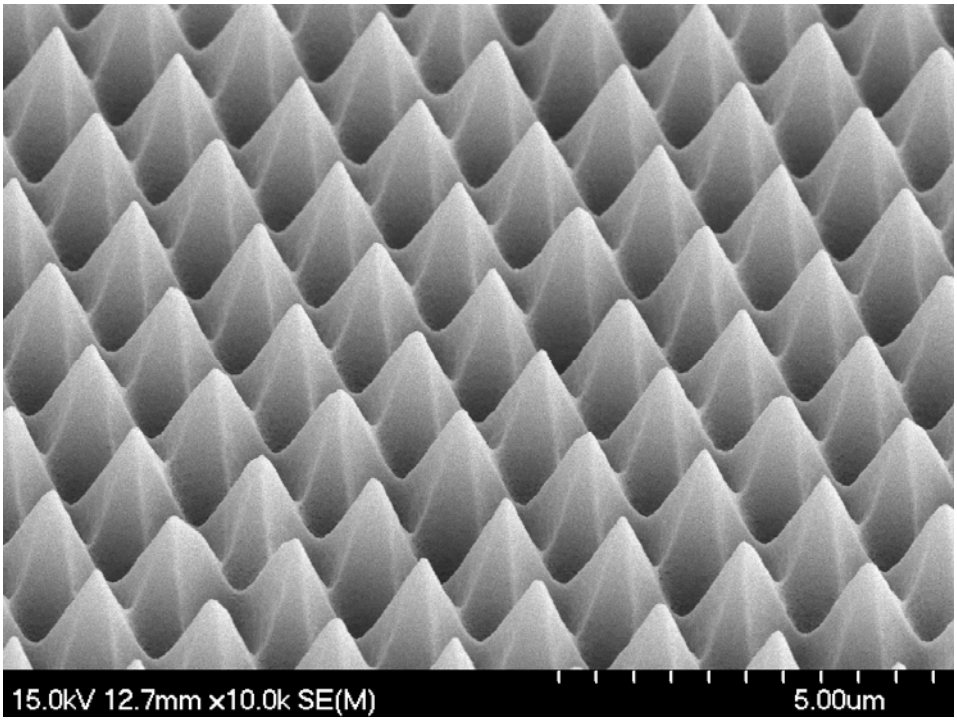

Fig. 1.17 – Slice 257 (Aspect Ratio – 1.2)

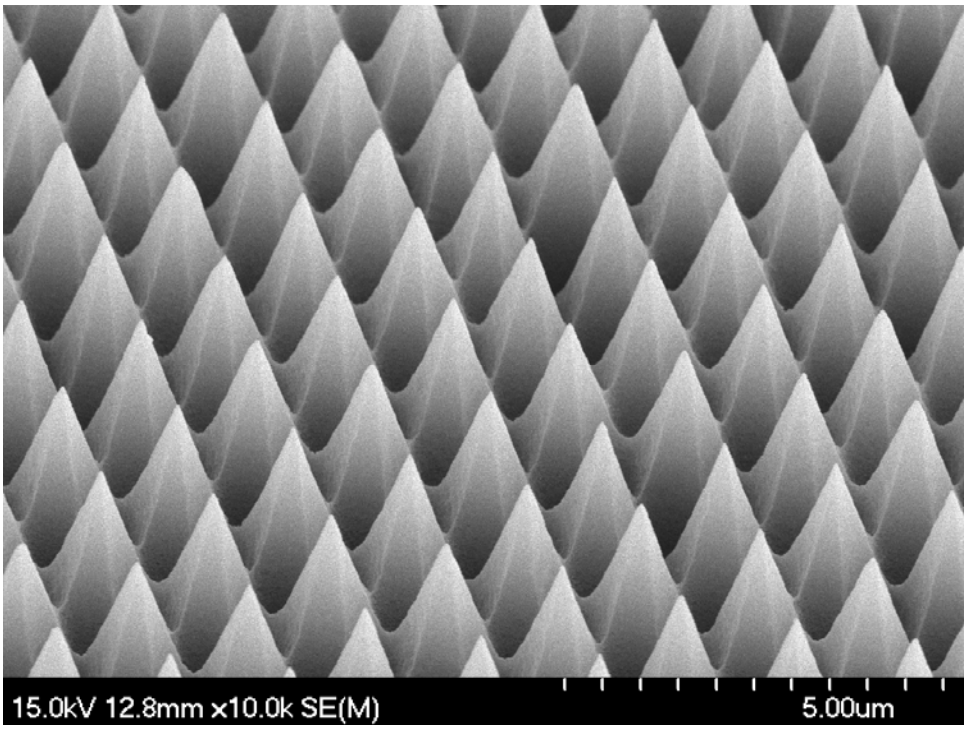

Fig. 1.18 – Slice 258 (Aspect Ratio – 1.6)

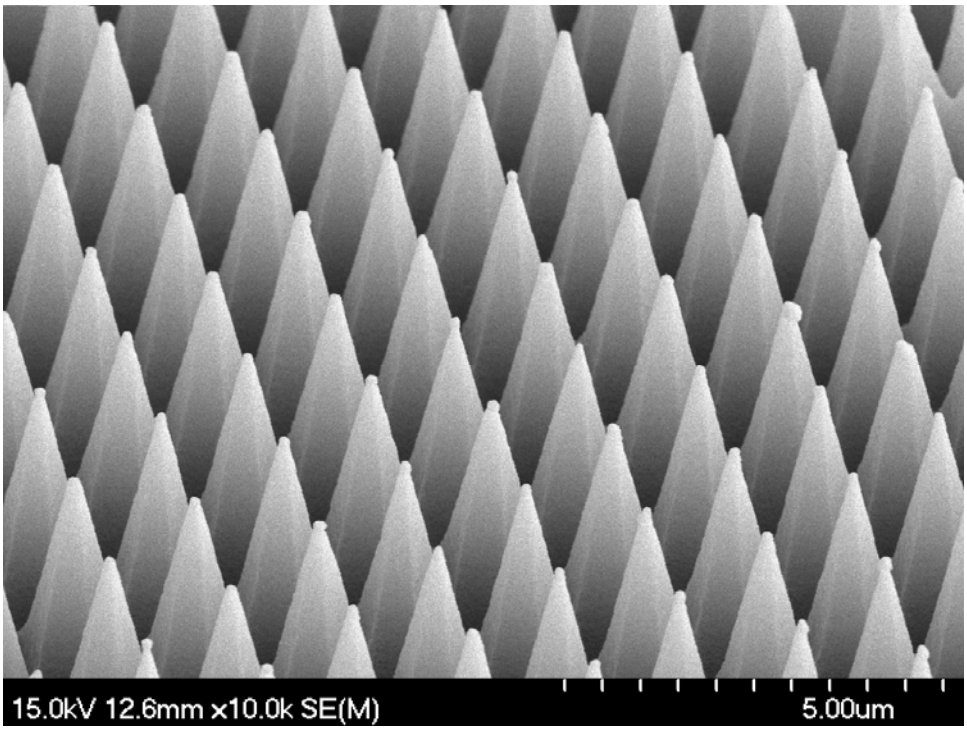

Fig. 1.19 – Slice 259 (Aspect Ratio – 2.2)

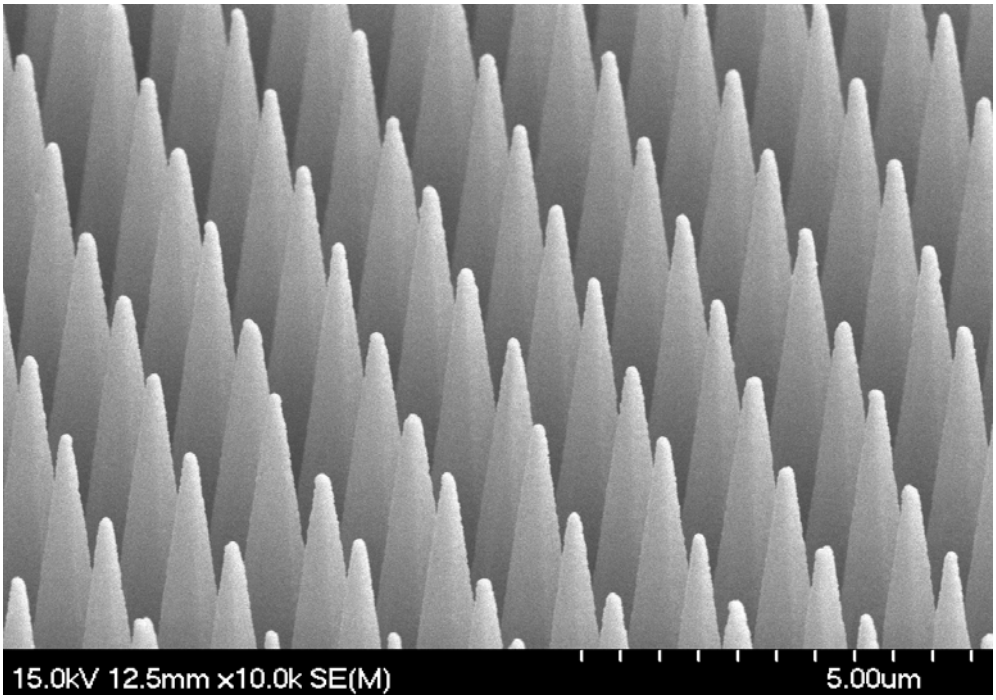

Fig. 1.20 – Slice 278 (Aspect Ratio – 5.1)

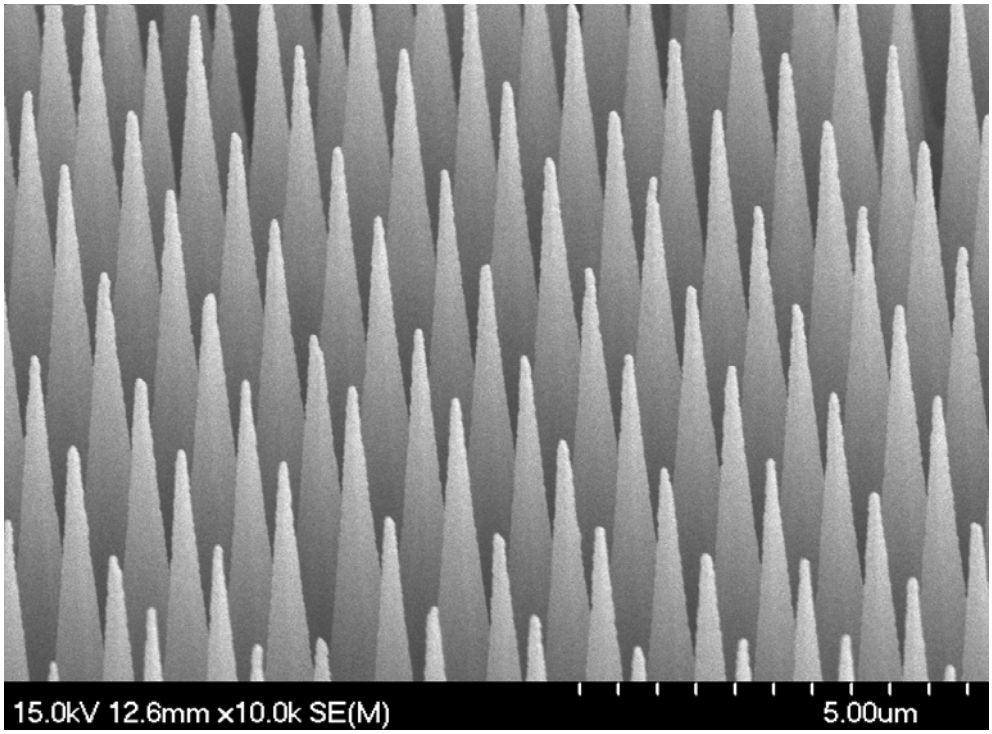

Fig. 1.21 – Slice 261 (Aspect Ratio 7.6)

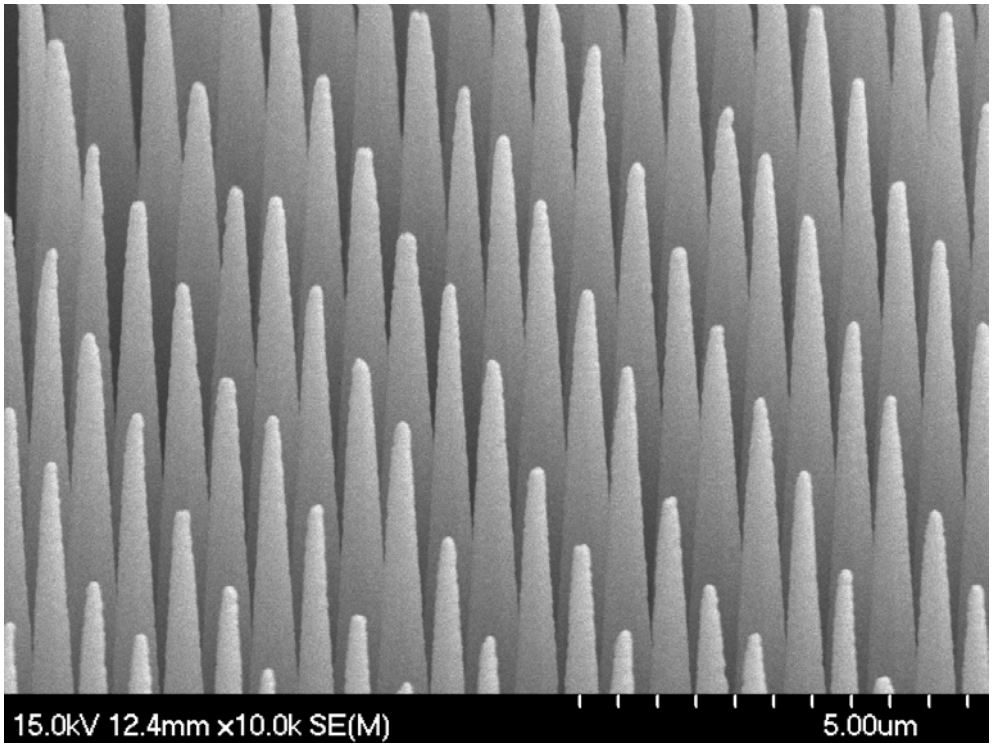

Fig. 1.22 – Slice 271 (Aspect Ratio 11.3)

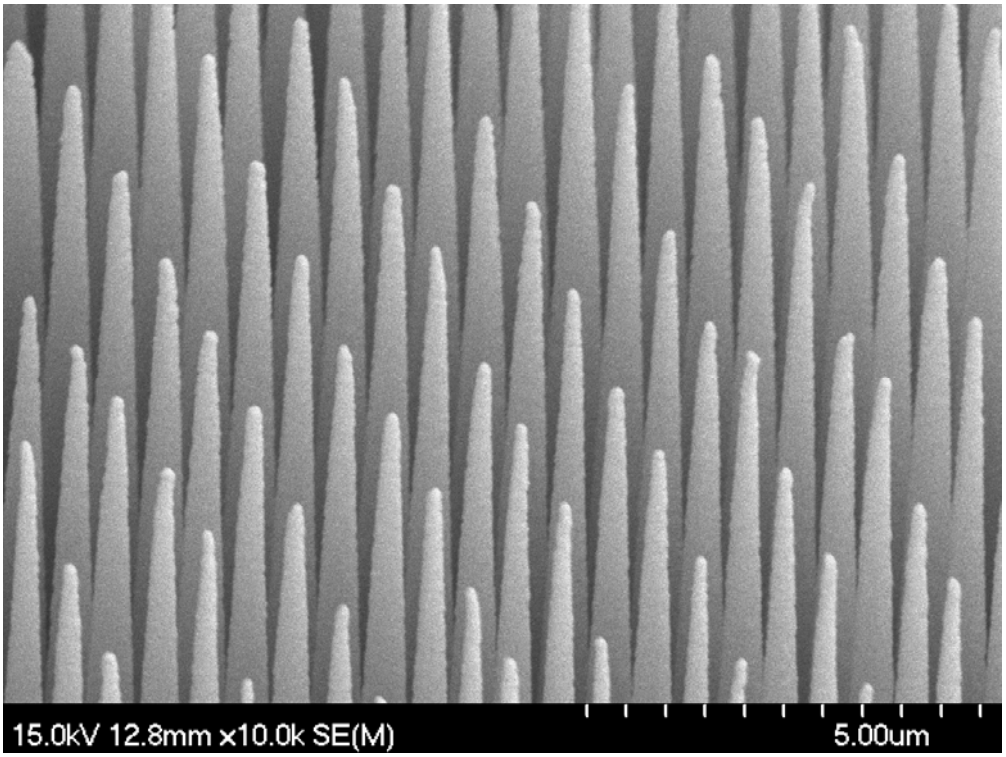

Fig. 1.23 – Slice 290 (Aspect Ratio 15.2)

The following SEM images (Fig. 1.24 – Fig. 1.26) depict the time dependent etching process for a set of double drawn wafers of lattice constant of 40 μm.

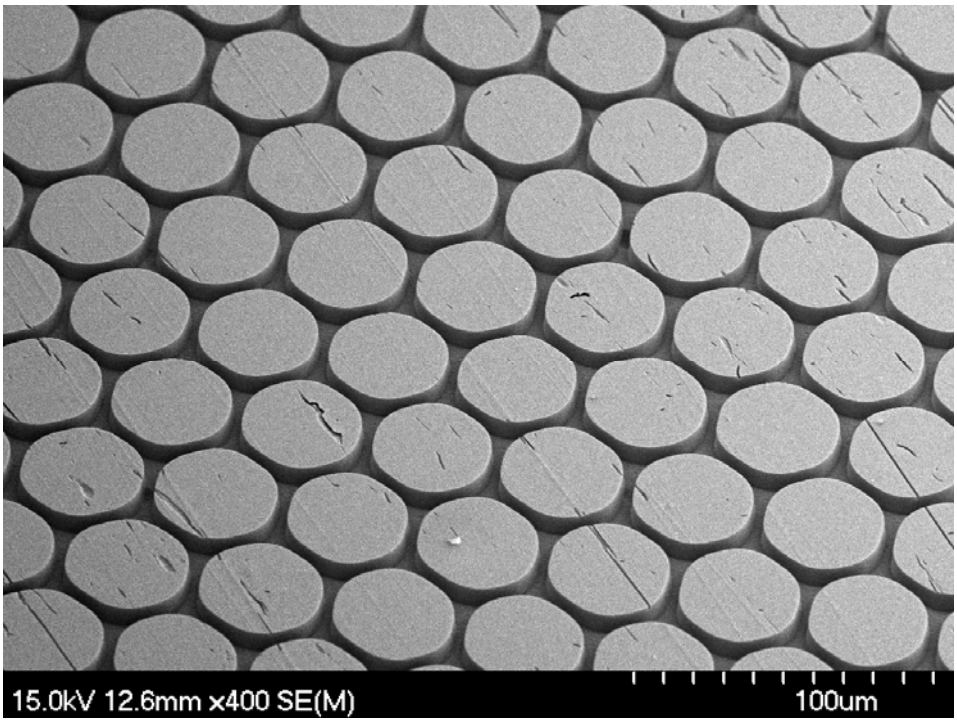

Fig. 1.24 – Sample 291 (Etched for 15 minutes)

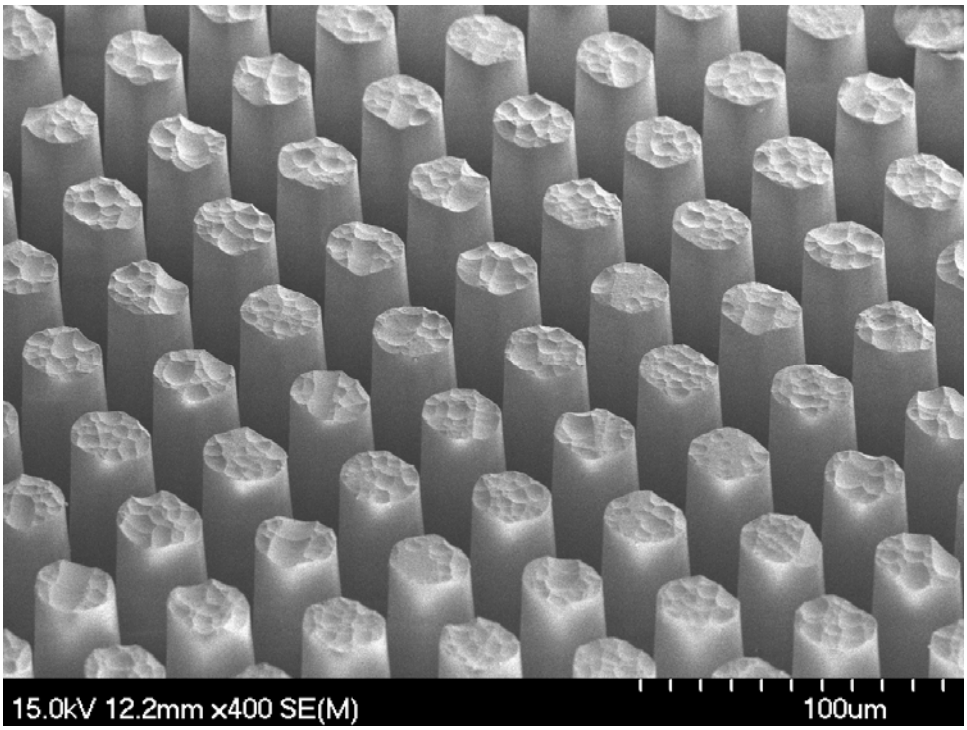

Fig. 1.25 – Sample 292 (Etched for 75 minutes)

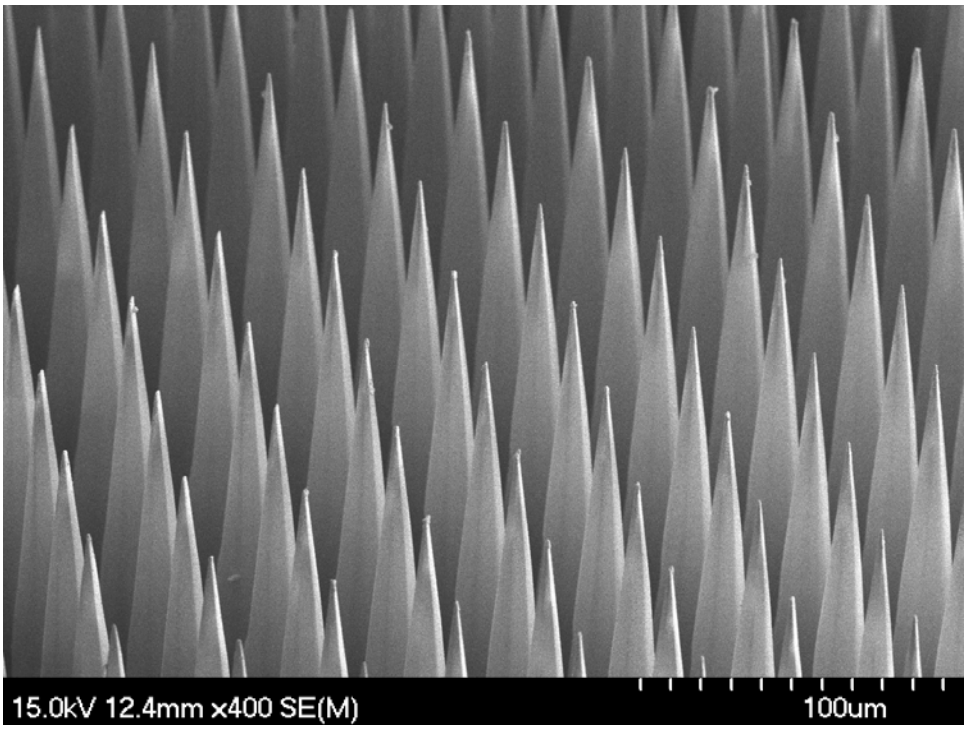

Fig. 1.26 – Sample 293 (Etched for 135 minutes)

Discussion of results

Etch Rate Contrast: The core and cladding glasses have an etch rate contrast. This is primarily estimated by the borate content of the glasses which is the easily etched phase when compared to the acid-resistant silica phase. The etch rate calculations of the individual untreated core and cladding glass for a range of etching concentrations helped in determining the etch rate contrast. The etch rates contrast for the various etch tests indicate that they do depend on the etching concentration. The etch rate contrast is considerably high for pure HF solutions and diminishes for solutions with buffer. We can see that there is significant difference between the theoretically predicted aspect ratios (from the etch rate ratios) the experimentally obtained ones. This can be attributed to the increased phase separation in the processed wafers due to the heat treatment by the fusion process. Thus we observe much larger aspect ratios when compared to the etch rate ratios of the untreated core and cladding slices.

Feature Size Limitation: The smallest attainable feature was a lattice constant of 1.6μm, which was present in the triple drawn fibers. The next smallest feature was 40μm present in the double drawn fibers. Good estimates of the target fiber size and the number of redraws help in the calculation of the final desired lattice constant. Quality of the structure in the final wafer depends

on the bundling and drawing process. A defect free wafer is free of holes and gaps, which tends to cause non-uniformities during the etching process. Going to smaller feature sizes was limited by a few factors. Some were experimental limitations like the cladding wall thickness, which could not survive more number of draws. Another experimental limitation was on the maximum preform size that could be fed into the furnace at each draw. The most significant is the thermodynamic limitation of interdiffusion of extremely small feature sizes during heat treatment.

Role of ionic species in etching process: HF served as the primary etching solution for the glass wafers. Various concentrations of pure HF were used for etching the wafers. The high etch rate contrast of the glasses to pure HF resulted in high aspect ratio features ranging from 5 to 15. However adding a buffer like NH_4F changed the etching behavior of the glass and reduced the aspect ratio of the features with more and more buffer. The nature of etching solutions was understood by characterizing them in terms of the constituent ions. The activities of the ionic species were calculated for various etching solutions. The three primary species that control the etching mechanism are HF, HF_2^- and H^+ ions. The H^+ ions, which are the catalytic species, are mainly responsible for leaching out the borate rich phase of the glass. Their concentrations drop down significantly as the buffer is increased resulting in a diminished etched rate contrast and hence lowered aspect ratio. The concentration of the H^+ ions also reduces with the increased dilution which indicates that they play a lesser role in etching as the dilution is increased. A similar trend is seen for the HF ions. But even with the dilution and the reduced ionic effect, the aspect ratio increases and this is due to the role of water in attacking the faster etching cladding glass. Hence though the etching takes a long time high aspect ratios are obtained due to the strong preferential attacking of the cladding glass by water.

The role of various parameters in the nanocone fabrication process is shown in *Fig. 1.27*.

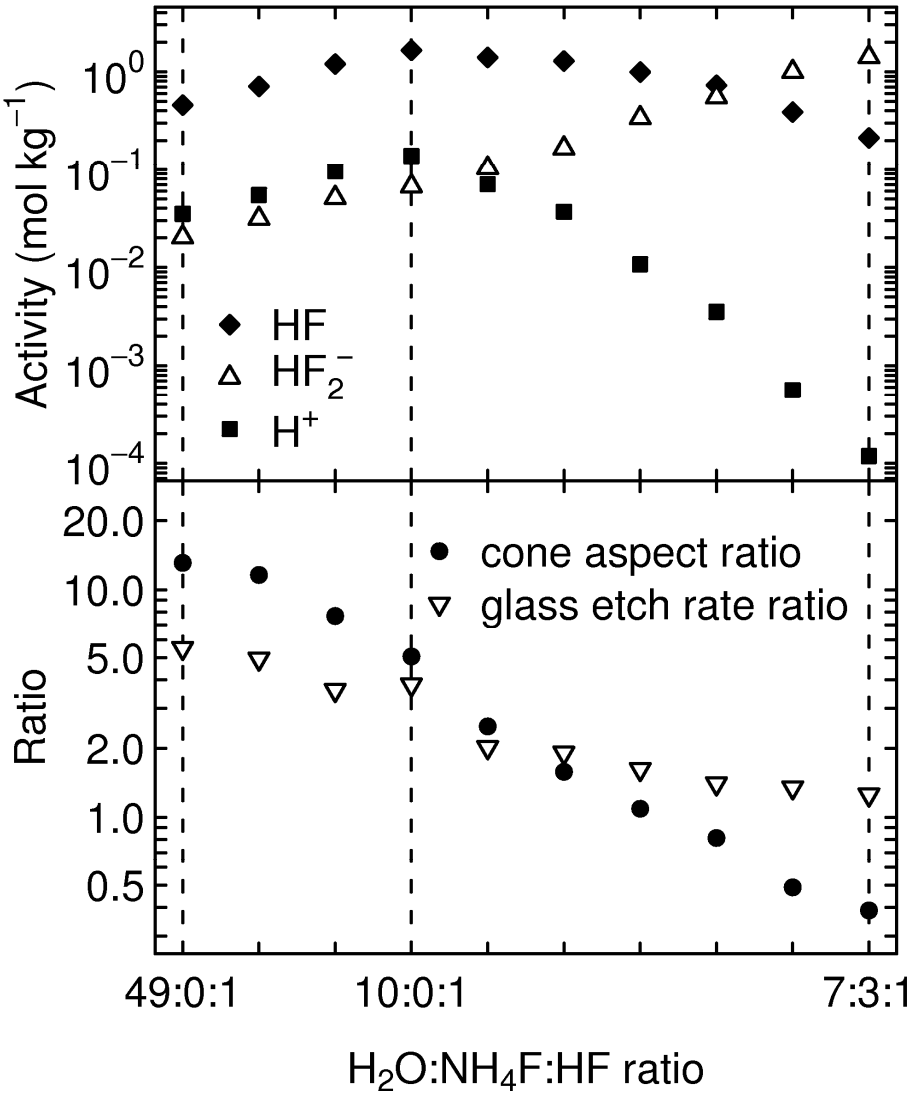

Fig. 1.27 – Relationship between etching and nanocone parameters (Figure is taken from [1.1])

Listed in the next page are figures that summarize the fabrication process. The time dependent differential etching process was studied by etching wafers from the double drawn fusion *(Fig. 1.28)*. The species-concentration dependent etch rate contrast leads to structures of varying aspect ratios for the same type of glass structure *(Fig. 1.29)*. The steps involves in the fabrication process are depicted in *Fig. 1.30*.

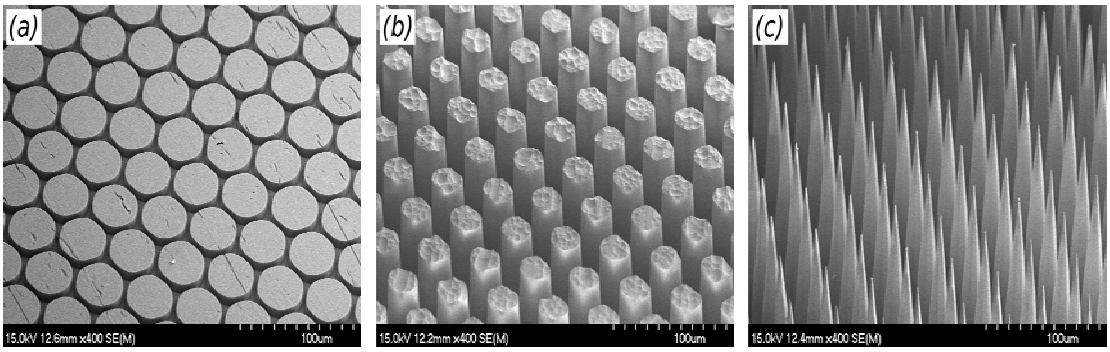

Fig. 1.28 – Differential etching process (at various time stages of etching) Figure is taken from [1.1].

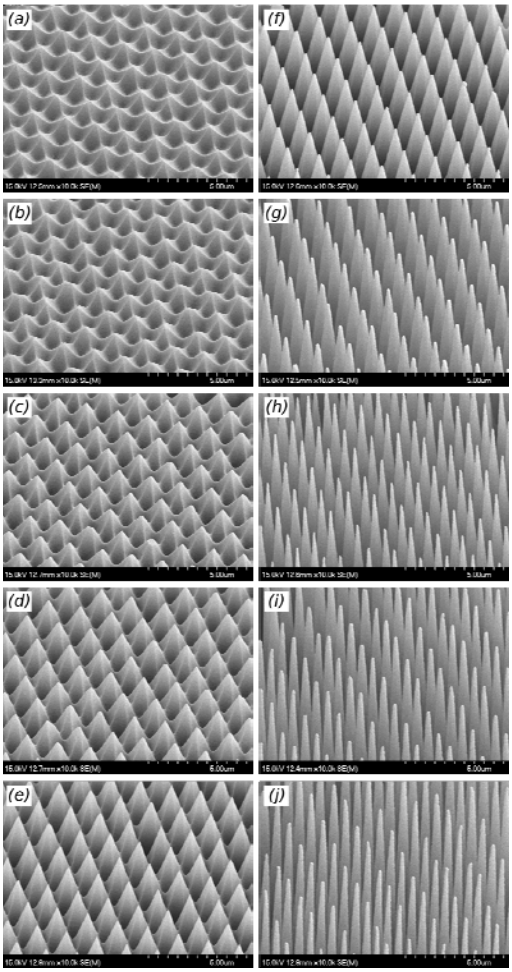

Fig. 1.29 – Nanocone Arrays of Different Aspect Ratios. Figure is taken from [1.1]

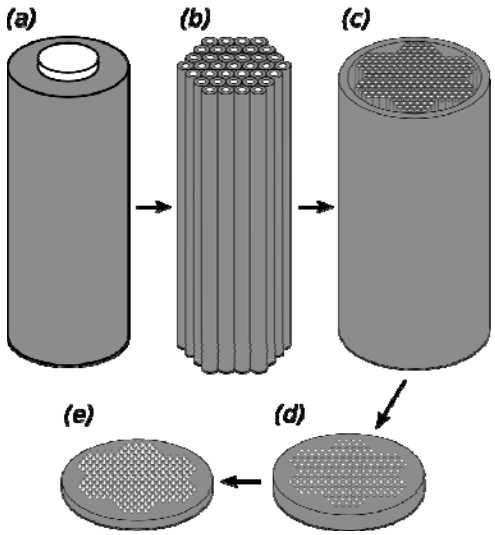

Fig. 1.30 – Steps of the fabrication process Figure is taken from [1.1]

Chapter 3

Static Wetting Properties

Background

Literature Review

A series of vertically aligned glass nanocones were fabricated for superhydrophobic treatment and testing [1.1]. Superhydrophobic surfaces require both surface roughness and low surface energy and several methods to produce such surfaces have been reported. Tunable plasma based techniques have been used to produce surfaces exhibiting contact angles of 102˚ up to 180˚ based on preparation conditions [2.1]. Irradiation of femtosecond laser pulses on silicon has been used to produce structure for superhydrophobic surfaces [1.8]. The water repellant behavior of microstructured surfaces was first studied on a surface of a lotus leaf [2.2]. The earliest and most fundamental theories on wetting regimes of rough surfaces were put forth by Wenzel and Cassie-Baxter [2.3, 2.4]. The degree of fractional wetting seen in a droplet under the Cassie regime has been shown to be dependent on the fractional wetting area of the features. A rough surface, which is hydrophobic, to begin with can be in a fully wetted Wenzel state or in a partially wetted Cassie state. This primarily depends on the aspect ratio of the protrusions causing the roughness. Several works have been reported to explain the tunability of wetting regimes behavior on surfaces with vertically aligned projections. The surfaces of different aspect ratios were coated with a suitable hydrophobic SAM. A good relationship has been established between the pillar height, contact angle and the roughness factor of pillar like surfaces [2.5]. A model to design a robust superhydrophobic surface by comparing the theoretical and experimental contact angles has been reported [2.6]. Tuning of feature parameters and the type of hydrophobic surface has been implemented to produce superhydrophobic surfaces [2.7]. A transition from Cassie to

Wenzel state can also be driven by external force as seen in electrowetting [2.8]. The dynamic contact angles on surfaces coated by fluorinated alkyltrichlorosilane have been studied [2.9]. A characterization of the wetting property of the surfaces was done based on the dynamic contact angles and the sliding angles. This was implemented by an experimental goniometric setup to image advancing and receding droplets on the various surfaces. Several works have been published on experimental methods to measure the contact angle and different methods have also been compared [2.10]. The contact angle hysteresis has been a critical parameter of analysis in these experiments. A useful prediction of hysteresis in terms of tunable feature geometry has been reported [2.11]. A relationship between the sliding angles and the contact angles of superhydrophobic surfaces has also been established [2.12]. The drop images were analyzed by implementing the axisymmetric drop shape analysis method. The fundamental theory behind the method is based on the Young - Laplace equation of capillarity. The method is based on an optimized contact angle calculation by comparing the theoretical and experimental drop fit values [2.13]. A user interfaced tool written in Python was used to run each image through a code sequence that converted the drop coordinates to plot coordinates followed by geometric computation of contact angle. The advancing and receding contact angles were plotted with respect to the aspect ratio of the nanocone wafers. A surface tension based model was used to explain the effect of the restoring pressure on the penetration depth of the droplets, which was in turn ascribed to the apex half angle of the nanocones [2.14]. As the aspect ratio was increased a sharp transition from the Wenzel to the Cassie regime was observed in the varying contact and rolling angles [1.20]. Several papers explaining the nature of the Wenzel to Cassie transition of wetting states have been published [2.15, 2.16].

Nature's contribution – The lotus effect

The main trigger to the extensive study of the wetting properties of surfaces was the discovery of the lotus effect [2.2]. This section discusses the lotus effect, which is the well-known water repellent behavior of lotus leaves.

Botanist, Wilhelm Barthlott from the University of Bonn discovered the Lotus effect in 1975. The discovery was led by examining the micro and nanostructured surface of a lotus leaf under an SEM *(Fig. 2.1)*. The Lotus effect is the theory behind the self-cleaning property of the leaves of the lotus plant that is connected to its water repellant behavior *(Fig. 2.2)*. This effect was explained to be completely dependent on the physio-chemical property of the leaves. The

chemical aspect was attributed to the presence of soluble lipids called waxes on the surface, which are poorly wettable. The physical aspect of roughness in the dimensions of micrometers further enhances the poor wettability. A combination of the effect of a hydrophobic substance and countless miniature protrusions renders the ability of the lotus leaf to let water droplets roll off the surface allowing it to remove the dirt and soil as it moves. This microstructural diversity observed SEM studies on several biological surfaces reveals their tendency to minimize the contact area of anything that comes into contact with the surface. Contaminations that are larger than the cellular structure are carried away easily due to the minimum energy expended in removing the particle when compared to the energy absorbed in carrying away the particle. This energy gain is due to the minimal contact area that the interfacial structure provides to the water droplet. This discovery has proved to be of great technological significance in synthesizing artificial superhydrophobic surfaces.

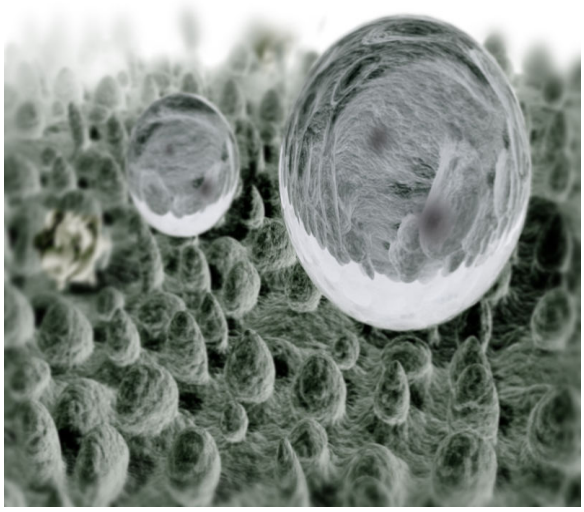

Fig. 2.1 – SEM image of Lotus Leaf

Fig. 2.2– Water Rolling off a Lotus Leaf

Theory of Superhydrophobic Behavior

Contact Angle Theory

The contact angle is the most relevant parameter to describing the wetting property of a surface with respect to a liquid. This section discusses the basic theory of static and dynamic contact angles.

Young's Equation

For a drop of liquid L in coexistence with a gas phase G that is put on a substrate S the key equation describing this situation is the Young's equation which describes the force balance between the interfacial tensions formed at the solid-liquid-vapor contact line.

$\cos \theta_Y = (\gamma_{sv} - \gamma_{sl}) / \gamma_{lv}$

θ_Y = Young's contact angle

γ_{sv} = Surface Tension (energy per unit surface) of the solid-vapor Interface

γ_{sl} = Surface Tension of the solid-liquid interface

γ_{lv} = Surface Tension of the liquid-vapor interface

Static Contact Angle

An important parameter given by the Young's expression is the contact angle θ_Y *(Fig. 2.3)*. This equilibrium contact angle is that of a droplet on an ideal hydrophobic surface, which is smooth, planar, rigid and homogeneous. When the solid surface becomes disordered the advancing and receding contact angles are taken into consideration. A liquid that rests on a solid surface without wetting it exhibits a definite angle of contact between the liquid and the solid phase.

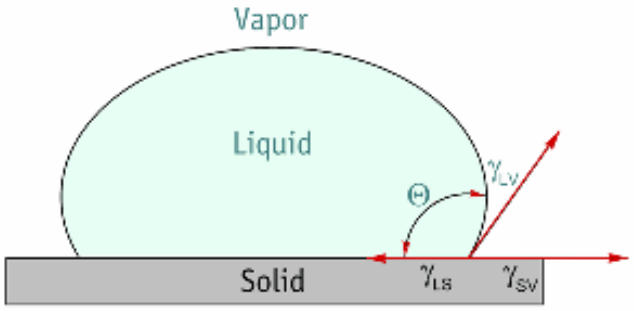

Fig. 2.3 – Young's contact angle

This is a result of the mechanical equilibrium the drop tries to attain under the action of three surface tensions. It is as geometric measure of the angle formed by the liquid at the solid-liquid-vapor boundary. Contact angle is a good parameter that describes the degree of wetting of a liquid and hydrophobic surfaces are those with contact angles greater than 90°. It can be attributed to a balance between the cohesive intermolecular forces of the liquid and the adhesive forces between the solid and liquid.

Dynamic Contact Angles

An interface is not always in a state of definite equilibrium and hence it is more useful to understand the significance of both static as well as dynamic contact angles. The dynamic contact angle describes the happenings at the three-phase boundary during the wetting and dewetting process. Dynamic contact angles are measured when the liquid phase in the system tends to approach the equilibrium state. An advancing contact angle (θ_A) is measured when the droplet's contact angle tends to increase and a receding contact angle (θ_R) is measured when the droplet's contact angle tends to decrease. Advancing and receding angles can be understood from a droplet on a tilted surface (that advances on the downhill side and recedes on the uphill side) and droplets undergoing evaporation or condensation. An alternate type of dynamic angle is called as the rolling angle, which is the tilt angle at which a droplet rolls off a surface. *Fig. 2.4* represents the static and dynamic contact angles of liquids on surfaces.

Hysteresis

A drop that sits on a tilted surface exhibits different contact angles at different ends of the tilt. When the upper and lower angles just approach the receded and advanced contact angle the drop begins to move.

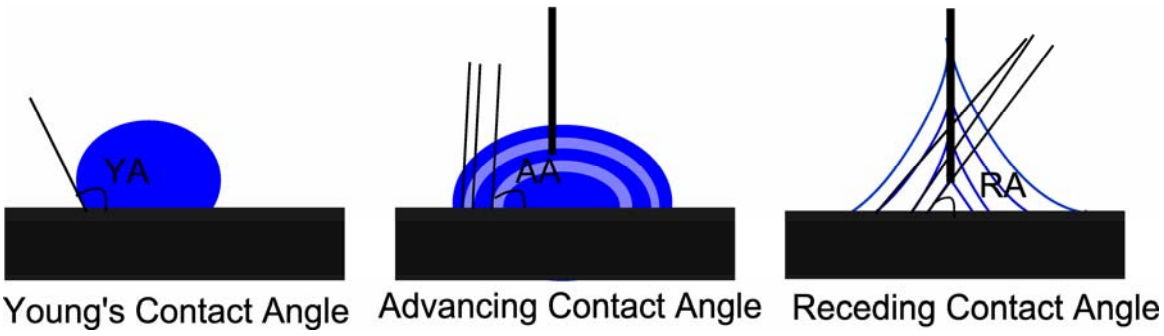

Fig. 2.4 – Static and Dynamic Contact Angles

The range of angles between the advancing and the receding is referred to as the contact hysteresis and plays an important role in understanding the nature of drop motion in a surface [2.11]. Surface non-homogeneities and roughness contribute to the contact angle hysteresis of a droplet on a surface. Increase in roughness increases the hysteresis although the change is the angle is not too large. For much higher degrees of roughness hysteresis almost vanishes due to large increases in the contact angle. Based on the contact angles we can summarize that superhydrophobic surfaces tend to have a high static contact angle, a low contact angle hysteresis and a low rolling angle as well.

Wetting Regimes and Roughness

This section introduces the theoretical classification put forth by Wenzel and Cassie to explain the energy states which attributes to hydrophobic - superhydrophobic surfaces [2.3, 2.4].

Classification

Wenzel, Cassie and Baxter did the earliest work on surface roughness and wetting theory classification. A hydrophobic surface that exhibits more and more roughness on its surface tends to be superhydrophobic. On a rough surface there can be at least two regimes for the contact profile on the surface *(Fig. 2.5)*. Their classification is listed below and the theory supporting it is provided in a forthcoming section.

a - Wenzel Regime (The droplets retains complete contact with the solid at all points)

b - Cassie – Baxter Regime (Air pockets are confined between the solid liquid interface)

Role of Roughness

A non-uniform solid surface is characterized in terms of its roughness. The simplest way to express roughness r is by computing the dispersion of the surface around its mean position z.

$$\mathbf{R = (1/N) \sum_{(x,y)\ \epsilon\ surface} | z(x,y) - z) |}$$

Wenzel regime - A solid surface is best characterized by describing the effective area using a coefficient r, which gives the ratio of the actual to the apparent or projected area. This is referred to as the Wenzel variable. Presence of roughness in a surface leads to a corrected Young's contact angle.

$$\mathbf{\cos\theta_W = r^* \cos\theta_Y}$$

Cassie Baxter Regime - Cassie Baxter regime involves liquids that do not completely fill up the roughness grooves of the surface. Hence the interface can be considered as composite having

both liquid-air as well as liquid-solid interfaces. Thus the apparent contact angle is expressed in terms of the surface area fractions occupied by each of these interfaces.

$\mathbf{\cos\theta_W = \varphi_s * \cos\theta_W + (1-\varphi_s) * \cos 180^o}$

φ_s - fractional area of the solid-liquid interface

$1-\varphi_s$ - fractional area of the liquid-air interface

Once the substrate is hydrophobic the contact angle increases sharply and tends to obey one of the mentioned wetting regimes. The Wenzel regime is homogeneous with higher hysteresis dues to the water sticking to the surface. The Cassie-Baxter is heterogeneous with a lower hysteresis and sliding angle thus making it roll off more easily when a droplet is sitting on air pockets. It has also been realized that the drop has to be sufficiently large when compared to the roughness scale. As seen for ideal surfaces the contact angle is the only independent variable that can be expressed in terms of minimization of the Gibb's energy of a drop. For rough surfaces both the roughness factor as well as the apparent contact angle play a role.

In general the Gibb's energy of an interfacial system can be given as

$G = \sigma_{lf}A_{lf} + \sigma_{sl}A_{sl} + \sigma_{sf}A_{sf}$

σ - Interfacial tension

A - Interfacial area.

Degree of Wetting

A water droplet on a surface that is hydrophobic tends to bead up instead of spreading on the surface. The degree of hydrophobicity of a surface is best characterized by its contact angle.

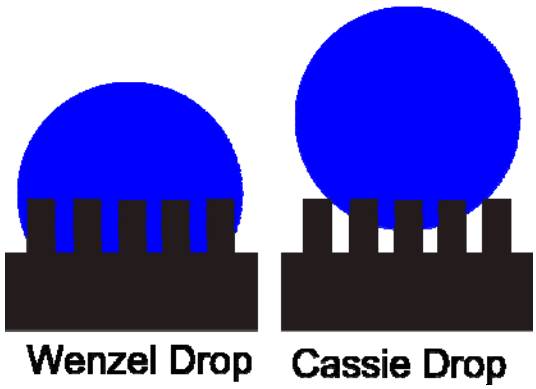

Fig. 2.5 - Cassie –Wenzel Regimes

A contact angle of 0° indicates complete wetting while a contact angle between 0° and 90° shows hydrophilic behavior wherein the water droplet tends to spread on the surface. Contact angles greater than 90° represent hydrophobic surfaces. The maximum attainable contact angle for a smooth surface was measured to be around 120°. But introducing roughness can boost the contact angle of a surface almost by 40°-50° making it fall in the category of superhydrophobic or ultrahydrophobic surfaces. A relationship of contact angle and wetting degree is illustrated in *Fig. 2.6*.

Interfaces

This section discusses the relevance of the physio-chemical properties of an interface that is formed by a surface and the interacting liquid to its wetting behavior.

An Interface

In physical chemistry an interface has been defined as the common boundary between two phases. It can be summarized in terms of the three states of matter as follows

Gas – Liquid, Gas – Solid, Liquid – Liquid, Liquid – Solid, Solid – Solid

The thermodynamic functions of free energy, enthalpy and entropy can be defined for and interface as well. A system involving an interface is not completely stable since equilibrium is dependent on certain factors. Direction and structure are also characteristics involved in the study of interfacial forces.

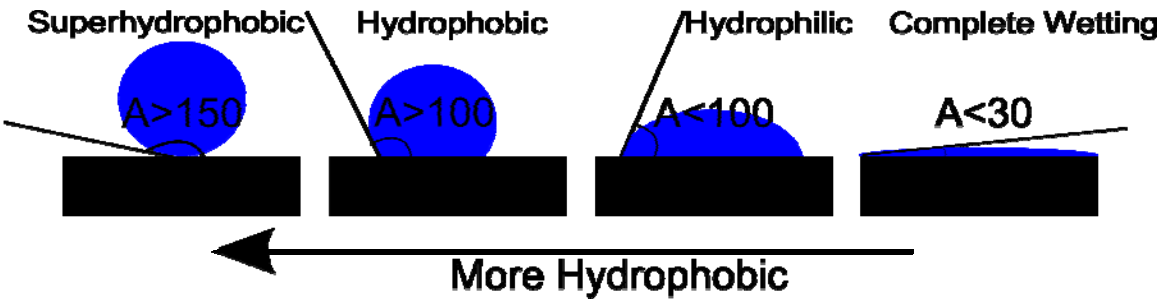

Fig. 2.6 – Degrees of Wetting of Surfaces

Capillarity

The interfacial energy is referred to as the sum of the free energies of all the molecules present in the interface. The stable existence of an interface between any two phases depends on the free energy of the formation of the interface that is positive.

This can be illustrated by liquid that behave as if it were surrounded by an elastic skin with a tendency to contract making drops of liquid uninfluenced by gravity to adopt to a truly spherical shape. Capillarity deals with such equilibrium configurations describing macroscopic behavior of interfaces. This fundamental capillarity can be explained by the expression below which is commonly referred to as the Young–Laplace equation.

$$\mathbf{\Delta P = \sigma*(1/R_1 + 1/R_2)}$$

ΔP – Pressure Difference between the phases

R_1 and R_2 – Two principal radii of curvature of the droplet.

σ = Interfacial Tension of the Droplet Surface

The cohesion between the molecules of the liquid tends to surpass their tendency to disperse. Cohesion is present to a great extent in the interior phase of the liquid medium while the exterior mainly consists of atoms and molecules that would like to separate under the influence of thermal motion. The system now tries to attain minimum free energy state thereby undergoing spontaneous contraction. Solids cannot flow and hence do not undergo surface area minimization. Neither do the free energies of gases or miscible liquids offer any opposition to dispersion of one material over another. A more useful term is the interfacial tension of a given liquid surface is measured by finding the force across any line on the surface divided by the length of the line segment. Thus, the interfacial tension becomes a force per unit length, which is equal to the energy per surface area.

Surface Tension

Surface Tension is a characteristic property of a liquid that attributes to the attractive forces between the molecules of a liquid thus holding the liquid together.

Surface tension can therefore be quantified in terms of the various intermolecular forces acting on a unit length at the liquid-air interface. Hence it is defined as the "Perpendicular force acting on the unit length of the surface of a liquid.

$\gamma = F/l$

Surface tension is typically measured in N/m. It is affected by factors like intermolecular forces, hydrogen bonding and temperature. As a general rule the greater the proportion of the polar groups (e.g. O-H groups) the greater the attractive forces between them. Strong attractive forces give rise to high surface tension thus making liquids to form discreet droplets on a surface rather than dispersing and wetting it completely. Increased temperature causes reduction of surface tension due to reduced inter molecular attraction. Surface tension produces several observable phenomena like the capillarity and spreading of oil on water. *Table 2.1* lists the surface tensions of commonly used fluids.

Hydrophobicity

Superhydrophobic behavior cannot be exhibited by a surface that is not hydrophobic to begin with. This section discusses the basis for chemically treating a surface with hydrophobic coating.

Physio-Chemical Basis

Contact Angles on surfaces are defined using water as the liquid medium. Hence the behavior of water and its interaction with various surfaces help in defining the surface properties. Water is a polar substance, which accounts for its ability to interact with ionic surfaces. Bulk liquid water is strongly influenced by hydrogen bond interactions, which are composed of several covalent O-H bonds. The hydrophobic effect can be explained in thermodynamic terms and primarily deals with the interaction of the solid – liquid boundary.

$\mathbf{\Delta G_s = \Delta H_s - T\Delta S_s}$

ΔG_s - The free energy of solvation

ΔH_s – The enthalpy of solvation

ΔS_s – The entropy of solvation.

At room temperature, the *enthalpy* of solvation is negligible while the entropy is negative causing increase in free energy. At much higher temperatures hydrogen bonding diminishes and entropy is negligible and enthalpy dominates which is unfavorable in terms of hydrophobicity. A surface when treated with the right chemicals can be made resistant to wetting by water. A common understanding of hydrophobic behavior is associated with the demixing of oil and water. Several materials can be coated on a surface to make it hydrophobic out of which the most commonly used ones are rich in hydrocarbons, fluorine or siloxane. A well known hydrophobic material is polytetrafluoroethylene (PTFE), which has trade name of Teflon. The fluorine has the highest

electro negativity in the periodic table and it tends show lower critical surface tension due to a stable covalent bond. The critical surface tension is unique for any solid and is determined by plotting the cosine of the contact angles of liquids of different surface tensions and extrapolating to 1. Contact Angles vary for different liquids on different substrates based on the individual properties of each of them. Listed in *Table 2.2* are the contact angles of water on various smooth surfaces.

Silane Treatment of Surfaces

Silanes are primarily any of the series of covalently bonded compounds containing the elements Silicon and Hydrogen, having the chemical formula Si_nH_{2n+2} where n=1,2,3..

The silanes are structural analogues of the saturated hydrocarbons (alkanes) but are much less stable because the Si-Si bond has strength slightly lower than the C-C bond. In a surface treatment perspective silanes are silicon chemicals that possess a hydrolytically sensitive center that can react with inorganic substrates such as glass to form stable covalent bonds and possess an organic substitution that alters the physical interactions of treated substrates.

Table 2.1 - Surface Tensions of common fluids

Name	Surface tension @ 20 °C (mN/m)
Acetone	25.20
Ethanol	22.10
Glycerin	63.4
Mercury	425.41
Water	72.80
Benzene	28.9
Castor Oil	39
Olive Oil	35.8
Liquid Petroleum	33.1

Along with several other applications silanes are used to modify the surface energy or wettability of substrates. These silanes unlike the normal silanes (which are used as coupling agents in adhesive applications) do not impart chemical reactivity to the substrate. Hence they are termed as non-functional silanes. They are grouped as hydrophobic and hydrophilic silanes.

The main classes of hydrophobic silanes are as follows.

-Methyl

-Linear Alkyl

-Branched Alkyl

-Fluorinated Alkly

-Aryl

-Dipodal

Table 2.2 – Water Contact Angle on Surfaces

Smooth Surface	**Water Contact Angle (θ)**
Heptadecafluorodecyltrimethoxysilane	115°
poly(tetrafluoroethylene)	108 - 112°
poly(propylene)	108°
Poly(ethylene)	88 -103°
Poly(styrene)	94°
Dimethyldichlorosilane (Smooth Treated)	95 – 105°
Diamond	87°
Human skin	75 – 90°
Silicon (Etched)	86 - 88°
Steel	70 - 75°
Gold (Typical)	66°
Talc	50 - 55°
Platinum	40°
Soda Lime Glass	< 15°
Gold (Clean)	<10°

Surface modification is maximized when silanes react with the substrate surface and present the maximum number of accessible sites with appropriate surface energies. Silanes with alkyl groups such as butyl or octyl are hydrophobic. Alkoxysilyl groups, which are attached generally, help in the penetration, curing and bonding of silane with the substrate rendering the surface with hydrophobic property. *Table 2.3* lists the critical surface tensions of various materials.

Self-Assembled Monolayers (SAMs)

A Self-Assembled Monolayer (SAM) is formed when surfactant molecules spontaneously adsorb in a monomolecular layer on surfaces.

Table 2.3 – Critical Surface Tensions of Surfaces

Smooth Surface	Critical Surface Tension (dynes/cm)
Heptadecafluorodecyltrimethoxysilane	12
poly(tetrafluoroethylene)	18.5
Soda Lime Glass (Wet)	30
poly(propylene)	31
Poly(ethylene)	33
Poly(styrene)	34
Paraffin wax	25.5
Poly Vinyl Chloride	39
Copper	44
Nylon 6/6	45 – 46
Soda Lime Glass (Dry)	47
Fused Silica	78
Titanium Dioxide (Anatase)	91
Ferric Oxide	107
Tin Oxide	111

The self – assembly process involves the association of molecules into well-ordered domains. SAM's generally render a permanent modification of the surface due to the chemical bond that is formed by the silanes used. Common long chain alkyl silanes used in the formation of SAMs are simple hydrocarbon, fluoroalkyl and end-group substituted silanes. SAM's can be formed with silanes using simple solution deposition process. Silanes can have more than one hydrolysable group and those with one group finally form a single oxane bond with the substrate accompanied by the loss of water. The selection of a hydrophobic silane for treatment of a surface depends on several factors like the type and concentration of the hydroxyl groups on the surface, hydrolytic stability of the bond formed and the physical dimensions of the substrate features.

Contact Angle measurement

The two approaches to making contact angle measurements of a drop on a surface, which is introduced in this section.

Goniometry

A simple goniometric measurement involves a goniometer scale that indicates the measure of the contact angle of the drop when viewed manually from the side of the drop. For computer interfaced goniometry the horizontal microscope is replaced by a camera, which is interfaced with a computer program that fits a circle to the drop section and determines the angle with respect to the projected substrate surface. Goniometry techniques can be used over a wide range of substrates and smaller volumes of liquid. Since goniometry involves either manual or tool based fitting of the contact angle geometry it can be error prone. Hence multiple measurements are used to adequately characterize a surface.

Tensiometry

A tensiometric method involves calculation of contact angle by measuring the forces of interaction as the liquid makes contact with the solid surface. Liquid surface tension and solid geometry are required parameters in order to establish the contact angle from the forces.

Characterization of Static Wetting Behavior

The experimental wafers for the superhydrophobic tests in this section are the ones fabricated by the process discussed in the previous chapter. This section explains the hydrophobic treatment of the structures surfaces followed by a detailed contact angle analysis of a water droplet on each of these wafers.

Wafers for Hydrophobic Treatment

Fabricated Wafers – Brief Discussion

The wafers used for the preparation of superhydrophobic samples were obtained by a glass drawing and fusing process as described in the previous chapter. Two types of borosilicate glasses with slightly varying composition were used as the initial core and cladding glass performs. The glasses had a slightly varying composition making one more etchable than the other. The glasses were drawn together in the draw tower, bundled in a hexagonal casing and redrawn. The double drawn fibers were re-bundled again in a similar fashion and drawn the third time. The triple drawn fibers were fused in a glass bundle in a fusion furnace.

The multiple drawing and bundling were to attain a highly periodic multicomponent glass surface with extremely small feature sizes. The fusion helped eliminate the interstitial spaces between the bundled fibers thereby resulting in a well-fused array of glass structure. The fused bundle was sliced and polished to a good degree of finesse with respect to the feature size. Several sliced wafers were etched with ultrasonic agitation in a series of HF solutions as listed in the previous chapter (*Fig. 2.7*). The glasses have a definite etch rate contrast, which can be accounted by their difference in borate content. The cladding glass (Schott 8487) etches at a faster rate relative to the core glass (Schott 8330). This results in the regions containing the core glass protruding out from an etched back cladding background. These protruding features are termed as nanocones since they resemble a sharp tipped cone. The achievable lattice constant of the nanocones was 1.6 μm.

The profiles of the etched cones were controlled by using various concentrations of pure HF as well as buffered HF solutions. The etch time controlled the completeness of the etching process in order to obtained nanocones that were neither incomplete nor overetched. The detailed etching process and characterization is explained in the previous chapter. The aspect ratio of the cones was geometrically calculated from the SEM images. Structures with aspect ratios ranging from .3

to 15 were obtained. The buffered HF solutions contributed to the lower aspect ratio features and the pure HF solutions rendered features with higher aspect ratio.

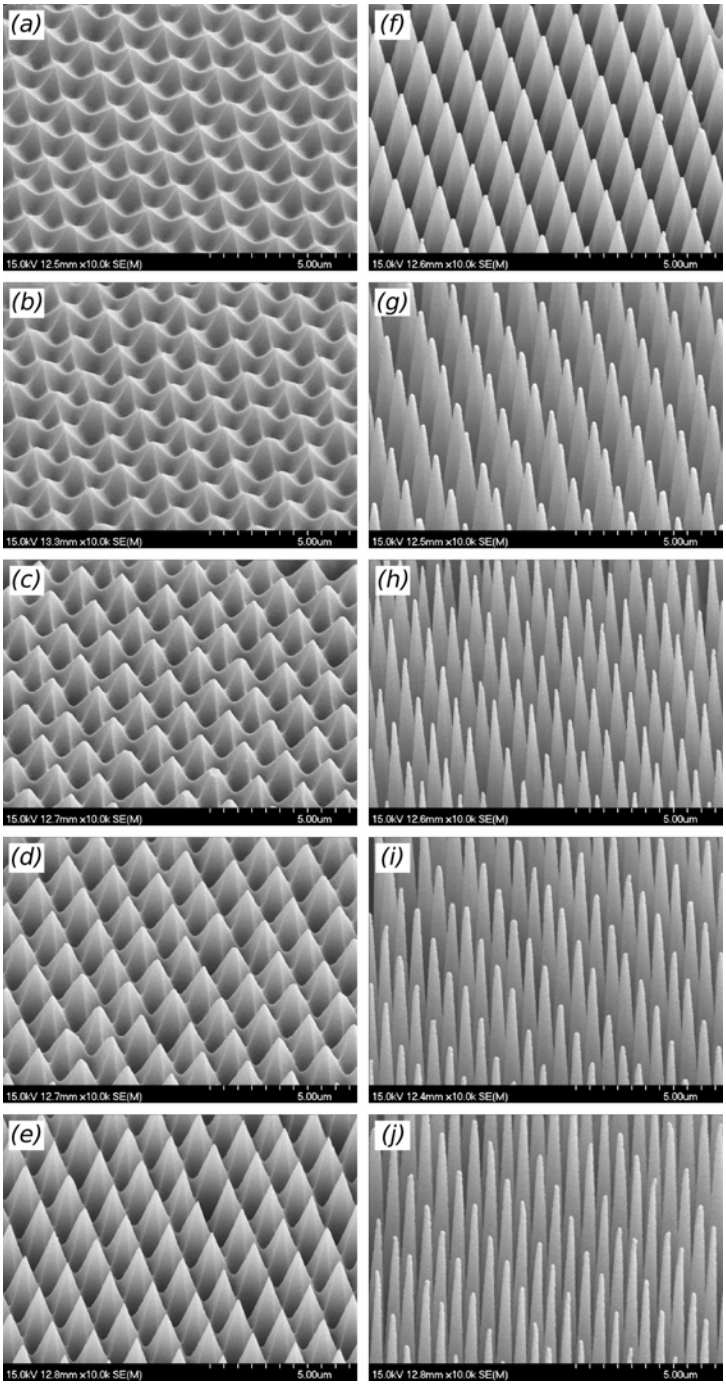

Fig. 2.7 – Etched series of nanocone glass arrays for the superhydrophobic tests. Figure is taken from [1.1]

Application of the Self-Assembled Monolayer

All of the etched wafers along with a flat unstructured homogeneous microscope glass slide were the chosen samples for treatment with the hydrophobic SAM. The first step in the treatment involves the complete immersion of the sample in a beaker containing 1% solution of tridecafluoro-1,1,2,2-tetrahydrooctyl trichlorosilane *(Fig. 2.8)* in hexane for 30 minutes. A smooth surface treated with octadecyltrichlorosilane can give a contact angle of around 102° to 109°, which is highly hydrophobic. A fluorinated alkylsilane provides an even better hydrophobic surface treatment by oxane bond formation with hydrogens of the hydroxyl groups on the surface. This results in complete and conformal shielding of the polar regions of the wafer by a non-polar interface. The hexanes are unreactive and primarily serve as an inert non-polar solvent. Hexanes, used as a suspension medium offer good coverage of the substrate by the fluorine-terminated monolayers. The samples are thermally cured by drying and heating in a furnace at 110°C for 15 min. They were finally cleaned and cleaned in isopropanol with ultrasonic agitation. The samples are allowed to thoroughly dry for at least 24 h at room temperature before testing. After allowing complete curing the samples are given a rough test for superhydrophobic behavior. Generally a drop of water is dispensed on the surface of the sample through a water dispenser and its behavior is noted. The most primary thing to look for in a manual test is whether the SAM has coated the surface well rendering a uniform hydrophobic surface.

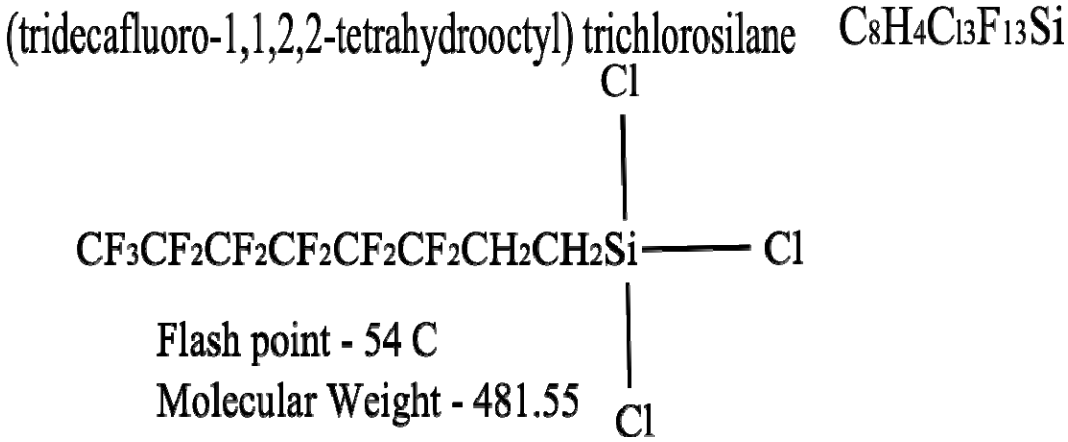

Fig. 2.8– Silane for hydrophobic treatment

This is indicated by absence of any sticky droplets or regions with hydrophilic behavior. The next step involves an estimate of the degree of superhydrophobicity of a surface, which can be made by just observing the dynamic behavior of dispensed water droplets. Excellent superhydrophobic behavior is observed in surfaces, which do not allow any water droplet to stay on its surface. Droplets on such surfaces get completely repelled just on contact with the surface with very high contact angles. Surfaces that show very high contact angles and small rolling angles also have good superhydrophobic properties. For surfaces that does not let the water roll off easily contact angle observation can be done.

All the wafers treated with the hydrophobic SAM showed reasonably agreeable hydrophobic-superhydrophobic behavior based on their aspect ratios. They were chosen for the nest step, which was the formal measurement of the dynamic contact angles.

Imaging of Drops and Rolling Angle Measurement

This section gives the experiment for imaging the advancing and receding drop profiles on the wafer. It also discusses the rolling angle measurements. The experiment is followed by a theoretical discussion of the physical model implemented to analyze the drop shape and calculate the contact angle.

Contact Angle

The setup for contact angle measurements consisted of a goniometric arrangement where the drop was observed from the side as shown in *Fig. 2.9. The* wafer was placed on an optical stage with controllable x y and z movements with its treated structured side facing up. A graduated dispenser with a micro-tipped stainless steel needle that served as the water droplet dispenser was clamped well above the wafer. The minimum dispensable volume of the syringe is 1 µl. A small needle tip helps minimizing the distortion of the drop due to adhesion of the fluid to the needle.

A high speed Mikrotron black and white video camera with a lens mount was lined up horizontally to focus well on a droplet that is being dispensed on the wafer below. The camera was 12V DC powered and run by a python program from the computer terminal. A 2.5X, 4X objective microscope lenses were used to focus on the drop to obtain the appropriate magnification. The camera was interfaced with a python based tool for capturing images. A fiber optic illuminator was placed behind the drop setup to light up the drop for achieving good contrast image capture. The liquid volume chosen for each of these drops was about 10 µl. The

lighting and focus was adjusted and the needle location is set so that the needle is visible in the images.

The advancing contact angle was measured as the droplet was slowly dispensed (as the volume of the droplet got bigger). Following that the receding contact angles were measured by slowly withdrawing the liquid from the surface of the wafer. Advancing and receding angles were measured from at least five different spots on the surface of the wafer to avoid any large deviation of measurement due sticky spots or defective regions. Advancing and receding drop images were taken from every region selected. For best approximation purposes images a sapphire lens ball (3mm diameter) was placed on the wafers. The balls were places in the same spots from which the drop images were taken in order to obtain best correspondence of the drop and ball images. It was used in determination of the baseline which if incorrectly calibrated can lead to inaccuracies in the contact angle values.

Rolling Angle

The rolling angle was measured by placing a droplet on the surface followed by slowly introducing a gradual tilt to the surface till the droplet rolls of the surface.

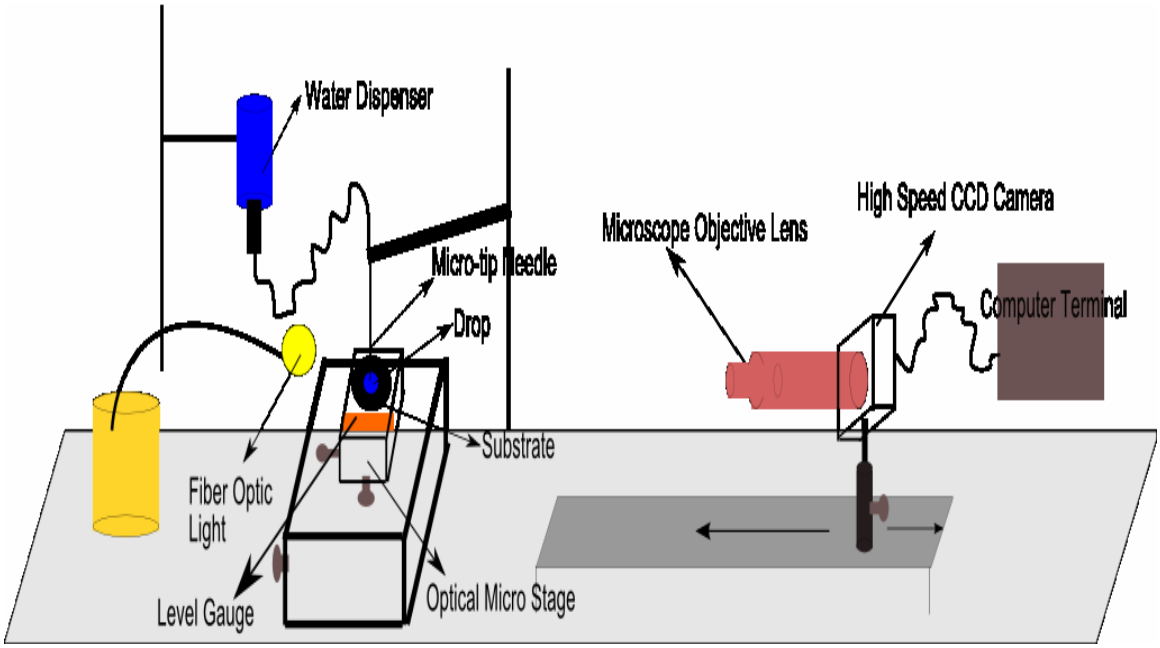

Fig. 2.9 - Goniometric setup for contact angle measurement

An accurate measurement of the rolling angle is obtained by ensuring that the two faces of the wafer are very parallel. The standard 10µl drop was dispensed on all of the substrates followed by the withdrawal of the needle tip from the drop. The wafer was placed on a highly level optical stage with x, y, z micrometer controls. A double-sided tape was used to carefully attach the wafer to the stage to prevent it from sliding during the tilt. A precision level gauge was used to ensure the initial evenness of the wafer base. A tilt in the x direction was introduced through the micrometer controls till the droplet rolled off the surface completely and the degree of tilt was noted in the level gauge. Surfaces on which the drops did not roll off can be characterized as having a high hysteresis due to lower aspect ratio and vice versa *(Fig. 2.10)*.

Surfaces on which droplets never underwent a tilt before they rolled off had a roll off angle 0° and those, which never rolled, were treated to have a roll off angle 90°.

Axisymmetric Drop Shape Analysis

Several works have been published discussing methods and approaches for accurate calculation of the contact angle. In this section we discuss the model was implemented for drop shape analysis [2.13]. The model is based on a comparison and error minimization technique of the experimental data with the theoretical one.

Approach

A small drop will always tend to be spherical. The gravitational effects decrease as the cube of the linear dimension whereas the surface forces decrease as the square of the linear dimension of the drop and both effects determine the effective shape of the drop.

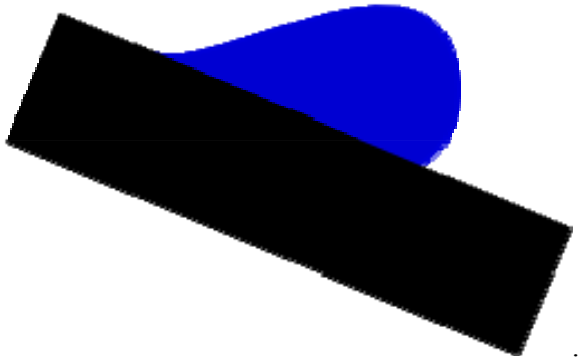

Fig. 2.10 – Effect of hysteresis during roll-off

A drop is generally termed as a pendant or a sessile drop.

Pendant Drop – A drop that hangs from a tip generally elongates, as it grows larger because the variation in hydrostatic pressure eventually becomes appreciable in comparison with that given by the curvature of the apex.

Sessile Drop – A sitting drop or a continuous drop of liquid on a solid substrate under steady state conditions.

In our experiment droplets are observed in their sessile state. An axisymmetric drop is considered to be symmetric about its z (vertical) axis. Several numerical methods have been established to study a drop shape and calculate parameters such as the interfacial tension and contact angle. The most basic approach involves a systematic comparison of the experimental profile of a drop (obtained from a captured image) with the theoretically calculated one followed by an error minimization method to get the most optimal approximation of the drop profile. Since the experimentally obtained drop shape is used in calculating the discrepancy with the theoretical curve the images have to be of very good quality. The theoretical curve is based on the Laplace equation explaining fundamental capillarity described in the previous section.

The approach that we have employed approach involves the steps mentioned below

- Experimental acquisition of images of advancing and receding drops on the various substrates (Discussed in the previous section)
- The numerical integration of Laplace equation with the appropriate boundary conditions
- Application of a suitable non-linear least squares optimization technique to fit a the drop profile
- Geometric computation of the contact angle by measuring the slope of the tangent to the drop plot and the three phase interface

Laplace model

Laplace equation is given by

$$\Delta P = \lambda^*(1/R_1 + 1/R_2) \quad \text{.....(2.1)}$$

ΔP – Pressure Difference between the phases

R_1 and R_2 – Two principal radii of curvature of the droplet.

σ = Interfacial Tension of the Droplet Surface

If gravity is the only outside force acting on a droplet pressure difference can be expressed as

$\Delta P = \Delta P_0 + (\Delta\sigma)*g*z$……(2.2)

ΔP_0 = Pressure Difference at a selected datum plane

$\Delta\sigma$ = Density difference of the two bulk phases

g = Acceleration due to gravity

z = Vertical height of the drop from the datum plane

Let us consider an axisymmetric sessile drop whose apex lies in the origin (O) of the coordinate system *(Fig. 2.11)*. At the apex R gives the radius of curvature.

$1/R_1 = 1/R_2 = c$

c = curvature at the origin of the coordinates

$t = (\Delta\sigma)*g$ = capillary constant

$\Delta\sigma = .9982\ g/cm^3$

$g = 9.8\ m/s^2$

$\lambda = 72.785\ dynes/cm^2$

$\Delta P_0 = 2*c*\lambda$……..…….(2.3)

From equations (1), (2) and (3) and from Fig 2.7 we get a set of ordinary differential equations which are expressed as a function of the arc length s.

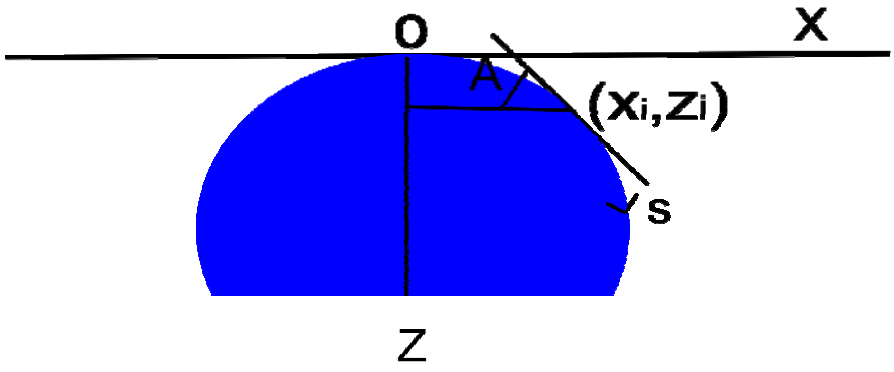

Fig. 2.11 – Sessile Drop for Axisymmetric Drop Shape Model

dx/ds = cosA……..…… (2.4)

dz/ds = sinA……..……. (2.5)

dA/ds = 2*c + t*z – sinA/x…….…….. (2.6)

Here A is the angle subtended by the tangent, which becomes the liquid contact angle at the three-phase boundary.

Boundary conditions ***(Note****: The actual boundary conditions implemented for the contact angle calculation takes into consideration the needle tip present in top of the drop. Hence they are not similar to the perfectly sessile drop assumption as shown in figure. The parametric limits were user defined and based on selected boundary of the droplet segment to be analyzed).*

x(0) = z(0) = A(0) ……..……...…….. (2.7)

At the apex where s = 0, which is the origin O

dA/ds = c ……...…….. (2.8)

For a given curvature and capillary constant integration of the above expressions can plot a theoretical curve. A Runge-Kutta method was used to solve the equations. The integration can be stopped at various limits of s, A, x or z.

Error function computation

In order to compare the theoretical and experimental profile of the drop an appropriate translation and rotation of the drop coordinate system must be done *(Fig. 2.12)*. This corrects any imperfections in the horizontal and vertical alignments of the camera and also takes into consideration the right magnification of the image obtained. Calculating the pixels per millimeter of the image does conversion of from image coordinates to plot coordinates. A sapphire ball of known 3mm diameter is placed in every corresponding region where the drop is dispensed for advancing and receding image capture. The lens ball is highly spherical and gives a good approximation to perfectly spherical and symmetrical drop. However an elliptical fit of the data points is used for achieving better correction of vertical and horizontal misalignment. The elliptical fit code sequence for a sapphire ball image provides the necessary parameters for the coordinate transformation (image rotation and substrate baseline shift) of the actual drop image.

The equations after transformation become

q1 = X0/R0……..…… (2.9)

q2 = Z0/R0…….…… (2.10)

q3 = R0…….…….……...…….. (2.11)

q4 = (Δσ)*g .R0^2/λ……....…….…..... (2.12)

The computed error function is given by

En = ½*distances (experimental_drop_points, theoretical_drop_points)^2

Program Tool

The logic for axisymmetric drop shape analysis was implemented in Python. The images obtained were first run through the code sequence for establishing the baseline of the substrate and derotating an image coordinate to plot coordinate. This was followed by the contact angle calculation.

Flow

User interface, theoretical and experimental calculations were Python coded. The flow of the programming sequence is depicted in the following page *(Fig. 2.13).*

Fig. 2.14 represents the screen shots of the tool i) establishing the baseline with a sapphire ball image ii) advancing drop image fit iii) receding drop fit

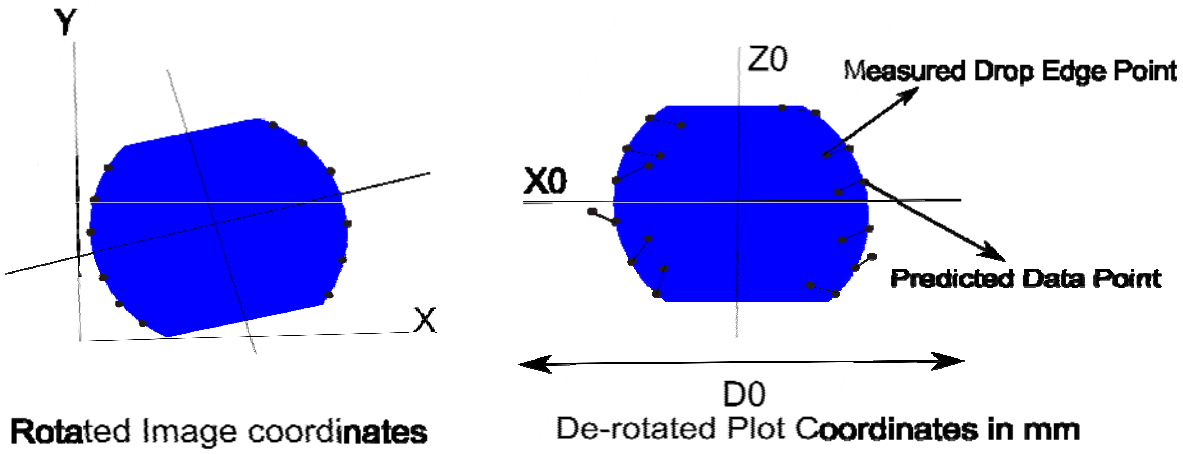

Fig. 2.12 – Sessile Drop (With Needle) - Experimental and Theoretical Drop Fit

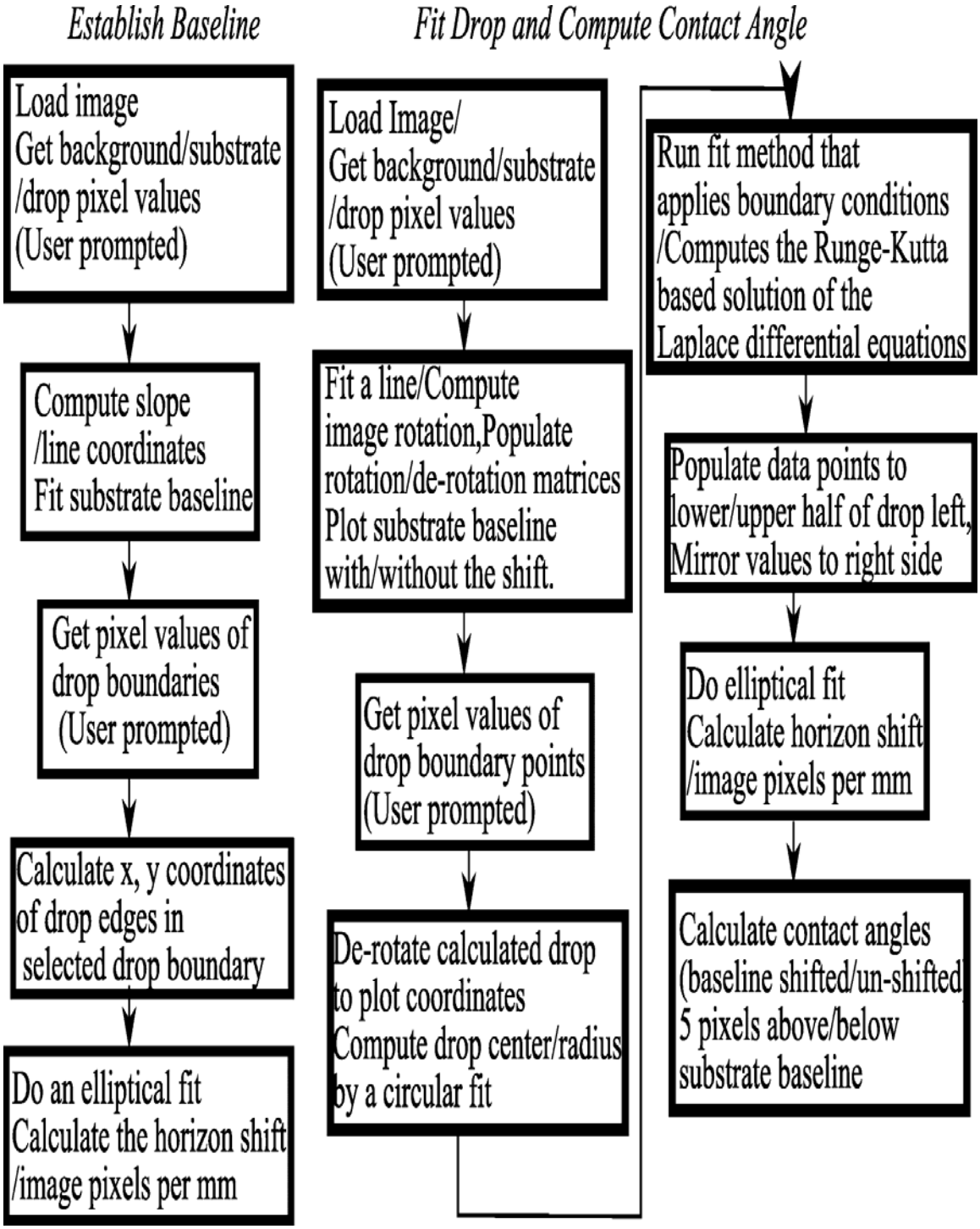

Fig. 2.13 – Contact Angle Computation Model – Program flow

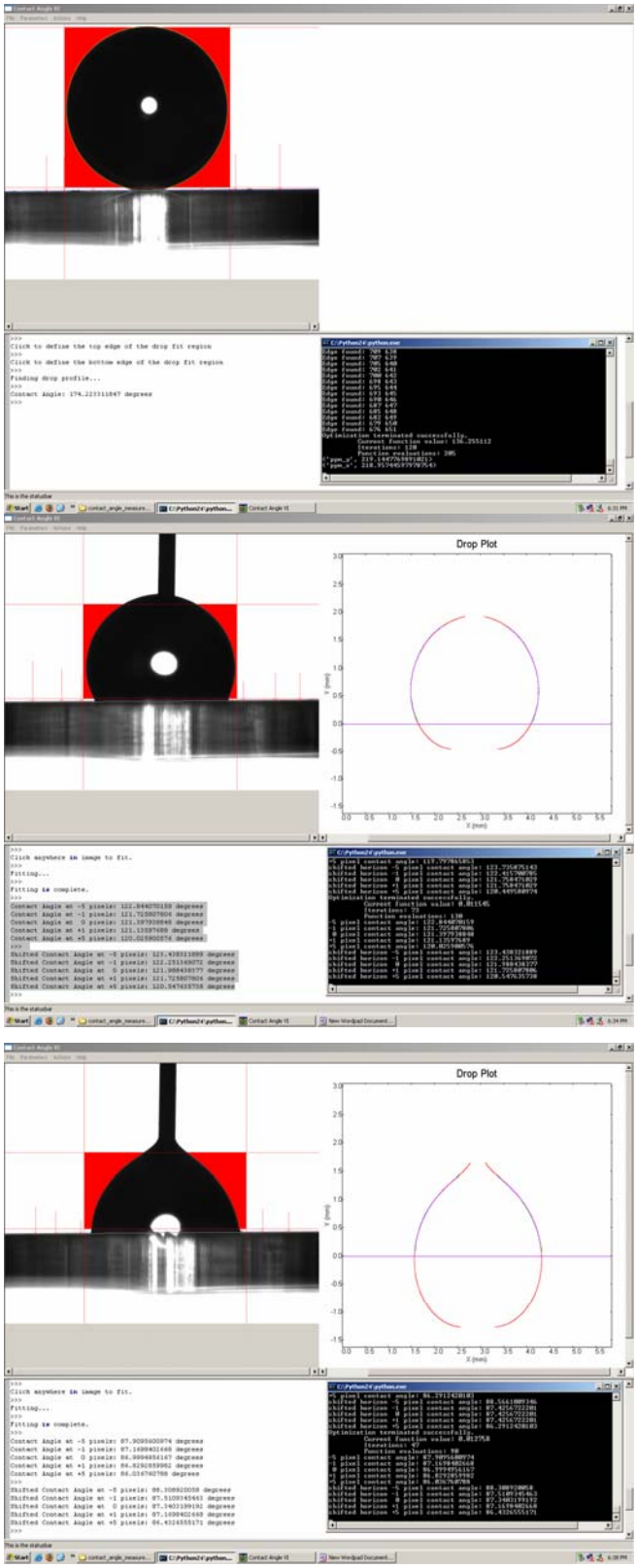

Fig. 2.14 – Screenshots from the drop shape analysis tool

Analysis and Results

Measured Wetting Angles

Table 2.4 represents the contact angles obtained for the etched wafers including a flat coated (with SAM) glass slide. *Table 2.5* represents the rolling angles of all the wafers.

Images of Drop Shapes

High quality drop images were crucial for accurate drop shape analysis. This was ensured by a sturdy experimental setup. The wafer was first imaged with a sapphire ball positioned on its surface. Imaging an advancing and a receding drop in the same region corresponding to the sapphire ball followed this.

Fig. 2.15 – Fig. 2.24 represent the images of the substrate taken with an advancing drop, receding drop and sapphire ball in a given region of the substrate. The drops are taken with the needle tip.

Table 2.4 –Advancing and Receding Contact Angles of the Etched Wafers

Wafer No.	Advancing Contact Angle (°)	Receding Contact Angle (°)
Slide	120	90
291	114.8	81.5
292	134.6	87.5
293	150.8	109.4
294	170.8	120.5
295	179.4	171.8
296	172.6	164.2
297	173.4	169.6
299	169.7	165.5
300	178.9	175.2
301	174.0	171.0

Table 2.5 –Rolling Angles of Etched Wafers

Wafer No.	Rolling Angle (°)
291	90
292	90
293	90
294	90
295	40
296	15
297	0
299	0
300	0
301	0

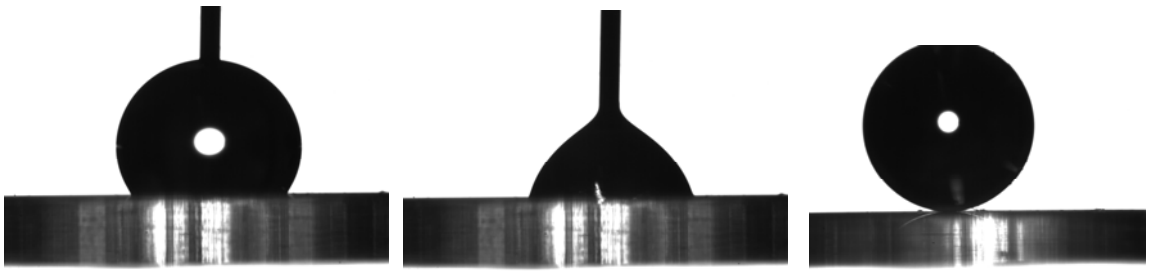

Fig. 2.15 – Drop Shape Images of Sample 291

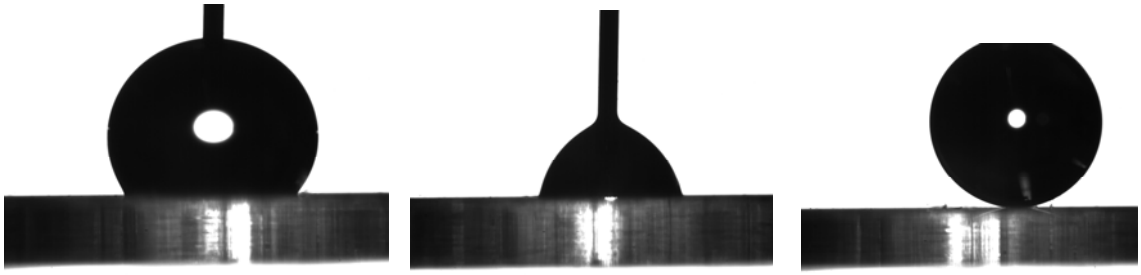

Fig. 2.16 – Drop Shape Images of Sample 292

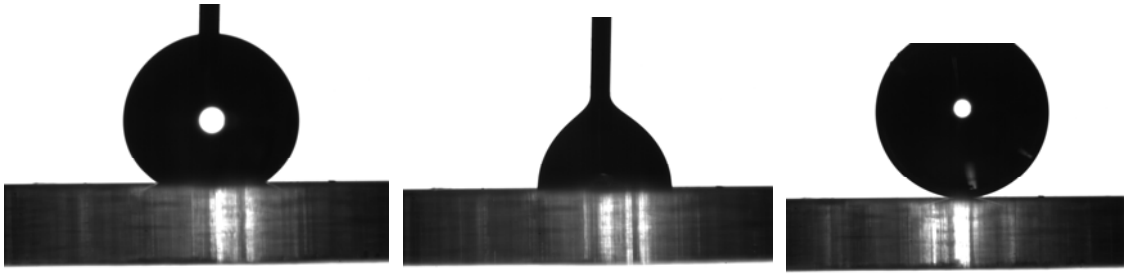

Fig. 2.17 – Drop Shape Images of Sample 293

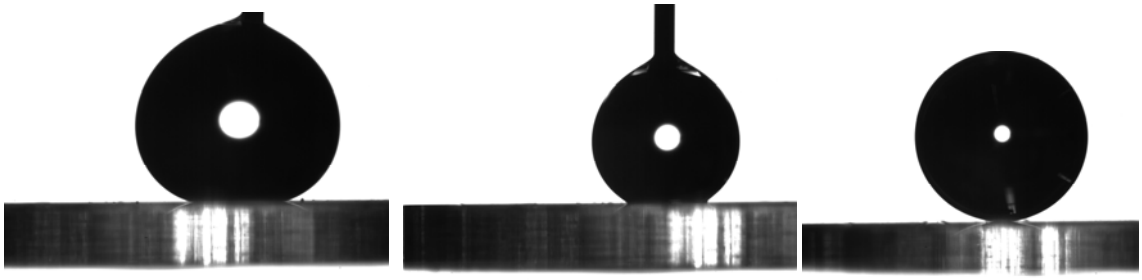

Fig. 2.18 – Drop Shape Images of Sample 294

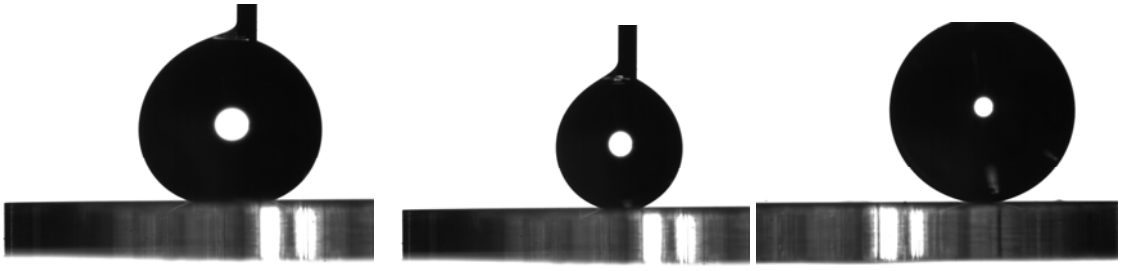

Fig. 2.19 – Drop Shape Images of Sample 295

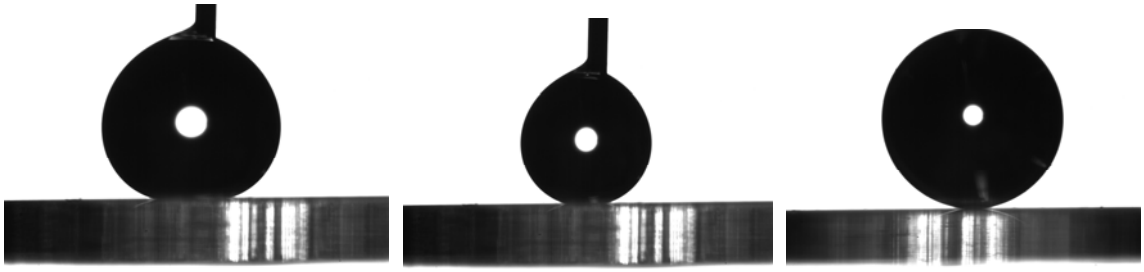

Fig. 2.20 – Drop Shape Images of Sample 296

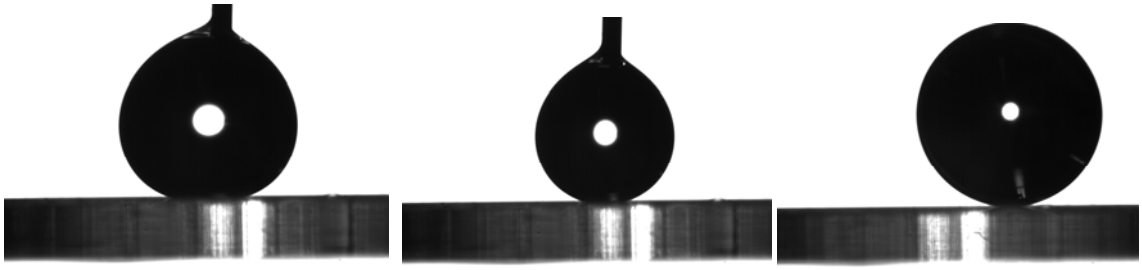

Fig. 2.21 – Drop Shape Images of Sample 297

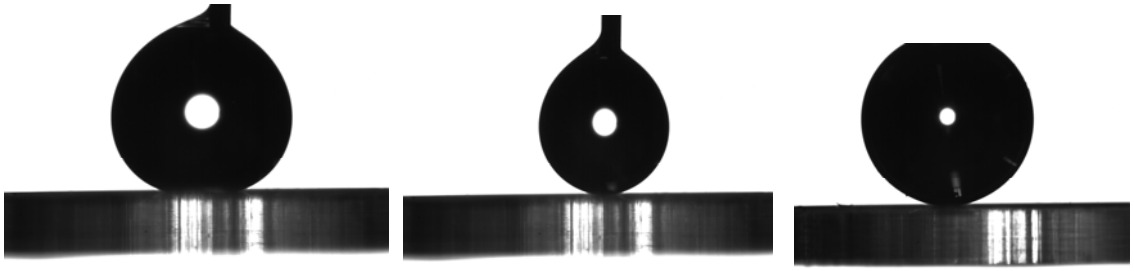

Fig. 2.22 – Drop Shape Images of Sample 299

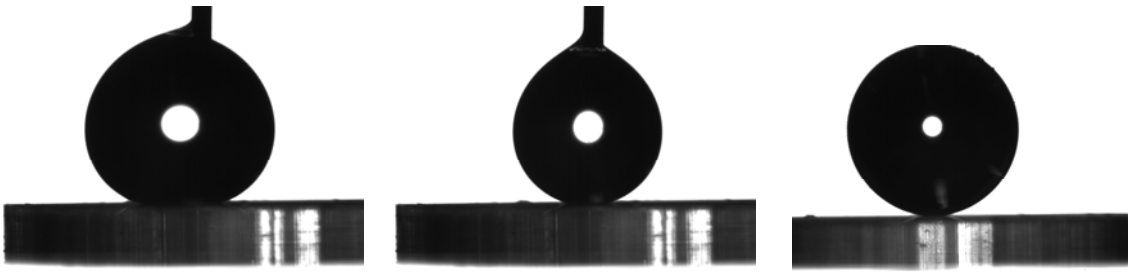

Fig. 2.23 – Drop Shape Images of Sample 300

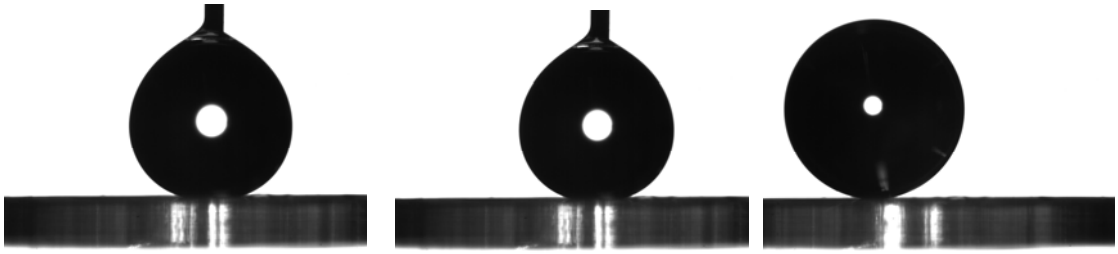

Fig. 2.24 – Drop Shape Images of Sample 301

Interpretation of the Results

This section discusses the Cassie and Wenzel states of structured surfaces in terms of a surface tension model [2.14]. The surface tension model integrates the surface tension around each of the nanocone features to evaluate the downward pressure that can be supported by the features. The model also shows that the optimal design parameters for a superhydrophobic surface are the lattice constant, nanocone apex half-angle and the Young's contact angle.

Surface Tension Model of a Nanocone

In order to analyze the effect of force on the vertically aligned nanocones it is useful to first consider a single nanocone, which holds a liquid drop at the upper section (Cassie state) as shown in *Fig. 2.25.* The surface curvature caused near the solid surface is ignored and a flat surface liquid contact angle is considered. The force acting vertically on the water is obtained by integrating it around the three-phase boundary line and can be expressed in terms of surface tension. The force increases linearly with the depth of penetration of the liquid.

$F = 2*\pi*\gamma*(d*\tan\varphi)*\sin(\theta_0 - 90 - \varphi)$

γ = surface tension of the liquid

θ_0 = liquid-solid contact angle (flat surface)

$d*\tan\varphi$ = radius of the three phase circle

φ = nanocone half apex angle

Since **P = F/A** the restoring pressure for an array of nanocone can be expressed as

$P = 2*\gamma*\sqrt{(\pi\rho\rho\sin\varphi)}*\sin(\theta_0 - 90 - \varphi)$

ρ = density of nanocones

P = fraction of the wet area relative to projected area

Fig. 2.26 shows the plot of the pressure with respect to the apex half angle. The following can be observed

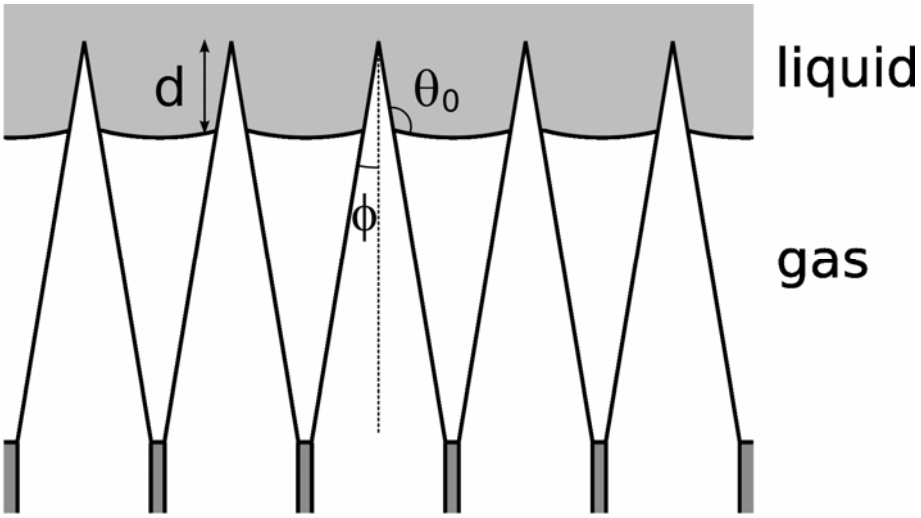

Fig. 2.25 – Liquid on a vertically aligned nanocone array. Figure is taken from [1.20]

- High aspect ratios characterized by low values of φ have low restoring pressure and a reduced depth of penetration.

- Low aspect ratios characterized by high values of φ experience considerable restoring pressure caused by the reversed vertical surface tension forces which pulls the liquid further down into the features.
- At an apex half angle $\varphi = \theta_0 - 90$, the restoring pressure drops to 0 making the surface tension forces completely horizontal.

Thus we can see that maximization of the restoring pressure can give optimal parameters for a successful design of hydrophobic to superhydrophobic surfaces. The parameters are mainly the lattice constant (spacing between the features), apex angle and contact angle.

Wenzel – Cassie Transition

Fig. 2.27 shows a plot of the dynamic contact angles of the wafers with varying aspect ratios. The aspect ratios can be compared to the half apex angle discussed in the previous section.

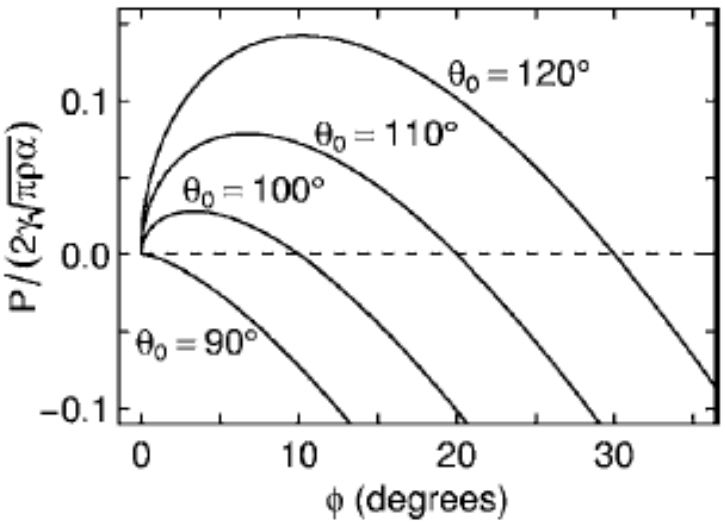

Fig. 2.26 – Restoring pressure as a function of the apex half angle.
Figure is taken from [1.20]

The values represent the mean of 5 different measurements of corresponding advancing receding and sapphire ball images taken at different spots on the surface of the wafer. An error bar is shows the standard deviation of each of these measurements. We can see that the advancing increases gradually with increasing aspect ratio and the rolling angles decrease. Hysteresis dominates in the lower aspect ratio regions due to low receding angles thereby making the droplets sticky and difficult to roll off.

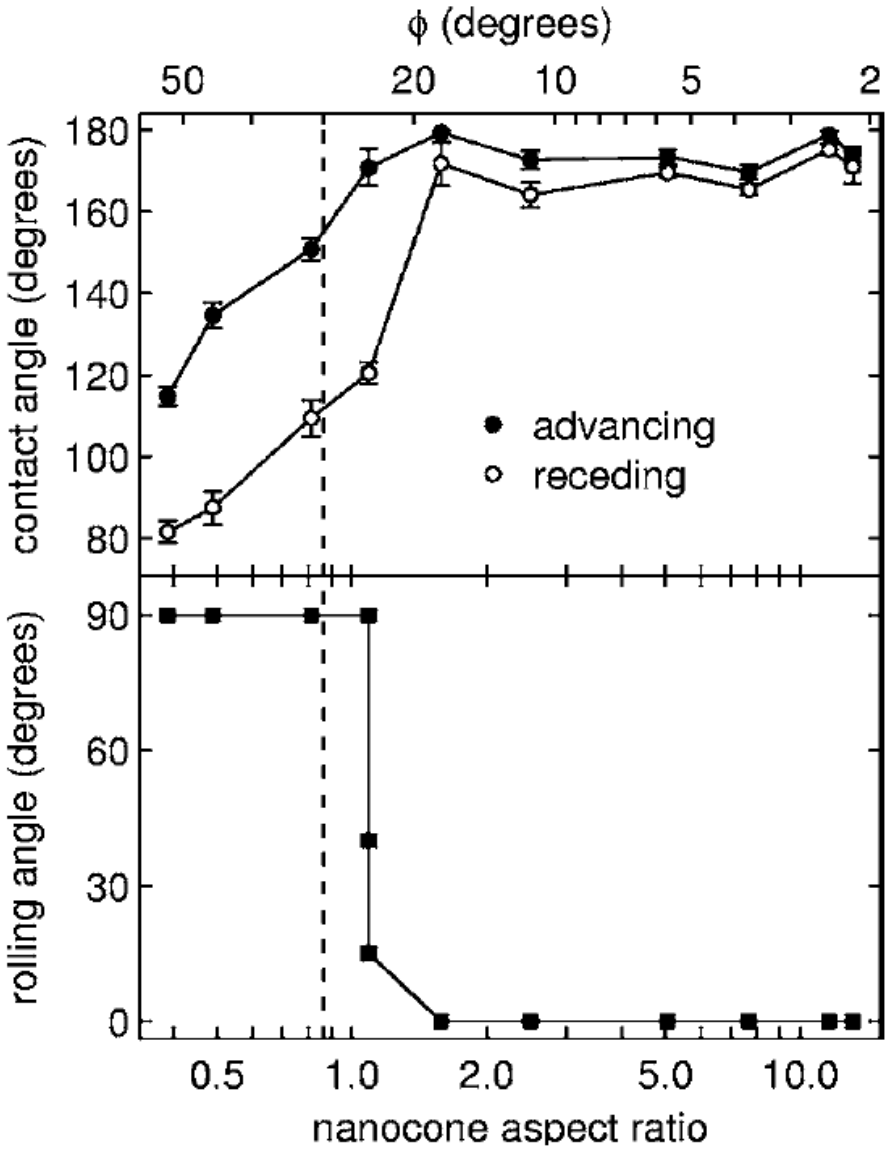

Fig. 2.27 – Dynamic Contact Angles of the Nanocones with varying aspect ratio. Figure is taken from [1.20]

Wenzel Regime

The Wenzel regime can be observed in aspect ratios ranging from .3 – 1. The presence of Wenzel state is primarily indicated by values of $\varphi > \theta_A - 90°$, which in agreement with the model discussed in the previous section, must pull the droplet down to a wetted Wenzel state.

Such surfaces do not roll off the surfaces at any inclination (indicated as 90°) primarily due to the dominance of hysteresis.

Fig. 2.28 represents the drop profiles and the corresponding surfaces of the Wenzel and the Cassie states.

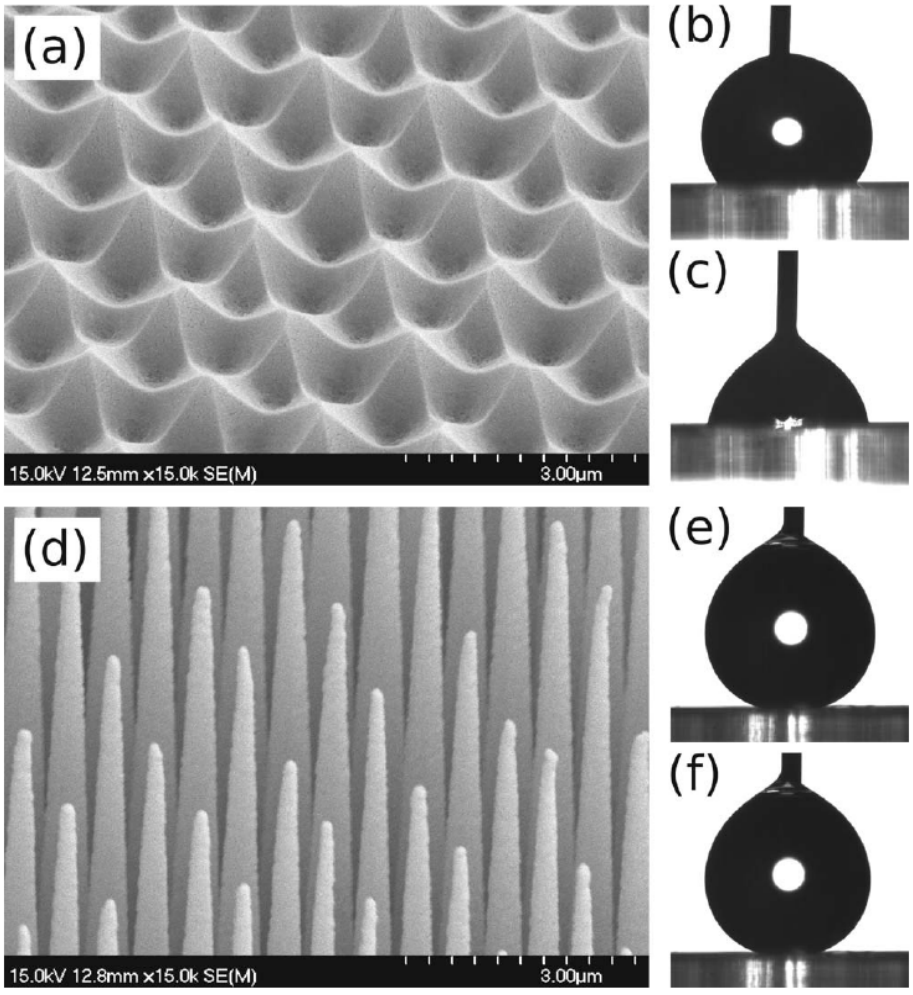

Fig. 2.28 – Surfaces resulting in a Wenzel drop (above) and a Cassie drop (below)
Figure is taken from [1.20]

Cassie Regime

Cassie – Baxter state takes over at higher aspect ratios and values of $\theta_A - 90° > \varphi > \theta_R - 90°$. For such a range of low half apex angles a poor restoring force results in the water being pushed upwards thereby trapping a layer of air under the liquid. The rolling angles undergo an abrupt change from the non-rolling Wenzel regime. For increasing aspect ratios the drops start to roll at smaller angles like 35° and 15° and then undergo a complete de-wetting state where they could not be balanced on the surface (indicated as 0). This sharp transition occurs when the apex angle is decreased from 32°. Thus, the Wenzel-Cassie transition is clearly observed as the aspect ratio of the nanocones was gradually increased.

Chapter 4

Dynamic Wetting Properties

Background

Literature Review

This chapter discusses a study of the electrowetting properties of structured surfaces. Devices for the electrowetting experiments were prepared after adding additional layers on the wafers fabricated from the process discussed in the first chapter. Electrowetting involves the contact angle based actuation of a droplet on a surface by the application of voltage. Electrowetting based droplet manipulation has been studied extensively for a wide range of applications [3.1, 3.2, 3.3]. A work describing the fundamental EW and EWOD principles for microactuation has been reported [3.4]. A detailed review on electrowetting from basics to applications has been recently published [3.5]. Several theoretical approaches in understanding and characterizing EWOD behavior have been reported. One broad category has been based on the energy minimization of interfaces. Work has been reported describing an energy-based model for estimating the electrowetting actuation force acting on a droplet during its wetting transition [3.6]. The other broad approach is based on the exploitation of the electromechanical forces that are responsible for the droplet movement [3.7]. In this chapter theoretical explanations of the electrowetting behavior are given based on the energy minimization approach, which is simpler and yet physically accounts for the observable phenomena. Three categories of surfaces were chosen for the experiments. The first was a low aspect ratio surface that was expected to exhibit the Wenzel regime of wetting. The second was a high aspect ratio surface that was expected to

exhibit the Cassie regime of wetting. The third was a plane and smooth surface. The nano-structured wafers were fabricated by a technique discussed in the second chapter of the thesis. The lattice contact of the features was 7µm. A conductive gold layer was coated by e-beam evaporation. Several works on material considerations for effectively reducing the voltage requirements of the EWOD process have been reported [3.8, 3.9]. It has been shown that a smooth and thin dielectric coating that has a high breakdown voltage and the presence of an ambient medium like oil can greatly enhance the effective contact angle change [3.10]. Parylene-C was used as the dielectric layer and was coated by a CVD process to a 1µm thickness. The wetting behavior of the surfaces was tested by application of dc voltage. Various voltage parameters like the threshold; saturation and breakdown voltages were studied and analyzed in each of the cases. Work describing the relationship between hysteresis and actuation potentials in an electrowetting system has been established [3.10]. The phenomena of contact angle saturation can be described as the absence of further wetting as the applied voltage is increased. At the onset of contact angle saturation the device fails to follow the Young-Lippmann's equation of electrowetting. A detailed study has been done on the phenomena of contact angle saturation [3.11]. The electrowetting parameters of the structured surfaces were analyzed. Several works explaining the electrowetting behavior on superhydrophobic surfaces have been reported. A work describing the dynamic electric control of droplets on superhydrophobic surfaces through the entire range of wetting has been reported [3.12]. A wetting process in structured surface exhibiting a superhydrophobic contact angle has been reported to involve a Cassie-Wenzel transition of wetting states [2.8]. A similar work has been reported on achieving completely reversible wetting on liquid marbles coated with hydrophobic material [3.13]. Here, we try and analyze the occurrence of transition of 'Cassie-Wenzel-Fully Wetted' states in all the wafers tested. The electrowetting tests were performed using both oil and air as the ambient medium. An ac voltage based actuation of droplets on superhydrophobic surfaces has also been reported [3.14].

A few electrokinetic phenomena

This section introduces the electrical double layer, which is the origin of several interesting and useful electro-kinetic effects. It also discusses briefly electro-osmosis, electrophoresis and dielectrophoresis.

The Electrical Double Layer

Studying the electrical charges at solid surfaces interfacing an electrolyte and the consequent potentials gives rise to a whole new range of electrical phenomena.

This is caused by the charging of the solid surface caused due to the differences between the ion affinities of the solid surface and the solution. A useful kind of charging is the 'Electrical Double Layer' as shown in *Fig. 3.1*. The Stern double layer model describes the EDL as a layer of ions and counter ions developed around a surface of a particle carrying a net charge. The surface charges induce counterions, which form a monolayer that is adsorbed directly on the surface, and are dehydrated. This layer of ions is referred to as the Stern layer. The counterions are electrostatically and rigidly attached to the surface charges.

The layer next to the Stern layer is the outer Gouy layer separated from the Stern layer by a Stern plane at a distance δ from the surface. The distance corresponds roughly to the radius of a hydrated ion. All of the counterions do not lie in the same plane because of their tendency to diffuse away thereby reducing in concentration further and further away from the surface.

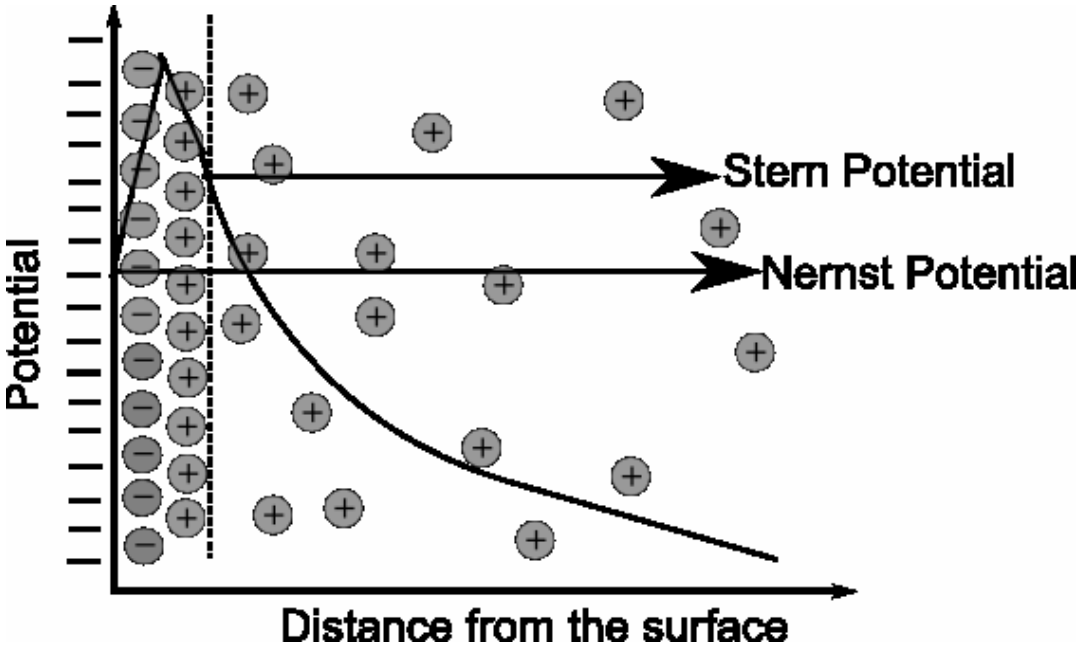

Fig. 3.1 – The Electrical Double Layer

Hence, an EDL contains an inner Stern layer of firmly bound ions and an outer diffuse layer of loosely bound ions. A boundary within this diffuse layer sets the limit for the specific particle and is called as the slipping boundary caused by the space charge distribution between electrostatics and diffusion. The zeta potential is this position dependent potential that is calculated within the plane of shear present in the space charge boundary. The zeta potential of the particle is calculated from the slipping boundary.

The effective thickness of the diffuse layer is defined by the Debye length, which is given by

$$\kappa = 2q2n/\varepsilon KT$$

q - Charge of the particle

n - Concentration of the positive (or negative) ions of the liquid

K – Boltzmann constant

T – Temperature

Electrically the EDL can be considered as a series combination of two parallel plate capacitors.

Electrophoresis

Electrophoresis is the migration of charged particles in a liquid in response to an electric field placed in a solution. The mobility of the molecule (which is its velocity divided by the electric field gradient) depends on several physical conditions, the size and shape of the particles of the medium and its net charge. It indicates the balance between the electric force that acts in favor of the motion and the frictional force that opposes it which is constant for a given ion under a given set of conditions.

The electrophoretic mobility a useful practical quantity given by the following equation.

$$\mu_p = z/6\pi\eta r$$

r – Radius of the particle

z – Net charge of the particle

Electro-osmosis

The diffuse part of the EDL moves when subjected to an electric potential. The tangential electric force applied along a charged surface a Columbic force is exerted on the ions of the EDL causing migration. For a solution like water the cohesive nature of the hydrogen bonding of its molecules the entire solution is pulled creating a uniform velocity profile across the solution. Electro-osmosis (EO) is the bulk liquid flow caused through a pore caused by a migrating ionic sheath. The volume of the solution transported per unit time is

$V = A\varepsilon E\zeta/4\pi\eta L$

A - Total effective area of the pores

ζ - Double layer zeta potential

L - Pore length

EO is very useful for creating EO flows due to its pressure building ability in contrast to the mechanical pressure driven flow and can also be driven by AC fields. An AC EO a time and frequency dependent field that interacts with the formed EDL generating a net force. The direction of the fluid remains the same due to the simultaneous cancellation of changing polarities and field directions. Velocity obtained through AC EO depends on the applied frequency and medium conductivity. Low frequencies give time for the space charge distribution causing smaller tangential fields and hence smaller EO velocities. At higher frequencies the charge in the EDL is smaller and impedance across the electrolyte dominates. The main advantage of AC EO is low driving voltage when compared to DC.

Dielectrophoresis

DEP is particle motion induced by spatially non-uniform electric fields and produces a force leading to directed motion of objects. The phenomenon mainly arises due to the difference in the magnitudes of the forces experienced by the electrical charges within an unbalanced dipole caused by a non-homogeneous electric field. A net imbalance in force causes the particles to migrate to a region of greatest field intensity *(Fig. 3.2).*

The DEP force is given by

$F = \frac{1}{2}\alpha V\Delta|E|^2$

α - Effective polarizability of the particle

E – Electric field

V – Volume of the particle

Generally for a particle that is more polarisable than the medium surrounding it the dipole tends to align itself with the field forcing it towards the high electric field region and vice versa. This can result in an attractive (positive DEP) or repulsive force (negative DEP).

The DEP acting on a homogeneous, isotropic dielectric sphere is given by

$F = 2\pi r^3 \varepsilon_m Re[(\varepsilon_p^* - \varepsilon_m^*)/(\varepsilon_p^* - 2\varepsilon_m^*)]\ \Delta|E|^2$

r - Radius

ε_m - Permittivity of the medium

ε_{m^*} - Complex permittivity of the medium

ε_{p^*} - Complex permittivity of the particle

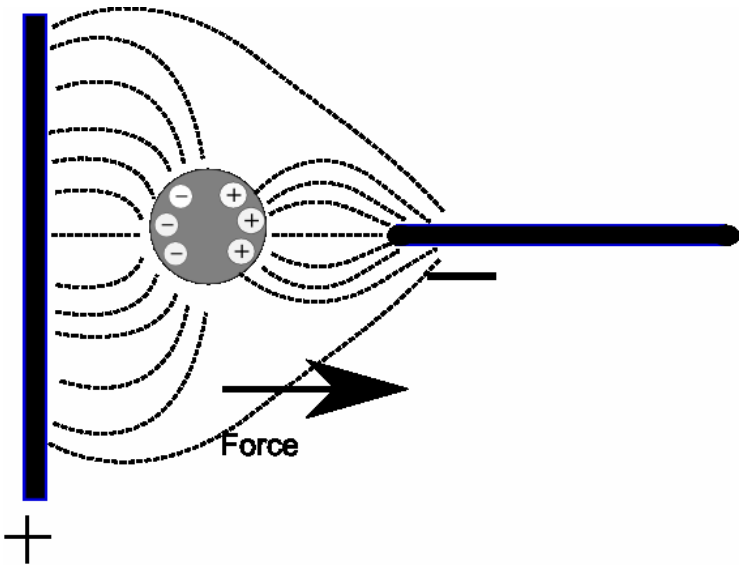

Fig. 3.2 – Dielectrophoresis

Electrowetting

This section discusses in detail the theoretical background and the principle of the electrowetting phenomenon. EWOD can bring about a change in the contact angle of a droplet on a dielectric coated device by the application of voltage. The principles of EWOD are discussed.

Theoretical Background

Introduction

Electrowetting is the modern version of the electro-capillarity principle, which was discovered by a Nobel laureate named Gabriel Lippmann in 1875. Lippmann discovered that by applying a voltage between mercury and an electrolyte a depression of the mercury, which is in contact with the electrolyte solution, can be obtained. It was explained that the effect occurred due to the changes in the charges of the Electrical Double Layer and the interfacial tensions of the mercury electrolyte interface. Following Lippmann several works have been published directly dealing with contact angle changes of sessile droplets sitting on conductive surfaces. Theses effects were referred to as 'Electrowetting' or 'General Electrowetting' or 'Continuous Electrowetting'. But the biggest drawback of the conventional form of electrowetting is the requirement of large voltages due to the larger charge separation in comparison to an electrocapillary setup.

This issue was addressed by introducing a major voltage drop across an inserted layer of insulator between the liquid and the electrode and this was called 'Electrowetting on Dielectric' (EWOD). In a EWOD setup as shown in *Fig. 3.3* an electrical double layer builds at the interface of the droplet and the dielectric and since the thickness of the dielectric is much larger that the EDL the total charge capacity of the system is increased.

Young's equation

Electrowetting is a combination of two fields, which are interfacial chemistry and electrostatics. Generally droplets of size < 1mm sitting on a dielectric surface and surrounded by an ambient medium like air (commonly used) or oil are studied for EWOD experiments. Both gravity and surface tension affect the behavior of the water droplets and the effects of gravity diminish as the droplet of study becomes smaller and smaller. The Bond number Bo determines the strength of gravity.

$Bo = \sqrt{(g\Delta\rho R^2/\sigma_{lv})}$

As already seen in the previous chapter the free energy of a droplet (unelectrified) is determined by surface tension and can be given by the following Young equation.

$\mathbf{\cos\theta_Y = (\gamma_{sv} - \gamma_{sl}) / \gamma_{lv}}$

θ_Y = Young's contact angle

γ_{sv} = Surface Tension (energy per unit surface) of the solid-vapor interface

$\boldsymbol{\gamma_{sl}}$ = Surface Tension of the solid-liquid interface

$\boldsymbol{\gamma_{lv}}$ = Surface Tension of the liquid-vapor interface

Lippmann-Young Equation

When an electric voltage is applied an electrostatic term is added to the system making it readjust itself for a minimization of energy of the total system. This readjustment results in the effective change in the contact angle of the droplet and the final equation of electrowetting can be given by using Lippmann's electrostatic expression.

$\mathbf{\cos\theta_V = \cos\theta_Y + \frac{1}{2}(\varepsilon_0\varepsilon_r V^2)/(d^* \gamma_{lv})}$ **……..(3.1)**

V - Applied Voltage

d - Thickness of the dielectric medium

θ_V - Electrowetting Contact Angle

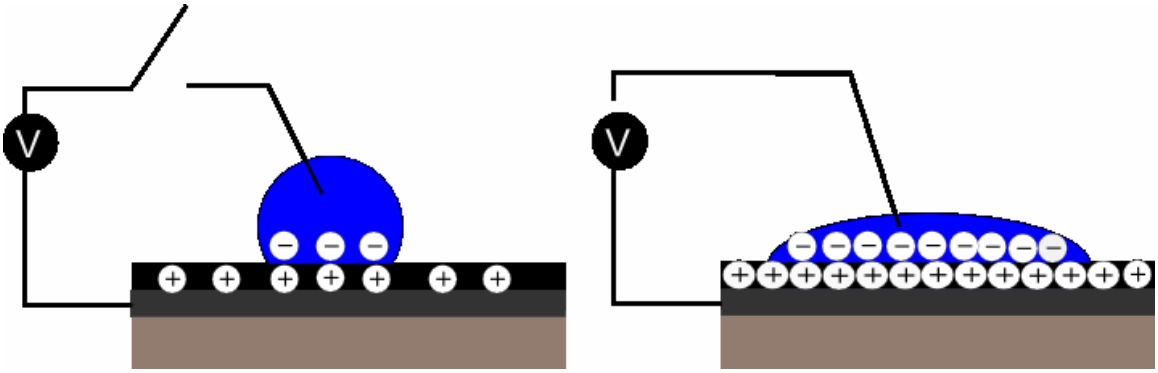

Fig. 3.3 – Voltage induced charge redistribution of a droplet interface

The additional term represents the electrostatic energy balance on the liquid droplet resulting from the charging of the flat plate capacitor that is created by the liquid, dielectric, solid boundary. While interfacial energies, permittivities and insulator thickness are constants that depend on the material and medium properties, the voltage is the parameter that plays a dynamic role in decreasing the contact angle and causing wetting. The important thing to be noted is that the above equation that correlates the contact angle and the applied voltage does not hold goods only for a certain range of voltages. Above that an effect called as the contact angle saturation is experienced where the contact angle does not decrease in agreement with the Lippmann-Young equation.

Contact Angle Saturation

Electrowetting can cause a considerable reduction in the contact angle from the initial contact angle (when no voltage is applied) thereby making it suitable for application in several droplet manipulation devices. Gaining maximum control over the contact angle works very favorably for most of these applications. A control over the contact angle implies the ability to achieve complete wetting and de-wetting by the alteration of a given range of voltages. But however it has always been observed that this has not been possible even at very high driving voltages.

The issue of contact angle saturation has been addressed extensively by several works which attribute the saturation to i) The actual contact line is shifted due to the injection of charge carriers inside the insulator causing alterations in free energies ii) Non – linear effects caused by the divergence of electric fields in the contact line iii) Imbalance of repelling charges at the contact line beyond a threshold voltage. The listed ones have been commonly used to describe the phenomena of contact angle saturation.

Evaluations – EWOD in rough and planar surfaces

Electrowetting phenomena are evaluated based on the energy minimization approach. Evaluations are done based on the surface roughness and the presence or absence of an ambient oil medium around the droplet. The nature of electrowetting is described by primarily applying the Lippmann-Young equation to each of the cases.

Energy Minimization approach

Two broad conceptual approaches to explaining the EWOD theory have been put forward. The first being the energy minimization approach and second being the electrohydrodynamic

approach. The energy minimization is more simplistic and accounts for the equilibrium shape of the droplet in terms of the free energy of minimization. The electrohydrodynamic approach takes into consideration the electromechanical forces exerted by field on the liquid, and hence rigorously considers fluid properties like viscosity etc.

The energy approach is used in this chapter and is centered on the tendency of the droplet to minimize its energy, which acts as the driving force behind the observed contact angle change.

Review on Contact Angle Equations

As seen in detail in the previous chapter superhydrophobic surfaces exhibit extremely large contact angles (generally greater than 150˚). The large contact angles are primarily contributed by enhanced surface roughness followed by chemical hydrophobic treatment of the surface.

When a solid surface is physically structured a roughness factor is introduced into the system

r - Actual Surface Area/Projected (Horizontal) Surface Area

For r>1 the de-wetting properties are enhanced due to an increased contact angle. Rough wetting regimes can be Wenzel or Cassie-Baxter.

The force balance Young-Laplace equation gives the contact angle of a planar hydrophobic surface.

$$\cos\theta_Y = (\gamma_{sv} - \gamma_{sl}) / \gamma_{lv} \quad \text{(3.2)}$$

The apparent contact angle of a Wenzel surface is given below.

$$\cos\theta w = r^* \cos\theta_Y \quad \text{(3.3)}$$

r – roughness ratio

The apparent contact angle of a Cassie surface is given by

$$\cos\theta_W = \varphi_{s^*} \cos\theta_Y + \varphi_{l^*} \cos 180^o \quad \text{(3.4)}$$

φ_s – Fraction of the wetted solid-liquid contact area

φ_l – Fraction of the liquid- air interface

The bottom of a Cassie droplet is heterogeneous since it interfaces with both enclosed air pockets and solid structure. Thus the Cassie apparent contact angle is expressed as fractional contact angle contributions from the solid liquid interface and the liquid air interface. The Cassie surface reduces to a Wenzel surface if the $\varphi_l = 0$.

A Planar Surface – Ambient Air Medium

A planar hydrophobic surface is smooth and homogeneous and suits the definition of Young's contact angle *(Fig. 3.4)*. A conductive surface coated with a smooth dielectric can be a suitable device. The dielectric is chosen to be a hydrophobic material ($\cos\theta_Y > 90^\circ$) to achieve the ultimate goal of wetting. The dielectric prevents leakage of the across the device and capacitively charges up resulting in an EDL. Though the EDL behaves like a uniform parallel plate capacitor across the bulk of the solution there is an enhanced charging at the three phase contact regions resulting in an electric field induced force. *Eqn. 3.1* gives the balance of forces in voltage-subjected system.

Energy Balance

$$\cos\theta_Y = (\gamma_{sv} - \gamma_{sl}) / \gamma_{lv}$$

Electrowetting

$$\cos\theta_V = \cos\theta_Y + \tfrac{1}{2} (\varepsilon_0\varepsilon_r V^2)/(d^* \gamma_{lv})$$

We can see from the EWOD equation that increasing the dielectric constant and decreasing its thickness can obtain a larger contact angle change for a given voltage. The inverse proportionality to the liquid air interfacial tension shows that electrowetting change favors a low surface energy liquid.

A Planar Surface – Ambient Oil Medium

An ambient oil medium consists of a setup similar to the section described in the previous section but with air replaced by oil. Oil is a non-polar substance and has a lower surface tension than water.

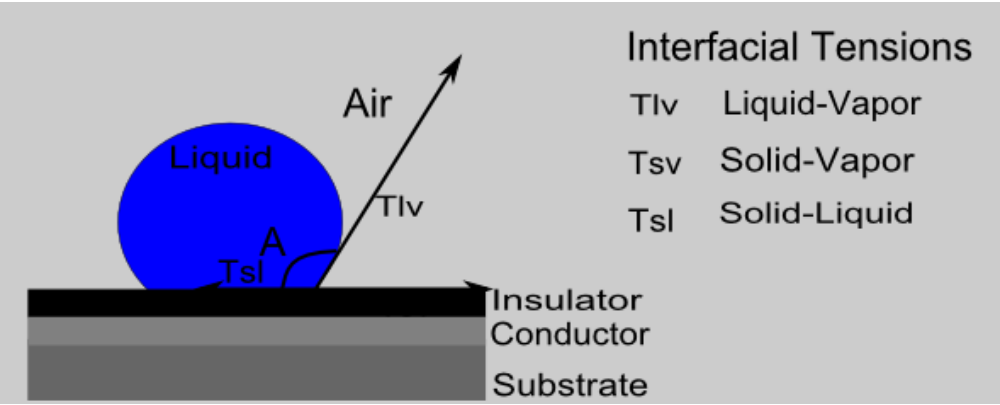

Fig. 3.4 – Droplet on a Plane Hydrophobic surface with air as an ambient medium

Hence it easily seeps in between the liquid solid region forming a thin film of oil that separates the liquid polar drop and the solid. The outer region of the drop interfaces with oil instead of air. The water droplet being less dense tends to sink into the bottom of the oil medium.
Drawing the contact line and analyzing the two-phase interface gives the following force balance equation (*Fig. 3.5*).

$\mathbf{\cos\theta_Y = (\gamma_{oo} - \gamma_{lo}) / \gamma_{lo}} = -1$
o - oil interface

The resulting electrowetting equation becomes
$\mathbf{\cos\theta_V = \cos\theta_Y (\sim\cos 180) + \frac{1}{2} (\varepsilon_0\varepsilon_r V^2)/(d^* \gamma_{lo})}$

We can make two inferences from the above equations

- The initial contact angle can be boosted to a high superhydrophobic value by introducing oil as an interfacial medium. We can see that the contact angles of droplets tend to shoot up to the maximum 180˚ when interfaced with oil. A high starting contact angle provides a large tuning range, which is a very useful feature for most applications. Also a reduced hysteresis (due to the oil) is very favorable for the reversibility or de-wetting to take place.

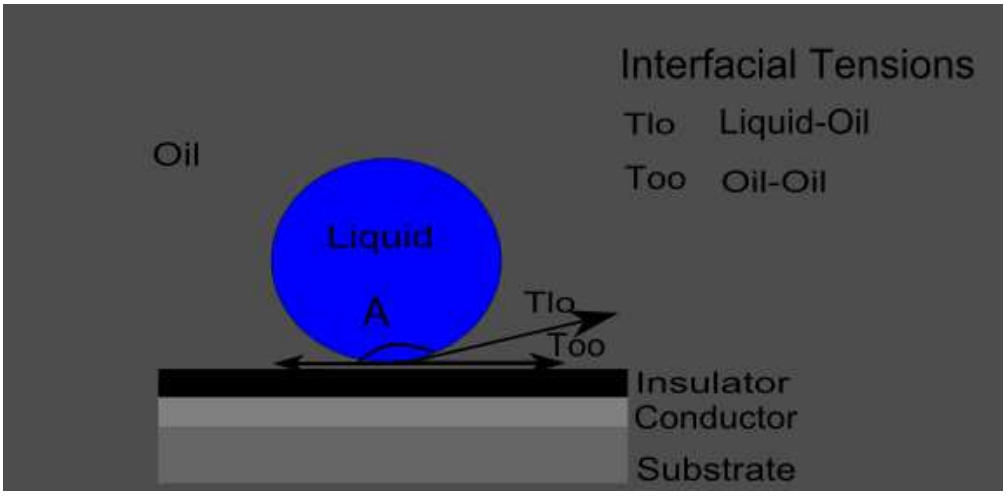

Fig. 3.5 – Droplet on a Plane Hydrophobic surface with oil as an ambient medium

- The electrostatic energy contribution is increased with the γ_{lo} factor in the denominator. This is due to the fact that oil has a much lower interfacial energy with water when compare to air. Thus a small voltage can help in attaining a considerable contact angle change.

A Wenzel Surface – Ambient Air Medium

A droplet in the Wenzel regime completely penetrates into the surface features thereby holding a homogeneous interface at the droplet bottom *(Fig. 3.6)*. The only difference of is that Wenzel droplet sits with an initial contact angle given by the roughness factor. A Wenzel surface for electrowetting can be made to have a fairly large initial contact angle when compared to a smooth hydrophobic surface but a still suffers hysteresis. Hysteresis makes reversibility more difficult to attain.

A Wenzel Surface – Ambient Oil Medium

A droplet in the Wenzel regime surrounded by an oil medium still penetrates into the surface features and the oil forms a layer between the liquid and the solid medium *(Fig. 3.7)*. So the contact angle of water is further raised to the ideal value by the presence of the oil. The presence of oil lowers hysteresis affects and reduces the effective voltage requirements for the wetting process as explained in the planar – oil system. The layer of oil below the liquid acts as a smooth interface below and the droplet acts like it were on a perfectly smooth surface free of micro-cracks and irregularities. This smoothness greatly helps in the reduction of contact angle hysteresis

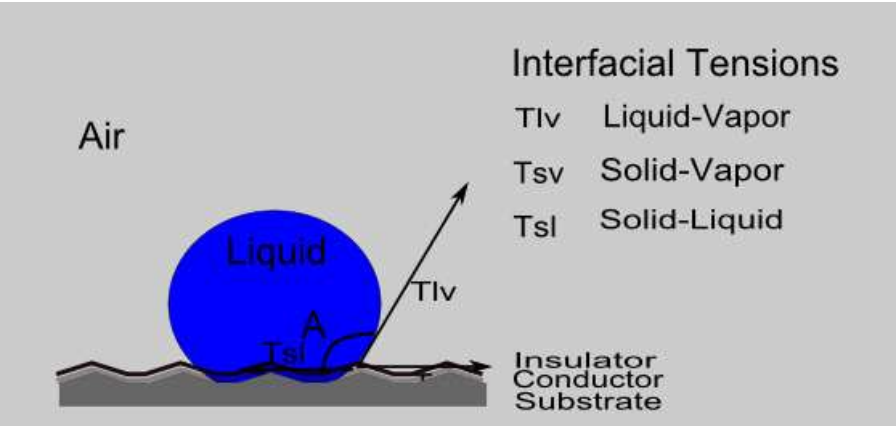

Fig. 3.6 – Droplet on a Wenzel surface with air as an ambient medium

A Cassie-Baxter Surface – Ambient Air Medium

A Cassie droplet attains energy minimization by resting on the tips of the surface structures *(Fig. 3.8)*. It has a very high contact angle (>150˚) and shows very low contact angle hysteresis due to the intermittent air surfaces beneath the surface of the droplet. Such surfaces show a high initial contact angle and slightly altered electrowetting behavior. The alteration is mainly caused due to the fractional wetting of the projected surface.

The wetting process for a Cassie drop involves the following phenomenon as described in an extensive work on droplet microfluidics [3.15].

- Horizontal movement (contact angle change) of the three-phase contact line.
- Vertical movement (horizontal contact line shift). The vertical movement is characterized by slow penetration of the liquid down into the features.

Analyzing *Fig. 3.8* we can write the following force balance equation at the contact line of the Cassie drop. The force balance equation reduces to

$$\cos\theta = (\gamma_{sl} - \gamma_{sv}) / \gamma_{lv}$$

An effective solid liquid interfacial energy $\gamma_{esl,}$ is contributed by the solid and the air contacts at the bottom of the drop. It has been shown that electric field induced force is only observed in the fractional area f which has been wetted by the surface [3.15].

Thus Lippmann's equation reduces to

$$\cos\theta_V = \cos\theta_Y + \tfrac{1}{2} f(\varepsilon_0\varepsilon_r V^2)/(d^* \gamma_{lv}) \quad \text{……..(3.5)}$$

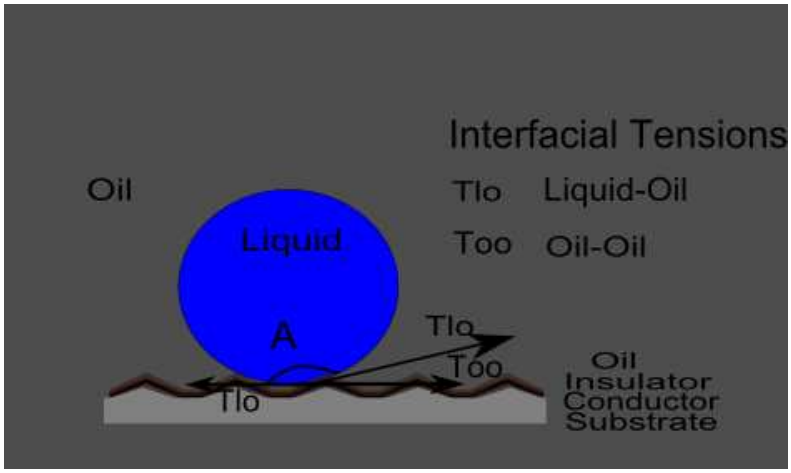

Fig. 3.7 – Droplet on a Wenzel surface with oil as an ambient medium

The fractional wetting causes fractional electrostatic energy thereby reducing the overall contact angle change for given voltage. Thus we can conclude that for a droplet sitting in the Cassie-Baxter regime the electrowetting effect is much weaker.

The voltage induced vertical motion of the baseline occurs resulting in a change in the instantaneous Young's angle of the drop *(Fig. 3.9)*. This gradual change in the Young's angle is due to a downward capillary force which changes the shape of the meniscus of the liquid between the features and makes it move down and wet the surface. The onset of complete wetting is characterized by a threshold voltage at which the convex to concave meniscus transition occurs. It has been shown that the electrowetting contact angle can be expressed in terms of the capacitance change due to the vertical distance moved by the droplet after the application of voltage [3.15].

$\cos\theta_V = \cos\theta_Y + ½ (\varepsilon_0\varepsilon_r V^2 * A)/(d^2 * \gamma_{lv} * L)$ ……..……..(3.6)

A – Effective perimeter in a unit capillary membrane of the structure

L – Effective perimeter of the unit capillary membrane

The ratio A/L varies for different structure profiles.

During the onset of action of the vertical electrostatic pressure

$\cos\theta_V = 0$

$½ (\varepsilon_0\varepsilon_r V^{2)}/d^2 = - \gamma_{lv} * \cos\theta_Y * L / A$…….(3.7)

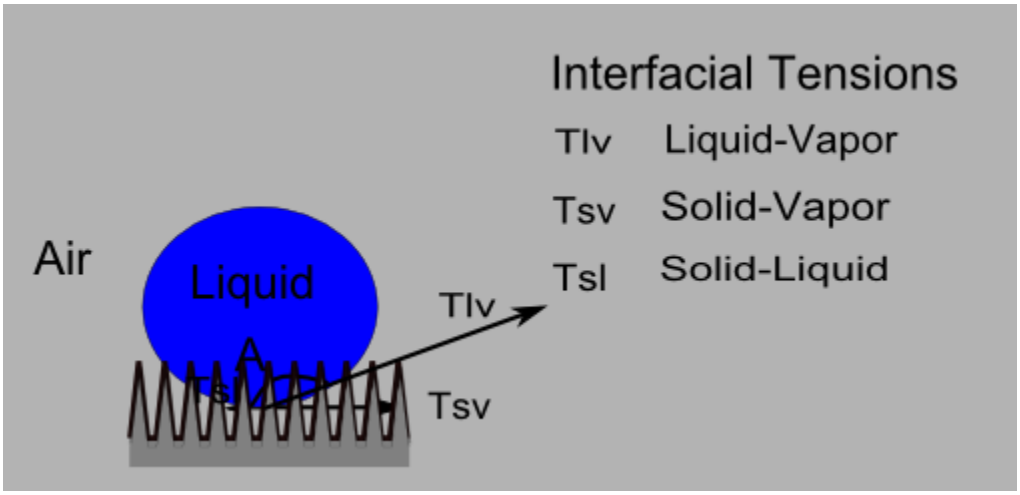

Fig. 3.8 – Droplet on a Cassie surface with air as an ambient medium

The expression on the right side of the equation is the pressure that will drive the liquid inside the surface of the capillary that is nothing but the vertical electrostatic pressure on the liquid. It has also been shown that the apparent contact angle change induced by the vertical motion changes the electrowetting contact angle only slightly more than *Eqn. 3.5*. The vertical movement induced change depends on the feature geometry. Hence the voltage induced contact angle change can be approximated to *Eqn. 3.5* for a Cassie Baxter surface.

The nature of reversibility for this model has been estimated to be poor due to the reduced energy state attained by the water drop that made to penetrate into the (normally unreachable) feature depth. Hence it is not energy-favorable for the droplet to pop back up on the withdrawal of the voltage and it remains in the wetted state.

A Cassie-Baxter Surface – Ambient Oil Medium

A drop on a Cassie surface surrounded completely by oil allows the oil to easily penetrate into the surface features *(Fig. 3.10)*. This results in the air pockets seen in a regular Cassie setup being replaced with oil.

On the application of the voltage a phenomena very similar to that obtained in the previous section is observed. The downward capillary force tries to push the oil out of regions between the structures. The force and contact angle change is similar but with the interfacial energies replaced with that of the oil. Oil, as previously discussed helps lowering the electrowetting voltage.

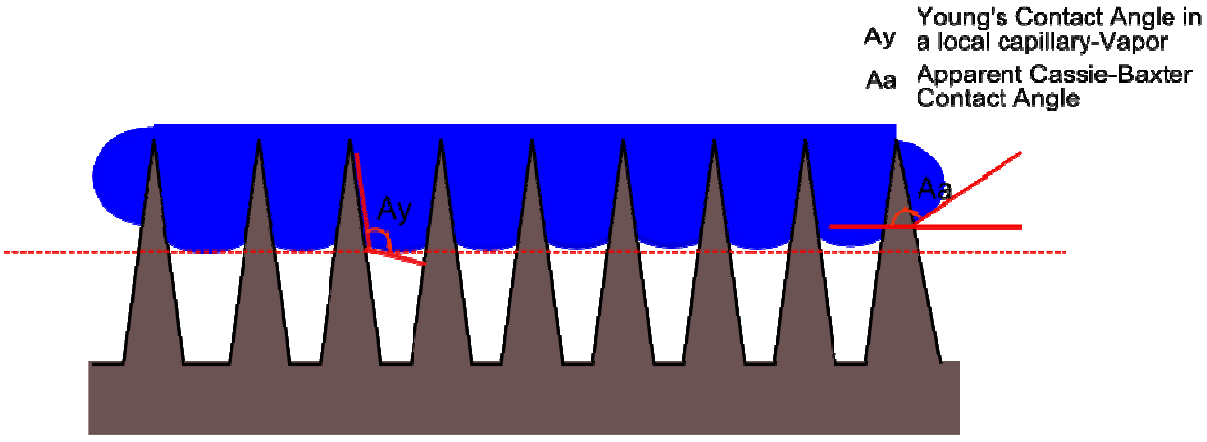

Fig. 3.9 – Contact Angles of a Cassie surface

The force balance equation at the baseline is given below.

$\mathbf{\cos\theta = (\gamma_{oo} - \gamma_{ol}) / \gamma_{lo}}$

The oil-modified Cassie electrowetting equations are

$\mathbf{\cos\theta_V = \cos\theta_Y + \frac{1}{2} f(\varepsilon_0\varepsilon_r V^2)/(d^* \gamma_{lo})}$ **……..……..(3.8)**

Apart from the increased wetting a more useful interpretation can be made from this model. The introduction of oil also helps in reducing hysteresis as already seen in the previous cases. Oil also helps in achieving reversibility, which is not possible in the presence of air pockets. This is because of the competitive tendency of the oil to push back the liquid to its initial Cassie position on the withdrawal of the voltage. Hence this setup is more advantageous when droplet actuation experiments are done on a superhydrophobic surface.

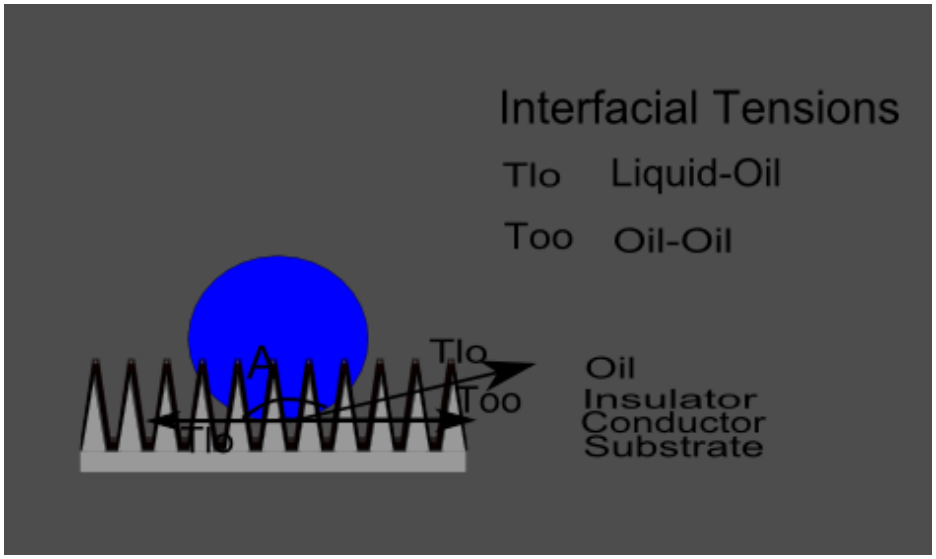

Fig. 3.10 – Droplet on a Cassie surface with oil as an ambient medium

Preparation of the EWOD Device

A good selection and application of the insulating layer on the rough substrates can drastically improve the electrowetting behavior. This section discusses the layering process that is employed to fabricate the electrowetting device.

Material Considerations

Several reports have been published on optimized electrowetting devices [3.5, 3.8, 3.9]. Most results show that electrowetting depends weakly on the liquid properties but more critically on the properties and type of insulator used. The fine-tuning of the dielectric layer is done mainly to favor electrowetting at much lower voltages, but at the same time the long-term stability of the device is also of utmost importance. As already discussed a high initial contact angle is useful for getting a larger range of wettability control as well as reduced hysteresis. Thus the dielectric materials are insulating hydrophobic layers. The thickness of the dielectric must also be thin and still must not suffer breakdown for a suitable range of voltages. The conductive layer used can be a thin coating of any chemically inert metal like gold. Conductive electrodes spaces periodically created by lithography techniques have also been used. For surfaces with features it is very important to have conformal and thin coating on the entire projected surface area. Vertically projecting spikes with a high aspect ratio are very challenging surfaces to uniformly deposit material. A technique like vapor deposition and evaporation are more anisotropic in nature and the material manages to arrive inside the surface features (which are spaced in the order of a few hundred nanometers) and deposit a smooth layer. The coating thickness is also a very critical parameter. Apart from increasing voltage requirements a thick coating of dielectric layer can also cover up the required surface features that might affect the initial contact angle of the surface during the electrowetting experiment. Suitable bonding materials can be additionally coated to improve the adhesion of the conductive and insulating layers.

Substrate Layer

The goal of the electrowetting experiments is to study behavior of droplets in the Wenzel and Cassie and smooth hydrophobic regime under the influence of an electric field. The Wenzel and Cassie fabrication is similar to that discussed in the previous chapters. Glass drawing followed by the differential etching results in features with a low and high aspect ratio. The etched wafers were cleaned ultrasonically in water and isopropanol. The results of the etching were two

features with a high and low aspect ratio. The samples were etched to an aspect ratio that made them fall under the Cassie and Wenzel regimes of surfaces. The lattice constant of these features is 7μm. The etching parameters for the substrates under electrowetting study are listed in *Table 3.1*. SEM images of the etched features are shown in *Fig. 3.11*. The low aspect ratio was classified as a Wenzel surface since it is expected to show an initial contact angle in air similar to that shown by a surface in a Wenzel wetting regime. The high aspect ratio was classified as a Cassie surface since it is expected to show an initial contact angle in air similar to that shown by a surface in a Cassie wetting regime. This aspect ratio based classification was done mainly based on the study in the third chapter of this thesis on superhydrophobic behavior.

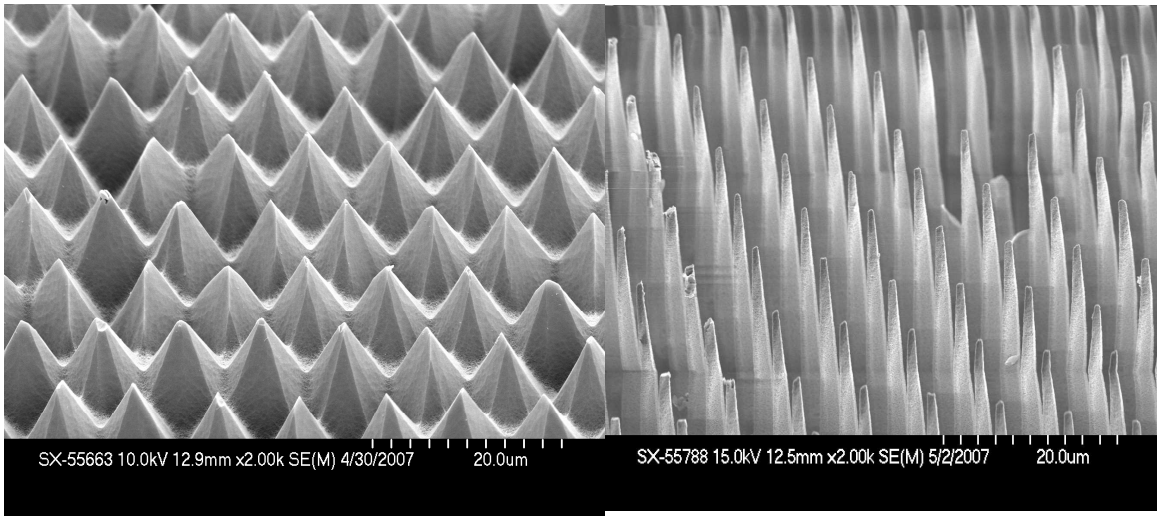

Fig. 3.11 – SEM images of Etched Wafers having a Low (left) and High Aspect Ratio (right)

Table 3.1 – Substrate Etching parameters for the EWOD experiments

Slice	Etching Solution	Etch Time	Aspect Ratio
412 – High Aspect Ratio	1.5ml BHF + 3.5ml DHF	60 min	.35
416 – Low Aspect Ratio	10:1 DHF	30 min	5
Glass Slide	-	-	-

Conductive Coating by E-Beam Evaporation

A conformal coating of gold on the low and high aspect ratio surfaces was chosen to serve as the conductive layer. The samples were placed in an e-beam evaporation chamber and were coated with gold. An e-beam evaporator uses a magnetic field to direct a high-energy electron beam (3 – 20keV) on target materials to melt and vaporize them. The eventual condensation of the vaporized metal results in its deposition on the substrate.

The system mainly consists of an electron beam evaporation gun, the material to be coated and the target metals placed in crucibles. The setup is enclosed in a vacuum chamber, which allows the molecules to evaporate freely. E-beam evaporation is a physical vapor deposition process not involving any chemical reactions. Film thickness control quartz based monitor is available which helps in knowing the amount of metal that has been deposited. Generally a high deposition rate of 50 – 500 nm/min can be obtained. The etched glass wafers were treated with 100 nm of chrome followed by 500 nm of gold in order to safely ensure a conformal coating on the surface features. The chrome coating was primarily done to improve it's the adhesion of glass with the gold. Evaporation seemed to be a better choice than sputtering for the deposition of gold due to its anisotropic nature. Anisotropic deposition seemed more favorable for the gold atoms to get into the high aspect ratio features.

Dielectric Coating by CVD Technique

The dielectric layer chosen for the electrowetting device is Parylene-C. Parylene-C is a member of the linear crystalline parylene polymeric series and contains a chlorine atom substituted for one of the aromatic hydrogen. A vapor deposition process deposits Parylene films where they polymerize upon adsorption onto the substrate. A 1-μm thick Parylene-C coating was deposited on the gold-coated samples in a SCS (Specialty Coating Systems) labcoater.

Heating of the Parylene-C powder loaded in the system causes the vaporization of the dimer followed by pyrolysis. At room temperature and pressure of .1 Torr the vaporized monomer deposits and polymerizes on the substrates. Parylene is inert and can give a very conformal pinhole free coating on topographically patterned surfaces. Parylene has high dielectric breakdown strength *(Table 3.2)* and hence a 1 μm thick coating was used. Parylene-C and Teflon are the commonly used dielectric coatings. Parylene has slightly better dielectric properties than Teflon and has been reported not to breakdown at 250V applied. However though Parylene is a good insulator it is much less hydrophobic than Teflon and other popular hydrophobic coatings.

The Parylene deposition *(Fig. 3.12)* process first involves the vaporization of the solid dimer at approximately 150°C. Next, the quantitative cleavage of the dimer at the two methylene-methylene bonds takes place at a temperature of around 670°C to yield the stable monomeric para-xylylene.

Finally, the monomer enters the room temperature deposition chamber where it simultaneously adsorbs and polymerizes on the substrate. The system is also equipped with the pumps for maintaining the pressure and a protective cold trap that condenses and collects Parylene byproducts thereby preventing contamination. The deposition rate is fairly fast (about .2 mils/hour).

Table 3.2 – Parylene-C properties

Property	Value
Dielectric Strength – 1 mil films	5600 dc volts/ mil
Surface Resistivity (23˚ C)	10^{14} ohms
Dielectric Constant	3.15 (60 Hz) 3.10 (1 KHz) 2.95 (1 MHz)

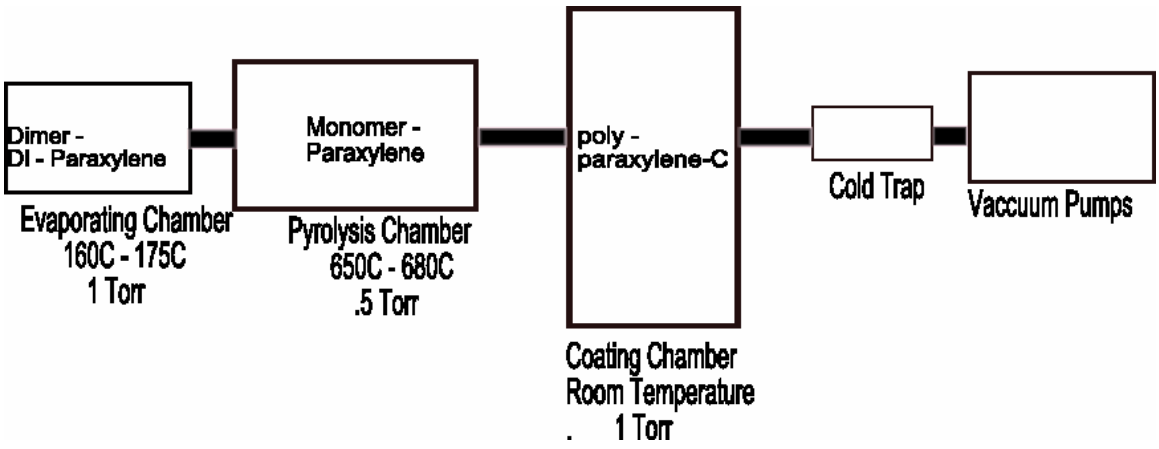

Fig. 3.12 – Schematic of the Parylene deposition process

A silane primer is used which is a commercially available parylene deposition-bonding agent marketed under the product name A174 Silane. It interfacially bonds the gold with the deposited Parylene C by creating chemical linkages.

The chemical agent in A174 Silane is gamma-methacryloxypropyltrimethoxysilane. Equal proportions of deionized water and isopropyl alcohol are mixed and the A-174 silane is added such that the proportion of the water-IPA and the silane is 200:1. After stirring continuously the solution is left to sit at room temperature for about two hours. The wafers are soaked in the solution followed by cleaning in IPA. The wafers are dried completely. The treated wafers must be used within a few hours of coating for the Parylene deposition.

Fig. 3.13 shows the SEM images of the Parylene coated wafers. The wafers were coated with gold in the sputter coater for viewing in the SEM.

Silicone oil

The oil used in the electrowetting tests was silicone oil. Silicone oil is an optically clear fluid with a refractive index of 1.397. It shows excellent water-repellency and low surface tension. The surface tension of silicone oil with a viscosity of 5cSt is 19.7mN/m. It also has very low toxicity and can be used freely as the ambient environment of liquids and devices. In our experiments silicone oil with a 2cSt viscosity was used.

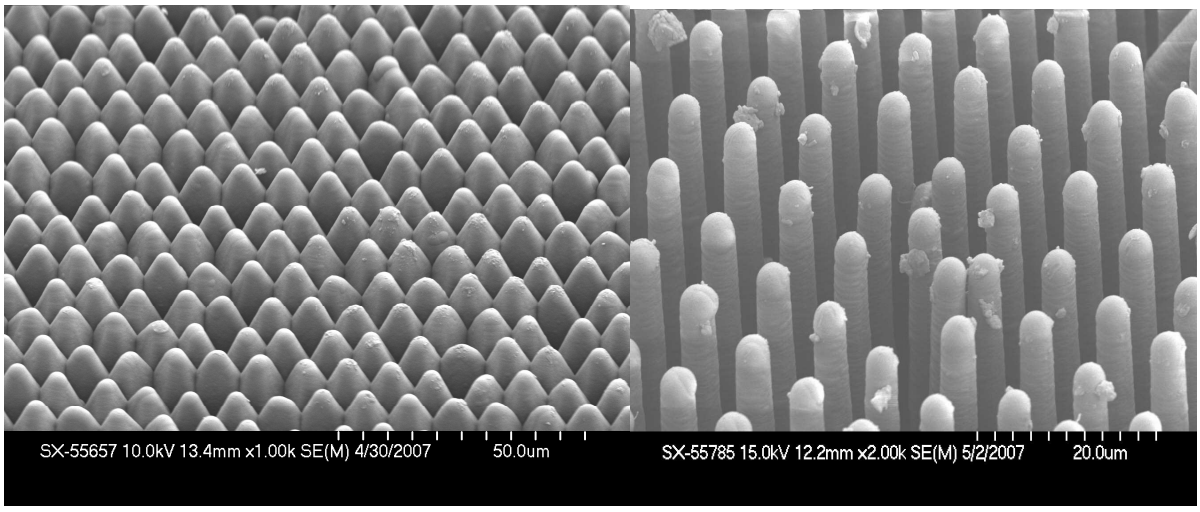

Fig. 3.13 – SEM images of the low (left) and high aspect ratio (right) wafers after coating with Gold and Parylene

EWOD – Experiments and Observations

The actual electrowetting property of the surfaces is observed in the experiment. The experimental process is described in this section. This is followed by detailed analysis of the wetting produced in each of the surfaces. The results are characterized using the images of the drop taken during the electowetting process and the current voltage curves.

Experimental Setup

The experimental setting for performing the electrowetting consist of the following equipments i) A Melsobel color camera ii) An adjustable focus, lighting lens iii) A Keithley source meter iv) A precision 3-axis Signatone micropositioner iv) Tungsten Probe Tips with holders iv) Video Tool box software interfaced with the camera v) Labtracer software interfaced with the Source meter as shown in *Fig. 3.14*.

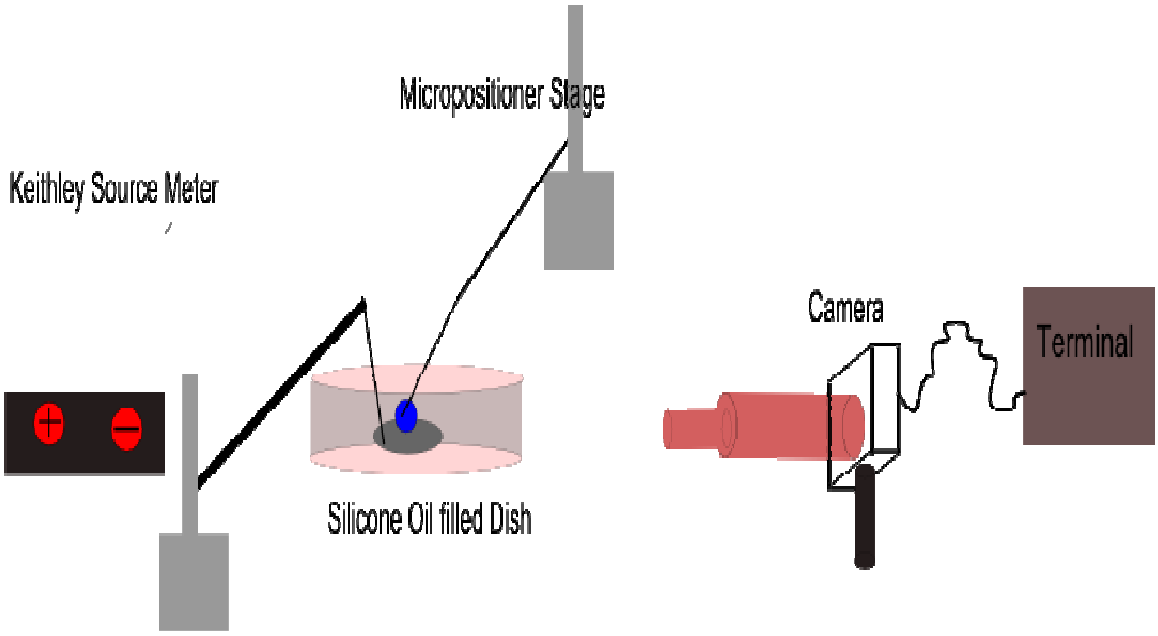

Fig. 3.14 – Schematic of the EWOD Experimental Setup

The droplet's volume is about 10 μl and is dispensed on a suitable defect free region of the wafer. The power supply is given though a general purpose source meter that can measure up to 200V, 1A and 20W power output. The source meter is GPIB interfaced with a Lab View driven tool. The tool can control the DC voltage profile. The voltage supply directly connects to tungsten probe tips are mounted on the probe holders using a screw mount system. The probe holders are pliable and are bent to an angle to reach and make easy contact of the probe tip with the wafer inside the dish. The micropositioner are equipped with probing features and have the linear X-Y-Z motion control with 100 threads per inch drives. A pivot head is attached has additional control knobs for quick and coarse positioning of the probe tip. The micropositioner has a magnetic base for steady positioning. The wafer to be analyzed is placed in a transparent Petri dish. The wafer is placed against the wall of the dish for better image quality. The positive probe tip is immersed in the droplet and the negative terminal is contacted with the conducting gold layer.
Since the gold layer is buried under the Parylene more attention was needed to get good contact of the conductor. Imaging was done using a high speed, high resolution equipped with a C– type lens mount. A USB interface was used to drive the camera through a Video toolbox in the computer terminal. It was positioned to line up horizontally to focus on the drop. The camera was placed on a mount for adjustable vertical height. A variable focus, variable lighting lens was attached to the camera. The entire setup was placed in an optical table.

The droplets that were tested using air as the ambient medium were first tested for its hydrophobic/superhydrophobic behavior. This was done by manual observation of the drop profile and also by the geometric estimation of the contact angle from the image of the drop before the application of any voltage. For oil based tests the contamination free silicone oil was filled in the Petri dish till a level where both the wafer and the droplet can be completely immersed. The wetting was characterized by running the device through a series of tests of varying voltage ranges and sweep times. The linear step voltages were introduced with a 25 ms delay and were useful for comparing the contact angles at various voltages. The voltage – current curve of the test was also taken. Several tests were done to make a better estimation of critical values such as the threshold, breakdown and saturation voltages. For a given wafer and a given set of conditions multiple sets of measurements were taken with the drop positioned in different locations in the surface and with the probes contacting different points of gold in the wafer. This is primarily to eliminate the effect of the errors introduced due to poor electrical contact and

defective regions under the drop. Both step and sweep voltages were applied to the droplet and snapshots of the droplet were taken in fixed intervals of time. For estimation of the contact angles at voltages, images of the wetting drop were taken at every 5V increment. The contact angle was estimated geometrically from the drop image.

Observations – Contact Angle Changes

Planar Surface – Air Medium

The planar surface used was a piece of microscope glass slide coated with gold and Parylene-C. The slide was placed in the Petri dish and a droplet of water was dispensed on a clean region of the slide. A DC potential was applied between the positive probe, which was immersed in the droplet, and the negative one that was placed firmly against the surface of the slide.

The parylene seems to have barely managed to make the surface hydrophobic. The actuation voltage was estimated from the contact angles. The device seemed to have a fairly low threshold voltage of 5 volts. The wetting response seemed to be very gradual in the air environment (*Fig. 3.15b – 3.15e*). A useful wetting range of voltages was between 5V – 60V where gradual contact angle decrease of about 35˚ was observed (*Table 3.3*). For a different test set the breakdown seemed to happen at around 100V. Breakdown was characterized by a current leakage causing bubbling in the droplet. The removal of the applied voltage in every case resulted in partial irreversibility of the wetting. The VI curve is shown in *Fig. 3.15a*.

Table 3.3 – Wetting voltages of a planar device in air medium

Voltage (V)	Contact Angle
0	92˚
20	78˚
40	69˚
60	55˚
80	55˚
100	55˚
0	65˚

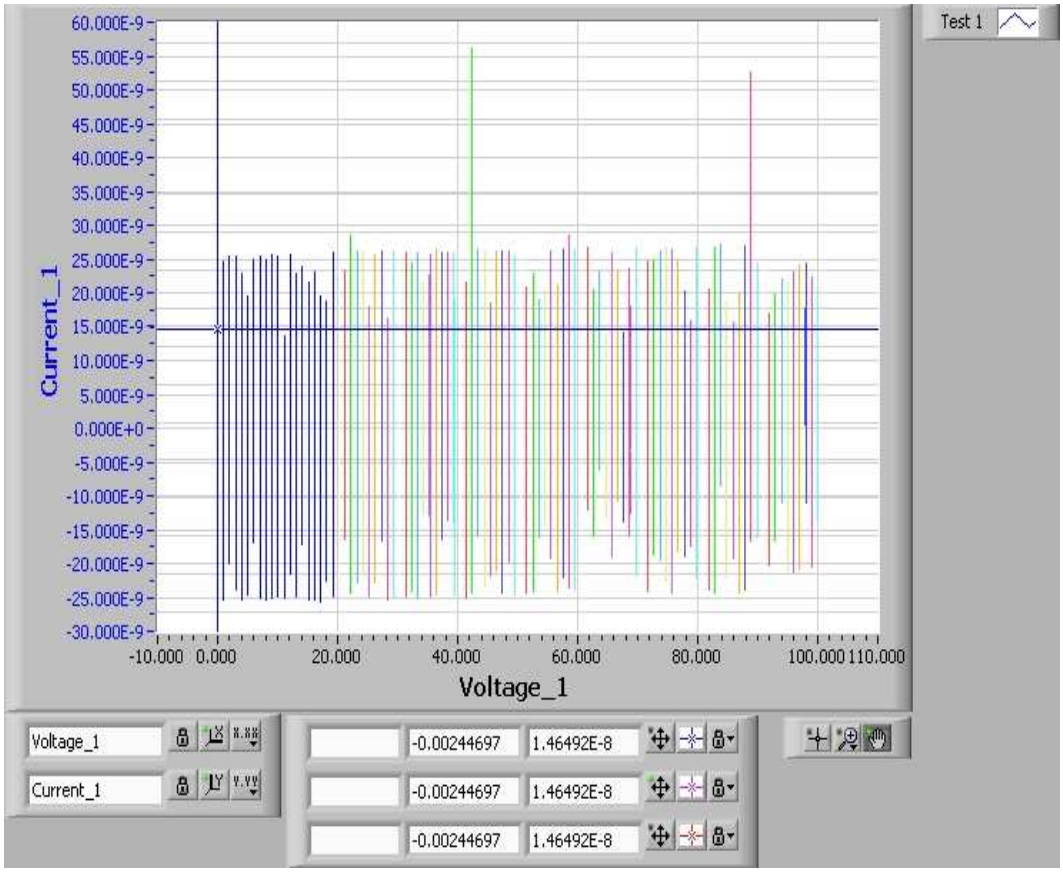

Fig. 3.15a – VI curve of the EW test on planar surface in air

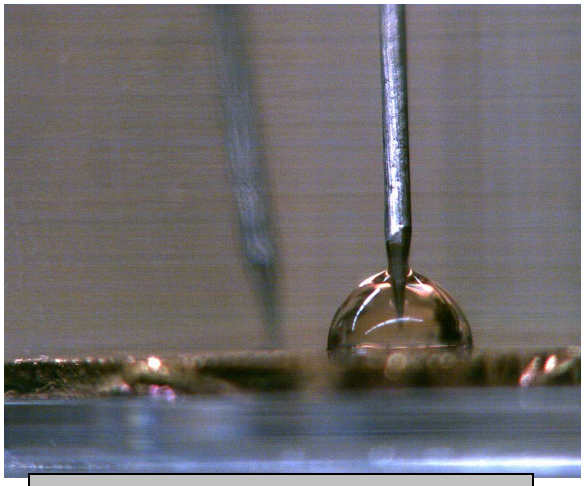

Surface seems just hydrophobic
Contact Angle - 92˚

Fig. 3.15b – Planar Surface –Air Medium (0V)

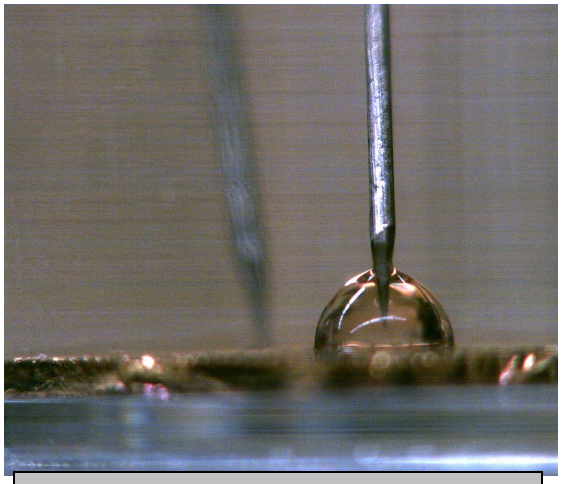

Drop actuated to contact angle
change at ~ 5V. Contact Angle - 90˚

Fig. 3.15c – Planar Surface –Air Medium (5V)

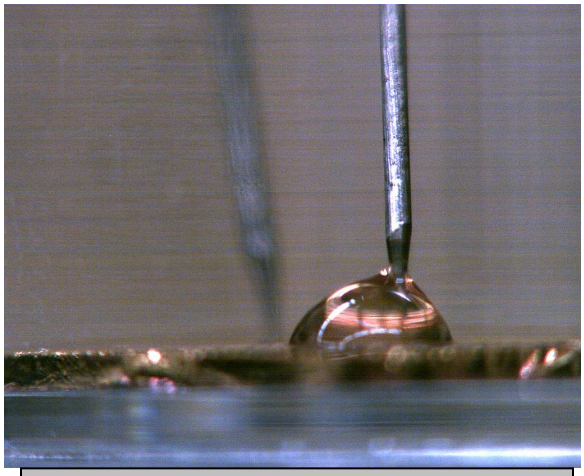

Maximum wetting witnessed at ~ 60V.
Contact Angle is 55˚
Contact angle saturates after 60V

Fig. 3.15d – Planar Surface –Air Medium (60V)

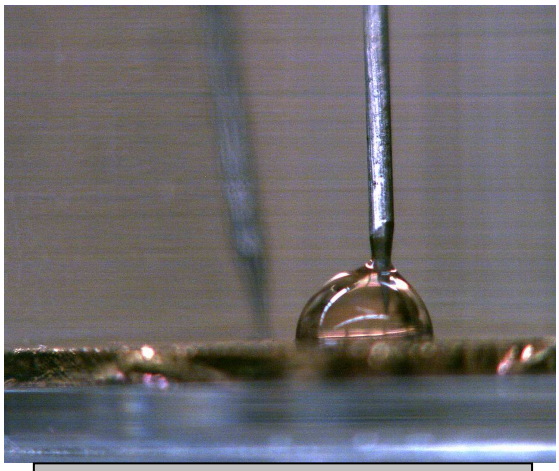

Voltage returned back to 0.
Incomplete reversal of wetting
Contact Angle is 65˚

Fig. 3.15e – Planar Surface –Air Medium (Returned to 0V)

Planar Surface – Oil Medium

The planar surface used with oil is similar to the one used in the previous section. The wafer was immersed in the oil filled dish. A droplet was allowed to completely sink down and settle on a smooth section of the glass slide and the potential was applied. As expected with the oil the droplet had a high contact angle. The threshold voltage was 5V. The wetting response was gradual in the oil environment (*Fig. 3.16b – 3.16e*). A smoothly changing contact angle was observed as the voltage was varied from 0 – 80V *(Table 3.4)*.

Table 3.4 – Wetting voltages of a planar device in oil medium

Voltage (V)	Contact Angle
0	132˚
20	115˚
40	100˚
60	88˚
80	80˚
0	120˚

The removal of the applied voltage in every case resulted in good reversibility back to a contact angle of 120˚. The VI curve is shown in *Fig. 3.16a*.

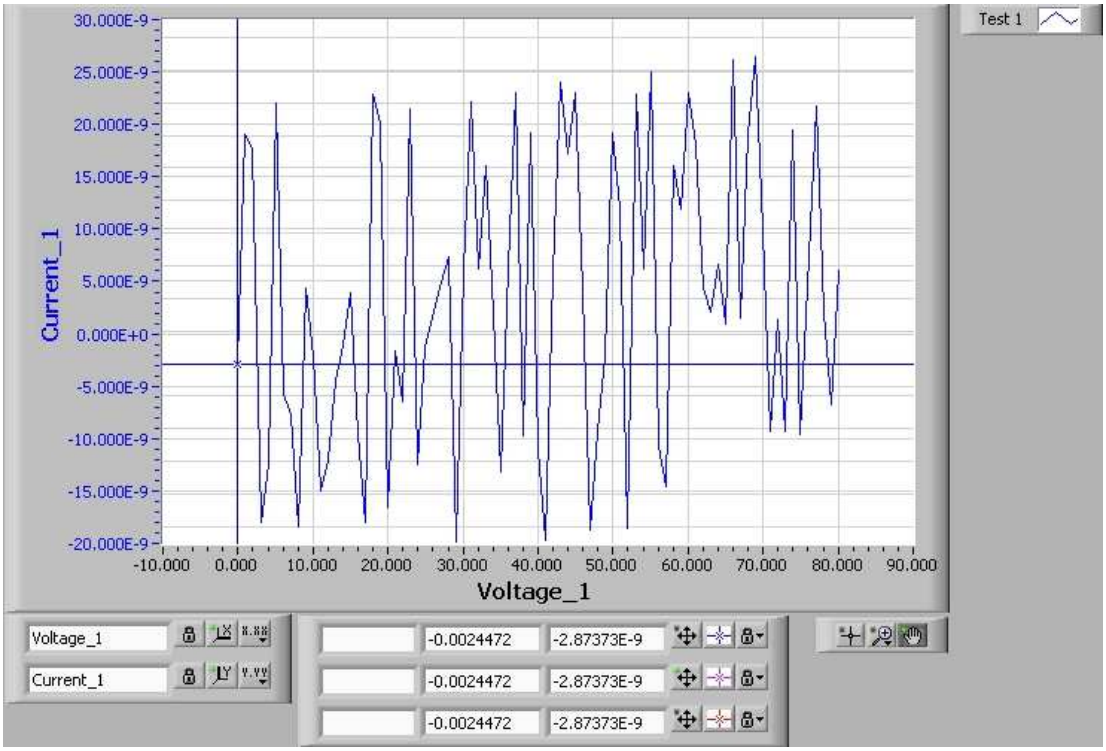

Fig. 3.16a – VI curve of the EW test on planar surface with oil

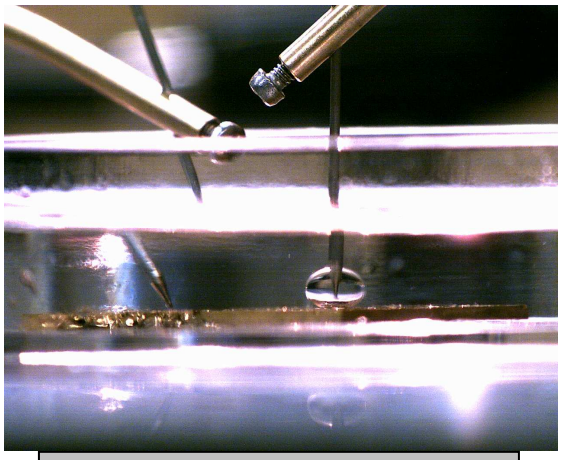

Large contact angle due to the oil
Contact Angle - 132˚

Fig. 3.16b – Planar Surface –Oil Medium (0V)

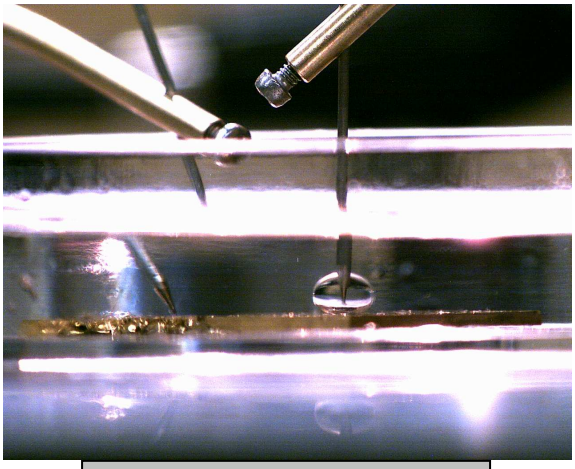

Actuation Voltage ~ 5V
Contact Angle - 128˚

Fig. 3.16c – Planar Surface –Oil Medium (5V)

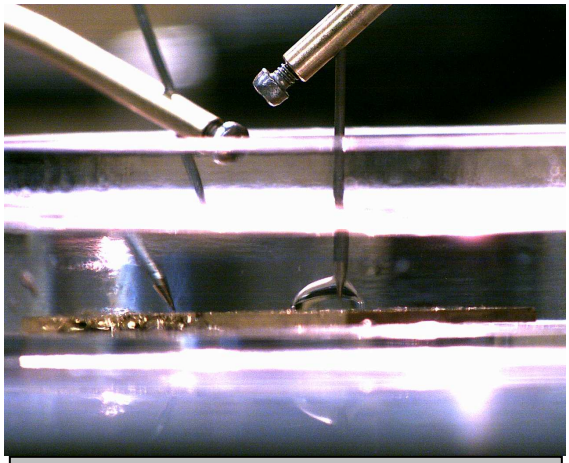

Maximum observed wetting ~ 85 V
Contact angle – 80˚
Breakdown observed at higher voltages

Fig. 3.16d – Planar Surface –Oil Medium (85V)

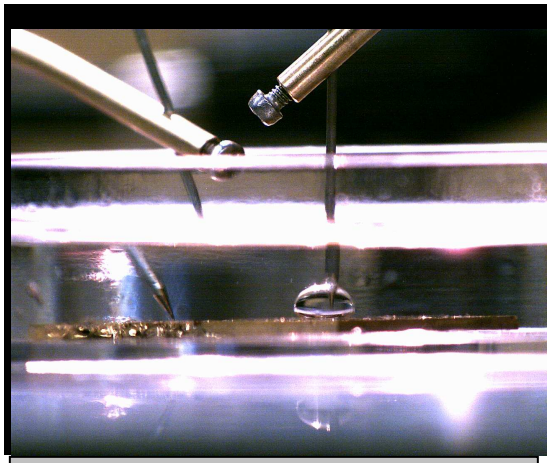

Voltage returned back to 0V.
Almost complete reversal of wetting observed , Contact Angle is 120˚

Fig. 3.16e – Planar Surface –Oil Medium (Returned to 0V)

A Breakdown condition

For another set of experiments with the planar surface and the oil an early breakdown occurred at around 85V as seen in *Fig. 3.16f* and *Fig. 3.16g.*

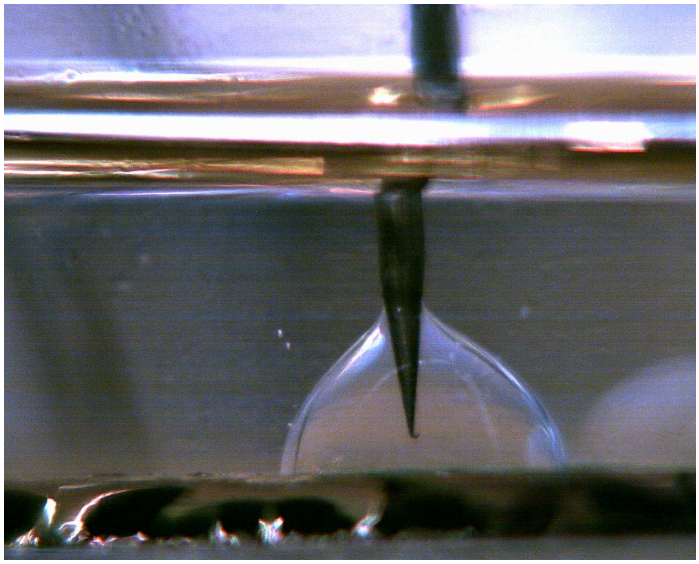

Fig. 3.16f – Wetting at breakdown condition

The breakdown induced complete wetting but reversal was still present. Due to the early breakdown the complete useful wettable range could not be tapped in the device.

Wenzel Surface – Air Medium

The wafer with a Wenzel surface is placed in the Petri dish and firm contact of the negative probe is made against the smooth edge of the wafer to avoid interference with the featured regions. The droplet is placed on the rough section of the wafer (other than the edge) and a potential is applied.

The Wenzel surface shows an initial contact angle of 114˚ due to the combination of surface roughness and the poorer hydrophobic properties of Parylene-C. The threshold voltage was at about 5V when a small noticeable change was observed. The contact angle change was more gradual *(Fig. 3.17b – Fig. 3.17e)*. Breakdown for a different test set was observed as low as 75V. The breakdown induced complete wetting but no reversibility was observed. An effective change of 25˚ was observed with a voltage range of 90V followed by a brief range of saturation *(Table 3.5)*. The VI curve is shown in *Fig. 3.17a*.

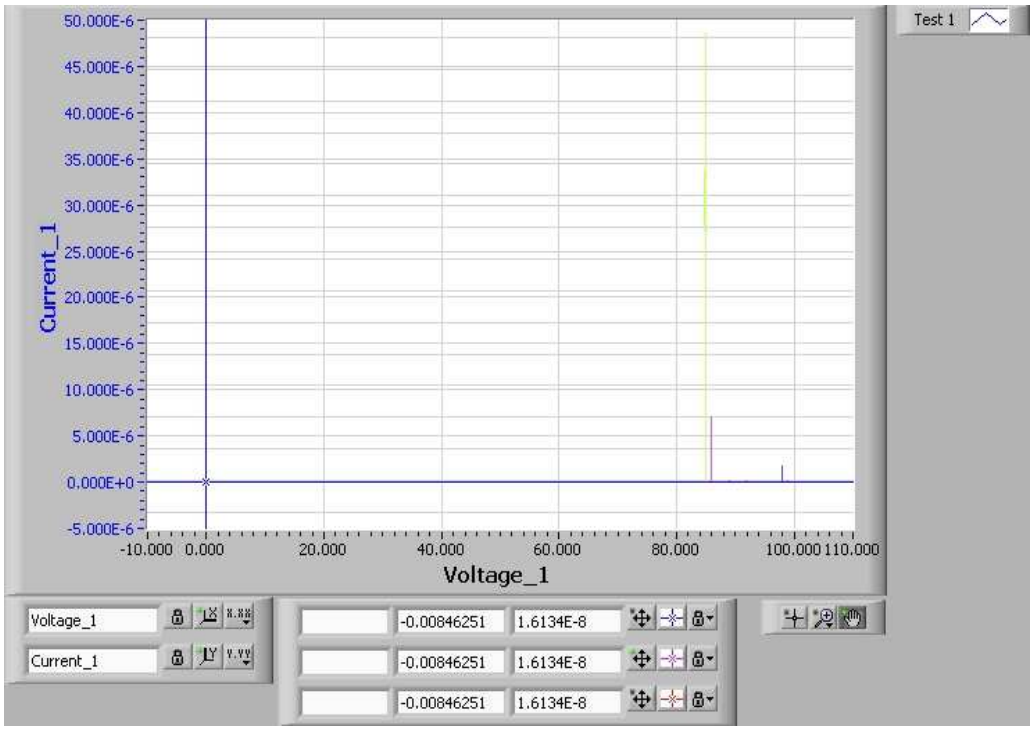

Fig. 3.16g – Leakage across the dielectric

Table 3.5 – Wetting voltages of a Wenzel device in air medium

Voltage (V)	Contact Angle
0	114°
20	108°
40	101°
60	96°
80	90°
100	87°
0	87°

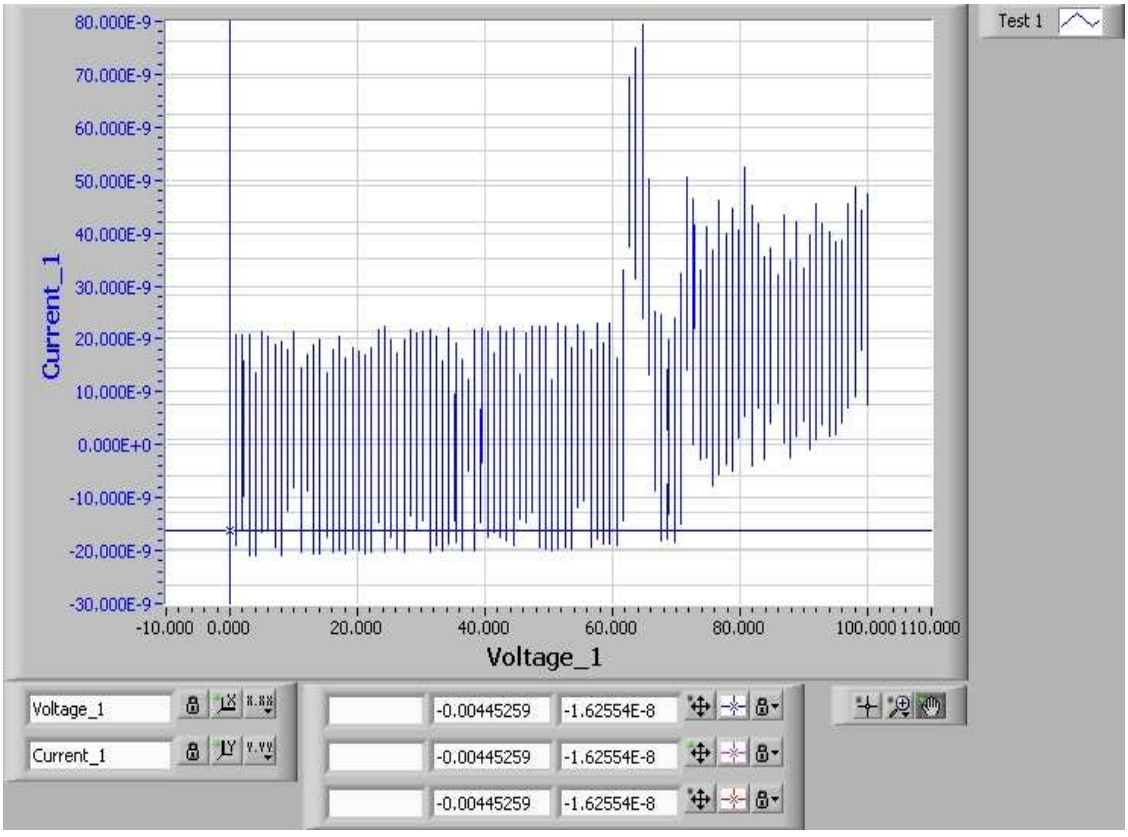

Fig. 3.17a – VI curve of the EW test on Wenzel surface surrounded with air

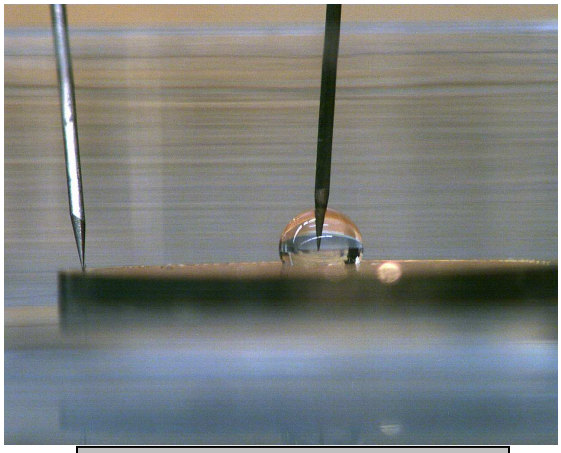

Contact angle - 114˚

Fig. 3.17b – Wenzel Surface –Air Medium (0V)

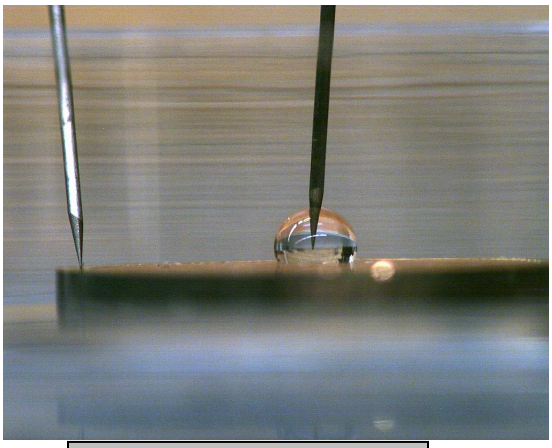

Threshold Voltage ~ 5V
Contact Angle - 113˚

Fig. 3.17c – Wenzel Surface –Air Medium (5V)

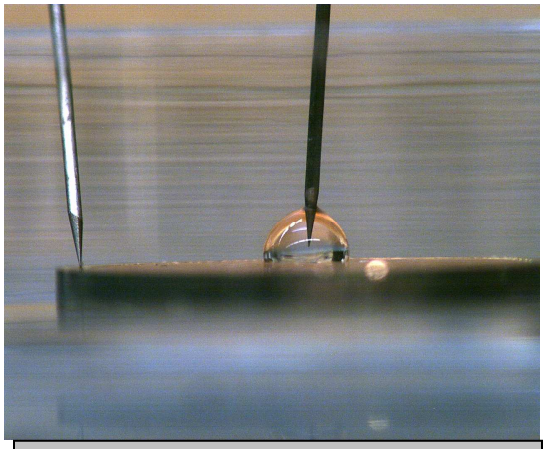

Maximum wetting observed - 90 V
Followed by saturation / breakdown
Contact Angle – 87˚

Fig. 3.17d – Wenzel Surface –Air Medium 90V

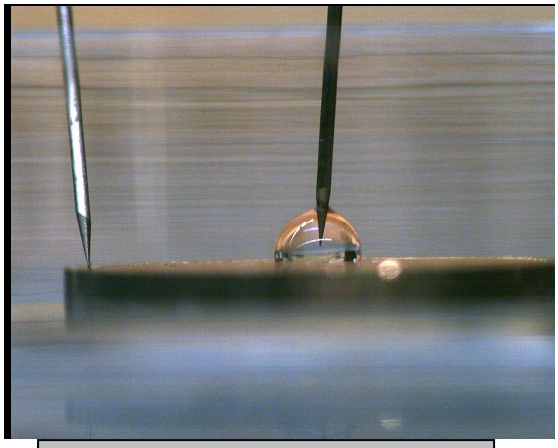

Voltage is returned back to 0V.
No reversal of the contact angle was observed

Fig. 3.17e – Wenzel Surface –Air Medium (Returned to 0V)

Wenzel Surface – Oil Medium

The Wenzel surface shows a very high contact angle of 155˚ *(Table 3.6)*. This threshold voltage was at about 5V. Breakdown for a different test set was observed at 115V. An effective change of 90˚ was observed with a voltage range of 120V *(Fig. 3.18b – 3.18e)*. The removal of the applied voltage in every case resulted in excellent reversibility back to a contact angle of 155˚. The VI curve is shown in *Fig. 3.18a.*

.

Table 3.6 – Wetting voltages of a Wenzel device in oil medium

Voltage (V)	Contact Angle
0	155˚
20	134˚
40	115˚
60	100˚
80	77˚
100	70˚
120	66˚
0	155˚

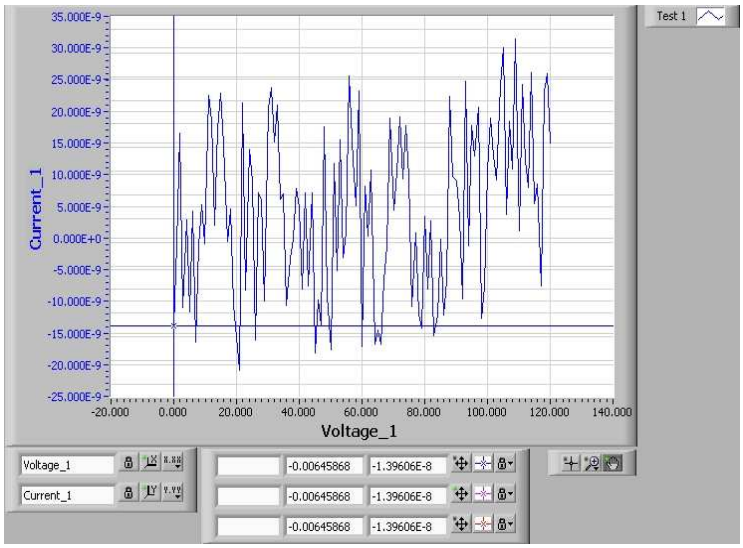

Fig. 3.18a – VI curve of the EW test on Wenzel surface surrounded with oil

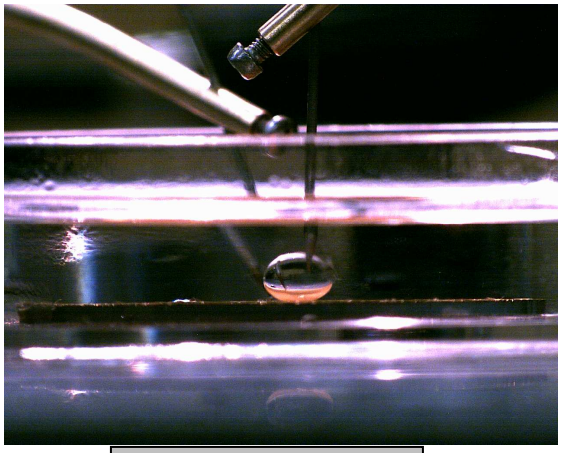

Contact angle - 160˚

Fig. 3.18b – Wenzel Surface –Oil Medium (0V)

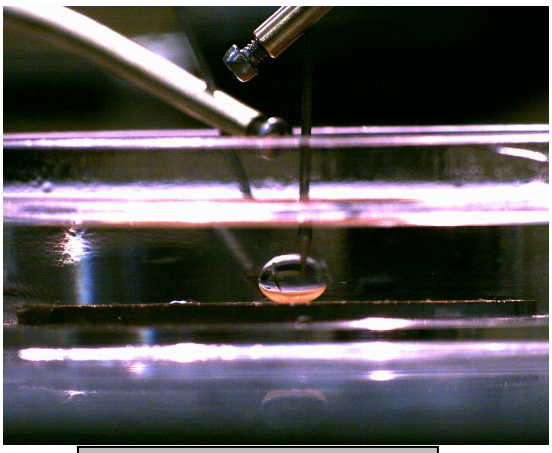

Threshold Voltage ~ 5V
Contact Angle - 153˚

Fig. 3.18c – Wenzel Surface –Oil Medium (5V)

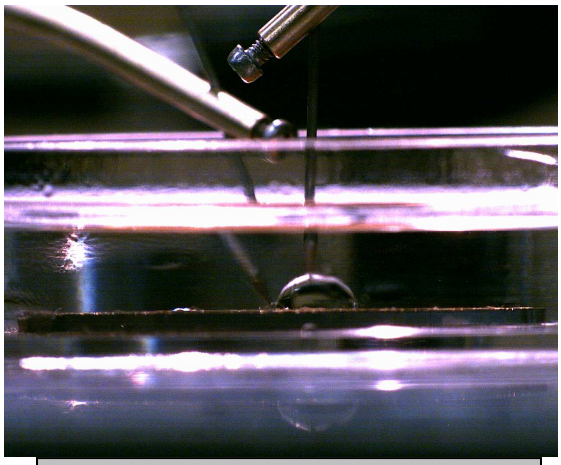

Maximum wetting was observed at 120 V
Contact Angle – 66˚

Fig. 3.18d – Wenzel Surface –Oil Medium (120V)

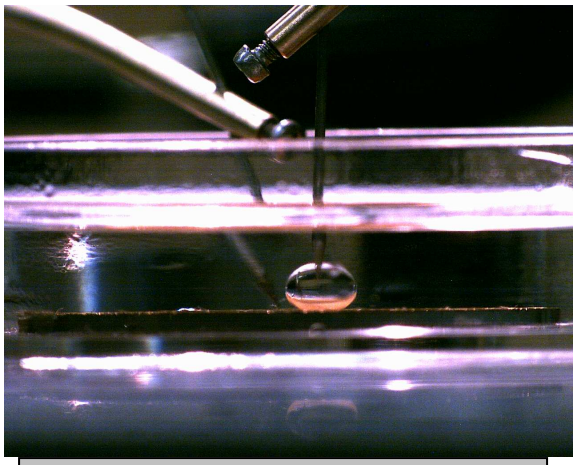

Voltage is returned back to 0V. Almost complete reversal of the contact angle was observed

Fig. 3.18e – Wenzel Surface –Oil Medium (0V-Returned)

Cassie Surface – Oil Medium

The Cassie surface shows a very high contact angle of 150˚. This threshold voltage was at about 25V till a noticeable wetting change was observed. No significant change in contact angle was observed with the Cassie surface *(Fig. 3.19b – 3.19e)*. The VI curve is shown in *Fig. 3.19a*. The contact angle mostly occurred during the vertical motion of the drop towards the surface. No signs of breakdown were observed even at voltages as high as 150V *(Table 3.7)*.

Table 3.7 – Wetting voltages of a Cassie device in oil medium

Voltage (V)	Contact Angle
0	180˚
20	180˚
40	170˚
60	151˚
80	135˚
100	130˚
120	128˚
140	134˚
0	138˚

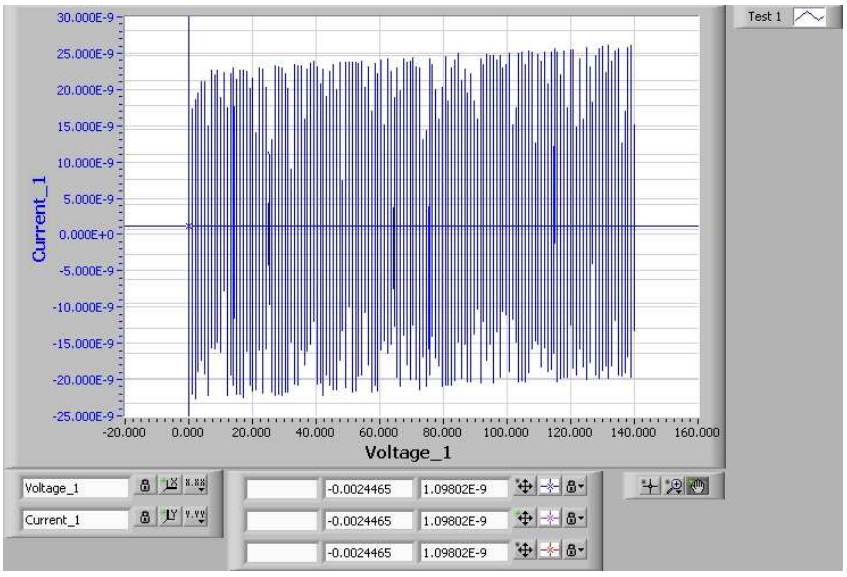

Fig. 3.19a – VI curve of the EW test on Cassie surface surrounded with oil

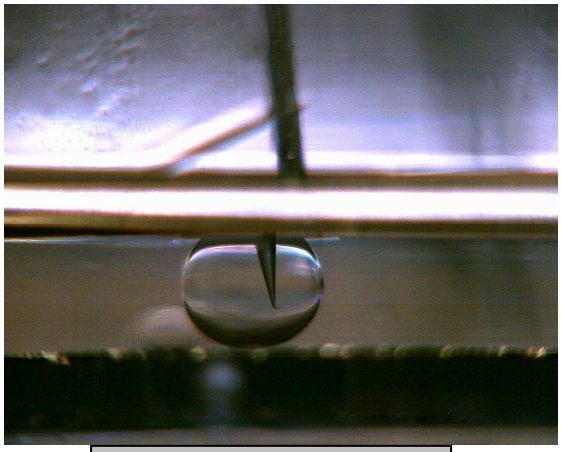

Contact angle - 180˚

Fig. 3.19b – Cassie Surface –Oil Medium (0V)

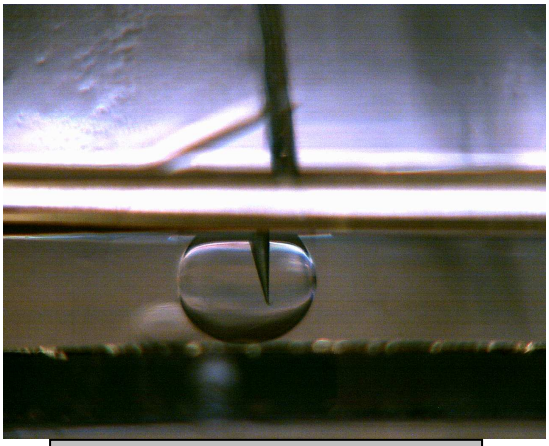

Threshold Voltage ~ 30V
Contact Angle - 170˚

Fig. 3.21c – Cassie Surface –Oil Medium (30V)

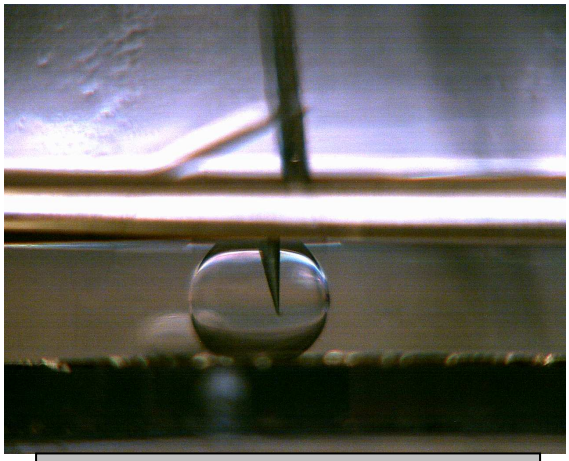

Maximum wetting was observed at 100 V
Contact Angle – 90˚

Fig. 3.19d – Cassie Surface –Oil Medium 140V

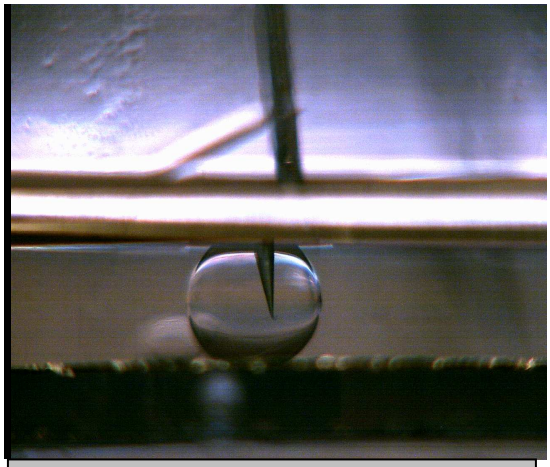

Voltage is returned back to 0V. Irreversibility of the contact angle was observed.

Fig. 3.19e – Cassie Surface –Oil Medium (0V Returned)

Modeling of EWOD on Nanocone surfaces

The electrowetting behavior of a water droplet on an ideally planar surface surrounded by air can be expressed in terms of the conventional Lippman-Young equation. But when a structured (topographically patterned) surface or an ambient oil medium (instead of air) is introduced the voltage induced contact angle change is greatly affected. In this section we study theoretically the effect of the nanocone structure and the role of oil in the electrowetting behavior and compare it to the experimentally obtained values.

Interfacial energies and areas of structured surfaces

A surface can exhibit structure in terms of random roughness or a periodic structure as seen in the nanocones. Here we consider the structured surface to be a well-ordered nanocone glass array. A drop of water sitting on such a surface in air could fall in either one of the well-known wetting regimes. A drop on a surface in the Wenzel regime is expected to completely wet the solid interface and one on a Cassie regime is expected to partially wet the solid interface. In our experimental analysis we use two surfaces, which can be classified as Wenzel or Cassie purely by known surface geometry (which is the aspect ratio).

For a structured surface the macroscopic interfacial tension can be expressed as

$\gamma_{macro} = \int_{micro} \gamma_{micro}(X).dA / A_{projected}$

$A_{projected} = A_{macro}$

The voltage-induced electrowetting changes the microscopic γ over some regions resulting in an effective change in the macroscopic γ and hence the effective contact angle change.

For a drop of liquid resting on such a surface surrounded by air the modified solid-liquid interfacial tension can be given as

$\gamma_{macro*} A_{macro} = A_{non\text{-}wetted} * \gamma_{la} + A_{wetted} * \gamma_{ls}$ ……..……...3.9

The effect of voltage on such an interface is that it modifies the solid liquid surface tension given by the Lippman's equation

$\gamma ls(V) = \gamma ls - ½ * C * V^2$ ……...…3.10

Incorporating *Eqn. 3.10* in *Eqn. 3.9* we get

$\gamma_{slm} = (A_{non\text{-}wetted}/A_{macro}) * \gamma_{la} + (A_{wetted}/A_{macro}) * (\gamma_{ls} - ½ * C * V^2)$ ……..……...….3.11

γ_{slm} = Electrowetting modified solid-liquid interfacial tension of a structured surface

$\gamma ls(V)$ = Solid-liquid interfacial tension at voltage V

γls = Solid-liquid interfacial tension

γ_{la} = Surface tension of the liquid

A_{wetted} = Area of the wetted region of the structure

$A_{non\text{-}wetted}$ = Area of the liquid-air interface around the wetted cone

A_{macro} = Area of the projected hexagonal lattice

C = Capacitance formed by the electrical double layer

V = Voltage applied

Interfacial areas of a nanocone

Water on a given structured hydrophobic surface partially or fully wets it based on its geometry. But the presence of an ambient medium like oil might enable a drop on a Wenzel surface to have a very high contact angle as if it were in a Cassie-like state. Such a Cassie-like state is also observed on a plane medium surrounded by oil. On a plane surface the transition from a Cassie-like to a Wenzel state is more straightforward due to the absence of structure and the voltage of transition can be directly measured from the contact angle. But in order to understand the nature of transition of a Cassie-like drop to a Wenzel drop on a Wenzel surface in oil we have to take into consideration the role of roughness in the wetting process. Hence we assume that a drop on a Wenzel surface in oil will tend to exhibit partial wetting.

The following parameters define the geometry of a partially wetted nanocone

a = face to face length of the hexagonal base

h = height of the nanocone

r = base radius of the nanocone

h_w = wetted nanocone height

r_w = wetted nanocone radius

φ = Nanocone apex half-angle

Using these parameters the areas listed in *Eqn. 3.11* can be calculated.

1- Projected Area

The projected area is the base hexagonal area of the nanocone and is the same for the Cassie and the Wenzel surface.

$A_{macro} = A_m = (\sqrt{3}*a^2)/2$

$a = 7*10^{-6}$ m

$A_m = 42.4352*10^{-12}$ m^2

2 - Wetted Areas

The wetted area of a partially wetted nanocone (as shown in *Fig. 3.20*) is the surface area of the fractionally wetted cone. Since we have assumed a fractionally wetted behavior for a Wenzel surface in the presence of oil the expressions for the fractionally wetted areas for a Wenzel surface is also derived. A Wenzel surface in air is expected to show a fully wetted state and the wetted area is calculated from the known height of the nanocone.

i) Partially wetted Cassie surface

$A_{wetted} = A_{partially\_wetted\_cassie} = A_{p\_w\_c} = (\pi * h_w^2 * \sin\varphi) / \cos^2\varphi$

$\varphi = 13^o$, $\sin\varphi = .22495$, $\cos\varphi = .97437$, $\tan\varphi = .23086$

$\mathbf{A_{p\_w\_c} = .743499 * h_w^2\ m^2}$

ii) Partially wetted Wenzel surface

$A_{wetted} = A_{partially\_wetted\_wenzel} = A_{p\_w\_w} = (\pi * h_w^2 * \sin\varphi) / \cos^2\varphi$

$\varphi = 32^o$, $\sin\varphi = .529919$, $\cos\varphi = .84804$, $\tan\varphi = .624869$

$\mathbf{A_{p\_w\_w} = 2.3105 * h_w^2\ m^2}$

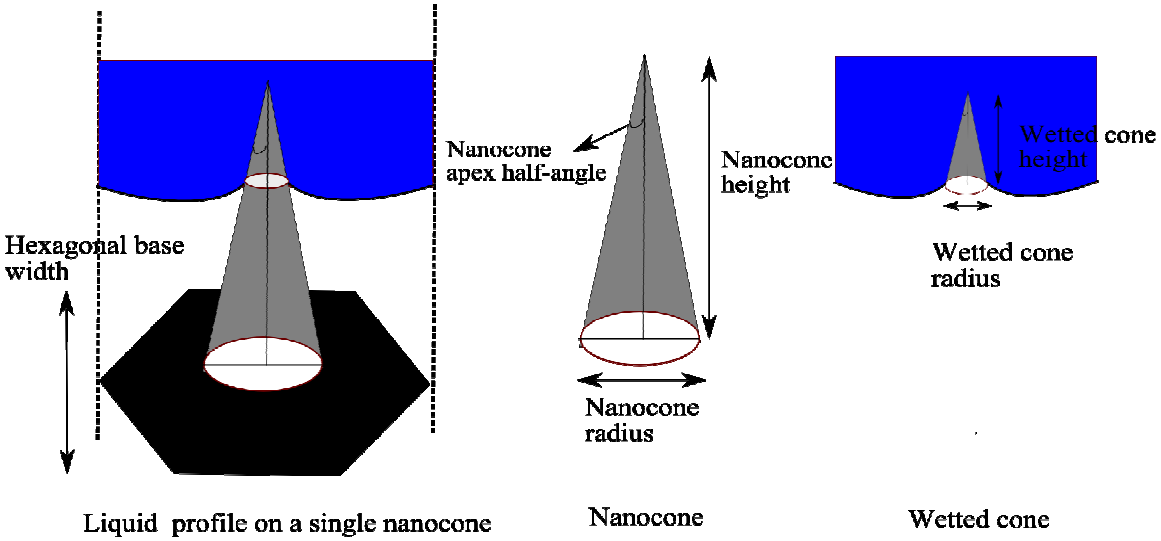

Fig. 3.20 – Fractional wetting profile of a single nanocone

iii) Fully wetted Wenzel surface

$A_{wetted} = A_{fully\_wetted\_wenzel} = A_{f\_w\_w} = \pi*h^2*(\sin\varphi-\sin^2\varphi)/\cos^2\varphi + (\sqrt{3}*a^2/2)$

$h = 7.07*10^{-6}$ m, $\varphi = 32^o$, $\sin\varphi = .529919$, $\cos\varphi = .84804$, $a = 7*10^{-6}$ m

$\mathbf{A_{f\_w\_w} = 96.8*10^{-12}\ m^2}$

3 - Non-wetted areas

The non-wetted region of a given nanocone refers to the area where the liquid interfaces with the ambient medium like air (or oil) instead of the solid. This is calculated by subtracting the area of the hexagonal base from the projected circular area of the wetted nanocone. For any partially wetted surface such an area exists due to the presence of air (or oil) pockets in each of the nanocones. But for a fully wetted nanocone the nonwetted area is absent since the liquid completely interfaces with the solid surface.

i) Partially wetted Cassie surface

$A_{non\_wetted} = A_{non\_wetted\_cassie} = A_{n\_w\_c} = (\sqrt{3}*a^2/2) - (\pi*h_w^2*\tan^2\varphi)$

$\varphi = 13^o$, $\tan\varphi = .23086$, $a = 7*10^{-6}$ m

$\mathbf{A_{n\_w\_c} = (42.4352*10^{-12} - .16735*h_w^2)\ m^2}$

ii) Partially wetted Wenzel surface

$A_{non\_wetted} = A_{non\_wetted\_wenzel} = A_{n\_w\_w} = (\sqrt{3}*a^2/2) - (\pi*h_w^2*\tan^2\varphi)$

$\varphi = 32^o$, $\tan\varphi = .624869$, $a = 7*10^{-6}$ m

$\mathbf{A_{n\_w\_w} = (42.4352*10^{-12} – 1.22613*h_w^2)\ m^2}$

iii) Fully wetted Wenzel surface

$\mathbf{A_{non\_wetted} = 0}$

Fractional Areas

Let $f1 = A_{wetted} / A_{macro}$ and $f2 = A_{nonwetted} / A_{macro}$

1 - Cassie surface

$f1 = f1_{cassie\_partial} = f1_{c\_p} = A_{p\_w\_c} / A_m$

$A_{macro} = 42.4352*10^{-12}\ m^2$

$A_{p\_w\_c} = .743499*h_w^2\ m^2$

$f1_{c\_p} = .017532*10^{12}*h_w^2$

$f2 = f2_{cassie\_partial} = f2_{c\_p} = A_{n\_w\_c} / A_m$

$f2_{c\_p} = 1 – (.003943*10^{12}*h_w^2)$

2 - Wenzel surface

i) Partially wetted

$f1 = f1_{wenzel\_partial} = f1_{w\_p} = A_{p\_w\_w} / A_m$

$A_{macro} = 42.4352*10^{-12}\ m^2$

$A_{p\_w\_c} = 2.31369*h_w^2\ m^2$

$f1_{w\_p} = .05452*10^{12}*h_w^2$

$f2 = f2_{wenzel\_partial} = f2_{w\_p} = A_{n\_w\_w} / A_m$

$f2_{w\_p} = 1 – (.02889*10^{12}*h_w^2)$

ii) Fully wetted

$f1 = f1_{wenzel\_full} = f1_{w\_f} = A_{f\_w\_w} / A_m$

$A_{macro} = 42.4352*10^{-12}\ m^2$

$A_{f\_w\_w} = 96.8*10^{-12}\ m^2$

$f1_{w\_f} = 2.2811$

$f2 = f2_{wenzel\_full} = f2_{w\_f} = 0$

$f2_{w\_f} = 0$

Electrowetting equations – Energy based approach

A Cassie surface in Air

The modified solid-liquid interfacial tension for a drop fractionally wetting a structured surface can be given by *Eqn. 3.11*, which can be re-written as below.

$\gamma_{slm} = f2_{c\_p} * \gamma_{la} + f1_{c\_p} * (\gamma_{ls} – (½ * \varepsilon_0 * \varepsilon_r * V^2 / d))$……..……..…..……..…..3.12

d = thickness of the dielectric layer

ε_0 and ε_r –dielectric constants of air and the dielectric layer respectively

The interfacial tension of a solid liquid interface in air γ_{ls} can be expressed in terms of the basic Young's contact angle equation

$\gamma_{ls} = \gamma_{sa} - \gamma_{la}*\cos\theta_Y$……..……..……..……...3.13

$\cos\theta_Y$ - The contact angle of water on a flat Parylene-C surface in air

$\gamma_{sa} = 0$ (but we maintain the factor for the derivations)

Incorporating *Eqn. 3.13* in *Eqn. 3.12* we get

$((f1_{c\_p}*\gamma_{sa}) - \gamma_{slm})/\gamma_{la} = (f1_{c\_p}*\cos\theta_Y) - f2_{c\_p} + ((f1_{c\_p}* ½*\varepsilon_0*\varepsilon_r*V^2)/(d*\gamma_{la}))$

$\cos\theta_W = (f1_{c\_p}*\cos\theta_Y) - f2_{c\_p} + ((f1_{c\_p}*½*\varepsilon_0*\varepsilon_r*V^2)/(d*\gamma_{la}))$ …….……...3.14

$\eta = (½*\varepsilon_0*\varepsilon_r*V^2) / (d*\gamma_{la})$ – dimensionless value that represents the strength of the electrostatic energy in comparison to the surface tension.

$d = 1*10^{-6}$ m

$\varepsilon_r = 2.7$

$\gamma_{la} = 72.8*10^{-3}$ N/m

$\theta_Y = 90^o$ -Measured contact angle of water in Parylene-C in air

Substituting the constant values and fractional area expressions in *Eqn. 3.14* we get

$(.003943*10^{12} + .0028785*10^9*V^2)*h_w^2 + (-1-\cos\theta_W) = 0$……..…...3.15

The fractional wetting of a nanocone Cassie surface (as shown in *Fig. 3.21*) can be analyzed using *Eqn. 3.15*, which solves for the unknown wetted height.

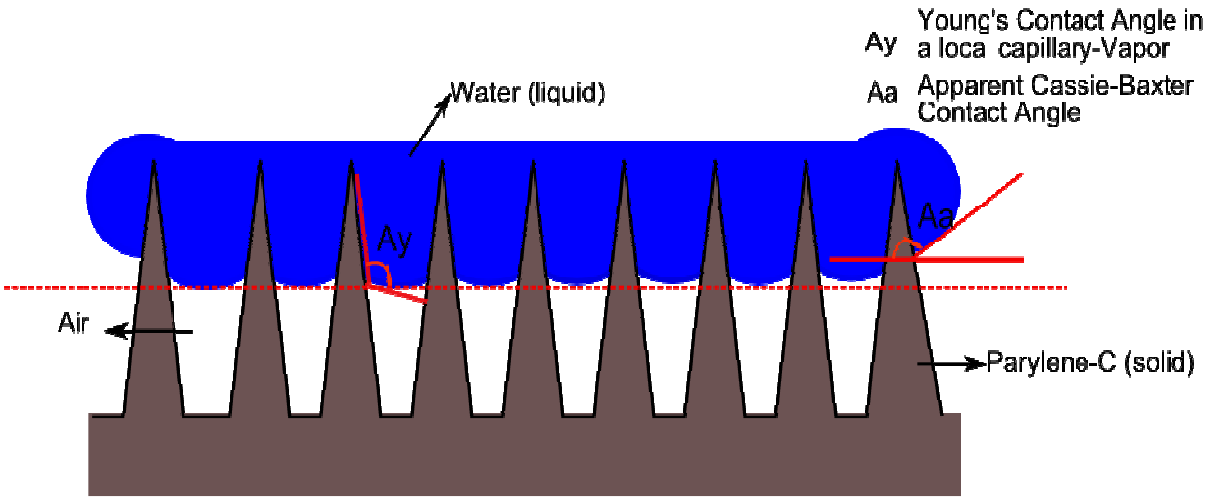

Fig. 3.21 – Cassie wetting profile of a single nanocone

If the surface produced the desired electrowetting behavior the fractional wetting and nonwetting areas can be calculated at each of the voltages. This fractional value can first help in knowing the increasing depth of penetration as the voltage is tuned up. The most useful and interesting observation that can be made is the transition from the fractionally wetted Cassie state to the fully wetted Wenzel state. The knowledge of the voltage values that induces this important transition is necessary for achieving a full-fledged contact angle change for a given voltage range.

In our case no noticeable electrowetting was observed on a drop of water on a Cassie surface surrounded by air. Hence we stop with the derived expression since the values of $\cos\theta_W$ are unknown.

A Wenzel surface in Air

A drop sitting on a Wenzel surface in air is expected to drop the surface completely. Hence such a surface does have liquid-air interfaces since the air pockets are filled with water in the Wenzel state.

Eqn. 3.11 can give the modified solid-liquid interfacial tension for a drop wetting a structured surface.

Since, $A_{nonwetted} = 0$

$f2 = 0$

$\gamma_{slm} = f1_{w\_f}*(\gamma_{ls} - (½*\varepsilon_0*\varepsilon_r*V^2/d))$……..…3.16

Here again, the interfacial tension of a solid liquid interface in air γ_{ls} can be expressed in terms of *Eqn. 3.13*.

$\gamma_{ls} = \gamma_{sa} - \gamma_{la}*\cos\theta_Y$

$\cos\theta_Y$ - The contact angle of water on a flat Parylene- C surface in air

Incorporating *Eqn. 3.13* in *Eqn. 3.16* we get

$((f1_{w\_f}*\gamma_{slm}) - \gamma_{sa})/\gamma_{la} = (f1_{w\_f}*\cos\theta_Y) + ((f1_{w\_f}*½*\varepsilon_0*\varepsilon_r*V^2)/(d*\gamma_{la}))$

$\cos\theta_W = (f1_{w\_f}*\cos\theta_Y) + ((f1_{w\_f}*½*\varepsilon_0*\varepsilon_r*V^2)/(d*\gamma_{la}))$ ……..……..……....3.17

$\theta_Y = 90^o$ - Measured contact angle of water in Parylene-C in air

Substituting the constant values and fractional area expressions in *Eqn. 3.17* we get

$\cos\theta_W = .37452*10^{-3}*V^2$ ……..……..…….3.18

Eqn. 3.18 gives the wetting behavior of a drop in a Wenzel surface in air. The contact angle change is affected by the constant value of surface roughness.

The theoretically calculated contact angles from *Eqn. 3.18* and the experimentally obtained values are shown in *Fig. 3.22*. We can see the effect of the roughness-driven hysteresis in the actual data when compared to the ideal one. The hysteresis causes early saturation and a poor contact angle change.

Planar surface in air

A plane surface in air simply follows the Lippman-Young relation since the surface is assumed to show no roughness. Hence for such a surface the wetted area is the same as the projected area.

$A_{nonwetted} = 0$, $A_{wetted} = A_{macro}$

Since, $A_{nonwetted} = 0$, f2 = 0

Since $A_{wetted} = A_{macro}$, f1 = 1

$\gamma_{slm} = \gamma_{ls} - (½*\varepsilon_0*\varepsilon_r*V^2/d))$……..……..…….3.19

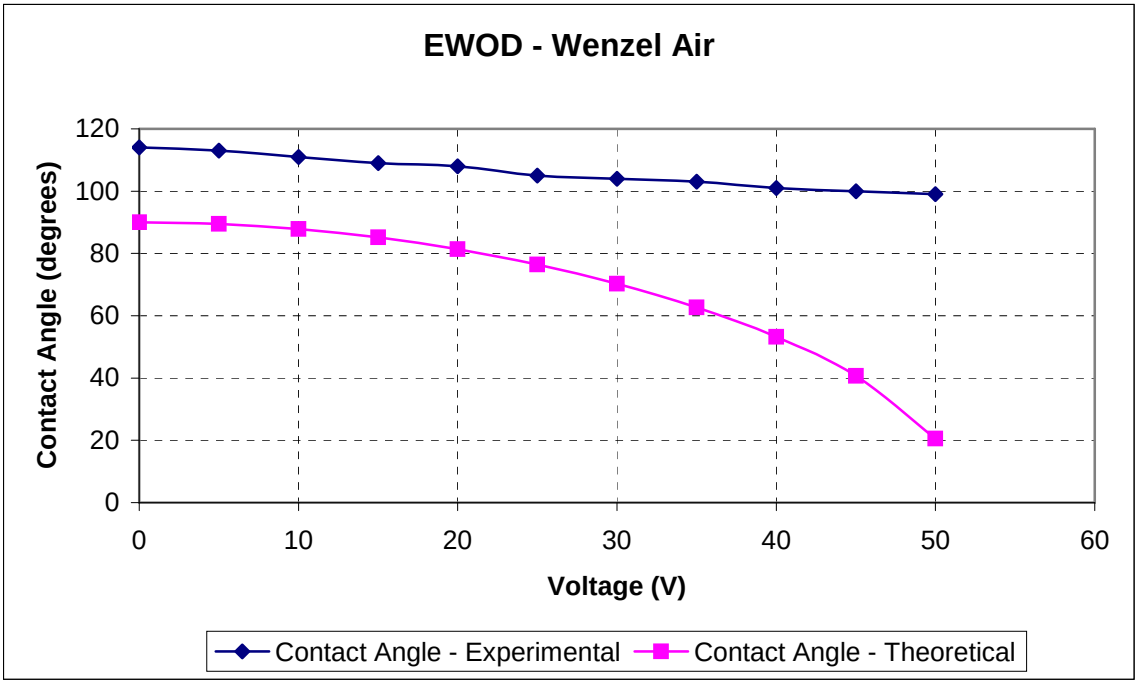

Fig. 3.22 – EWOD – Wenzel Air

Incorporating *Eqn. 3.13* in *Eqn. 3.19* we get the conventional Lippman-Young equation

$(\gamma_{sa}- \gamma_{slm})/\gamma_{la} = \cos\theta_Y + ((½*\varepsilon_0*\varepsilon_r*V^2)/(d*\gamma_{la}))$

$\cos\theta_W = \cos\theta_Y + ((½*\varepsilon_0*\varepsilon_r*V^2)/(d*\gamma_{la}))$ ……..3.20

$\theta_Y = 90^o$ -Measured contact angle of water in Parylene-C in air

Substituting the constant values and fractional area expressions in Eqn. 3.20 we get

$\cos\theta_W = .1641188*10^{-3}*V^2$ ……..3.21

We can compare *Eqn. 3.18* and *Eqn. 3.21* to notice the effect of roughness on the contact angle change for a fully wetted surface. The Wenzel surface has a reduced contact angle change due to the surface roughness factor given by f1.

The theoretically obtained contact angles from *Eqn. 3.21* and the experimental ones can be compared in *Fig. 3.23*. We can see that the experimental curve is closer to the theoretical one due to the reduced hysteresis unlike the Wenzel surface.

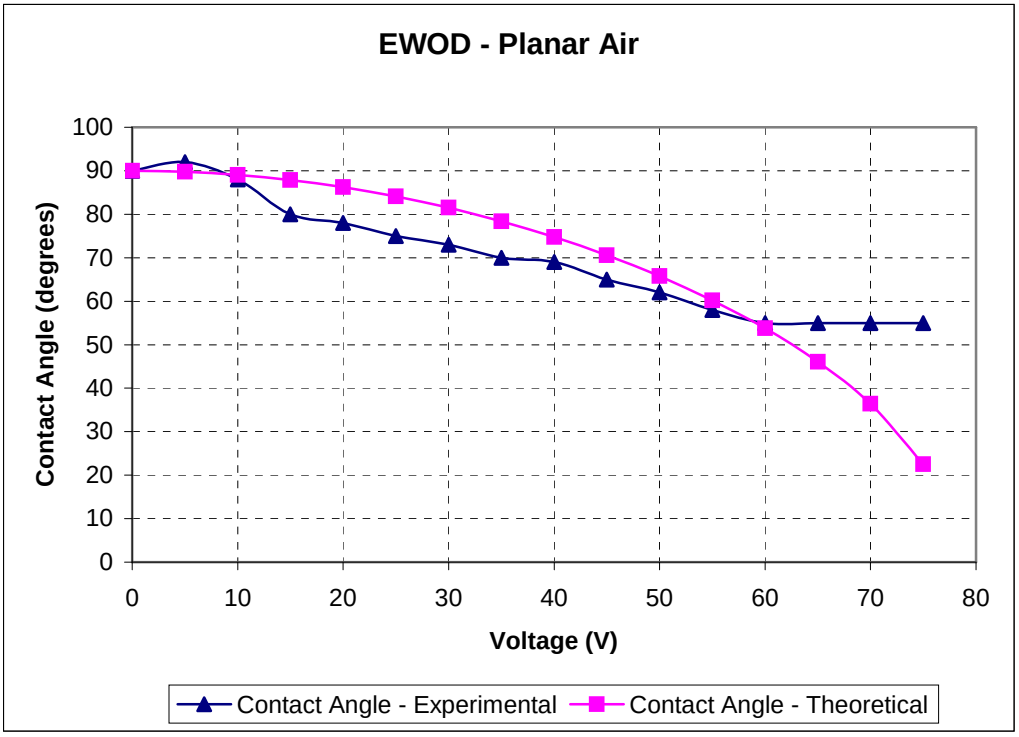

Fig. 3.23 –EWOD – Planar Air

A Cassie surface in Oil

A drop on a Cassie surface surrounded by oil is similar to the Cassie surface in air except that the oil replaces the air. Oil pockets are present between each of the nanocones instead of air. The partial wetting process involves the vertical downward force pushing of oil out of the nanocones till a condition is reached where the oil is completed pushed out of the nanocone regions resulting in complete wetting. This condition is equivalent to the Cassie to Wenzel transition of the drop undergoing electrowetting.

The modified solid-liquid interfacial tension for a drop fractionally wetting a structured surface in oil medium can be given by *Eqn. 3.12*, which can be re-written as below.

$\gamma_{slm} = f2_{c\_p}*\gamma_{lo} + f1_{c\_p}*(\gamma_{sl} - (½*\varepsilon_0*\varepsilon_r*V^2/d))$……..……..…….……..3.22

The interfacial tension of a solid liquid interface in oil γ_{ls} can be expressed in terms of the basic Young's contact angle equation

$\gamma_{ls} = \gamma_{so} - \gamma_{lo}*\cos\theta_Y$……..…….…….……..……..3.23

$\cos\theta_Y$ - The contact angle of water on a flat Parylene-C surface in oil

Incorporating Eqn. 3.23 in Eqn. 3.22 we get

$((f1_{c\_p}*\gamma_{so}) - \gamma_{slm})/\gamma_{lo} = (f1_{c\_p}*\cos\theta_Y) - f2_{c\_p} + ((f1_{c\_p}* ½*\varepsilon_0* \varepsilon_r*V^2)/(d* \gamma_{lo}))$

$\cos\theta_W = (f1_{c\_p}*\cos\theta_Y) - f2_{c\_p} + ((f1_{c\_p}*½*\varepsilon_0*\varepsilon_r*V^2)/(d*\gamma_{lo}))$ ……...…….….3.24

$d = 1*10^{-6}$ m

$\varepsilon_r = 2.7$

$\gamma_{lo} = 34*10^{-3}$ N/m

$\theta_Y = 132^o$ -Measured contact angle of water in Parylene-C in oil

$\cos\theta_Y = -.66913$

Substituting the constant values and fractional area expressions in Eqn. 3.25 we get

$(.066164*10^9*V^2 - .0077881*10^{12})*h_w^2 + (-1-\cos\theta_W) = 0$……..……..3.25

The fractional wetting of a nanocone Cassie surface in oil can be analyzed using *Eqn. 3.25*, which also solves for the unknown wetted height.

The fractional wetting area (*Fig. 3.24*) for a Cassie surface is 0 initially since the drop is not in contact with the spikes due to the presence of the oil. The fractional wetting area gradually increases with the contact angle change. In an ideal case a steady increase in fractional area till the Cassie to Wenzel transition occurs followed by complete wetting and an increased fractional area (which is equal to the roughness factor of the surface) must be observed. But in our case the

drop down of the fractional wetting area is seen only due to the effect of saturation, which occurs even before any transition thus not obeying the derived Lippman-Young equation.

A Wenzel surface in Oil

A drop sitting on a Wenzel surface in oil has a very high contact angle. This is due to the layer of oil present between the drop and the nanocone structure. Such a drop is considered to be in a Cassie-like state due to the very high contact angle. For such surface electrowetting involves the pushing of the oil out of the surface and allowing the water to completely wet it. In order to understand the nature of the Cassie-like to Wenzel transition we have assumed that the drop exhibits fractional wetting before it completely wets the surface.

The modified solid-liquid interfacial tension for a drop fractionally wetting a structured surface in oil medium can be given by *Eqn. 3.12*, which can be re-written as below.

$\gamma_{slm} = f2_{w\_p} * \gamma_{lo} + f1_{w\_p} * (\gamma_{sl} - (\frac{1}{2} * \varepsilon_0 * \varepsilon_r * V^2 / d))$ ……..……..…….……3.25

d = thickness of the dielectric layer

ε_0 and ε_r –dielectric constants of air and the dielectric layer respectively

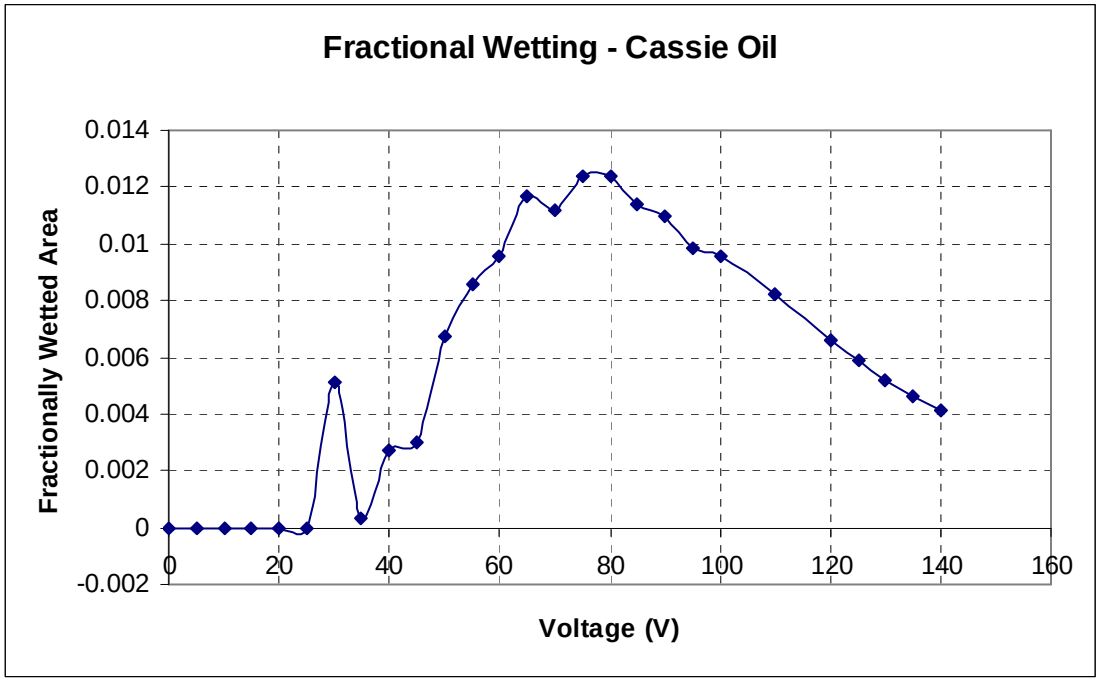

Fig. 3.24 – Fractional Wetting – Cassie Oil

The interfacial tension of a solid liquid interface in oil γ_{ls} can be expressed in terms of the basic Young's contact angle in *Eqn. 3.23*

$\gamma_{ls} = \gamma_{so} - \gamma_{lo}*\cos\theta_Y$

$\cos\theta_Y$ - The contact angle of water on a flat Parylene-C surface in oil

Incorporating *Eqn. 3.23* in *Eqn. 3.25* we get

$((f1_{w\_p}*\gamma_{so}) - \gamma_{slm})/\gamma_{lo} = (f1_{w\_p}*\cos\theta_Y) - f2_{w\_p} + ((f1_{w\_p} * ½*\varepsilon_0 * \varepsilon_r*V^2)/(d*\gamma_{lo}))$

$\cos\theta_W = (f1_{w\_p}*\cos\theta_Y) - f2_{w\_p} + ((f1_{w\_p}*½*\varepsilon_0*\varepsilon_r*V^2)/(d*\gamma_{lo}))$ ……..……..…3.26

$d = 1*10^{-6}$ m

$\varepsilon_r = 2.7$

$\gamma_{lo} = 34*10^{-3}$ N/m

$\theta_Y = 132^o$ -Measured contact angle of water in Parylene-C in oil

$\cos\theta_Y = -.66913$

Substituting the constant values and fractional area expressions in *Eqn. 3.26* we get

$(.019166*10^9*V^2 - .00749*10^{12})*h_w^2 + (-1-\cos\theta_W) = 0$……..…..……..3.27

The above equation solves for the fractional wetting height at various electrowetting voltages as the drop transitions from a Cassie-like state to a Wenzel state.

The fractional wetting areas for a Wenzel surface in oil are shown in *Fig. 3.25*. The negative fractional wetting area and the sudden shoot of the fractional wetting area are not realistic and can be attributed to mathematical errors in the computation.

Planar surface in oil

A plane surface in oil shows a very high initial contact angle due to the presence of oil. Such a surface can also be assumed to be in a Cassie-like state to begin with. But due to the absence of roughness there cannot be any possible fractional wetting and the drop only transition from a Cassie-like state to fully wetted state. During this transition the oil is completely pushed from the surface.

$A_{nonwetted} = 0$, $A_{wetted} = A_{macro}$

Since, $A_{nonwetted} = 0$, f2 = 0

Since $A_{wetted} = A_{macro}$, f1 = 1

$\gamma_{slm} = \gamma_{ls} - (½*\varepsilon_0*\varepsilon_r*V^2/d))$……..…….3.28

From *Eqn. 3.28* we get the conventional Lippman-Young equation in oil

$(\gamma_{sa} - \gamma_{slm})/\gamma_{lo} = \cos\theta_Y + ((½*\varepsilon_0*\varepsilon_r*V^2)/(d*\gamma_{lo}))$

$\cos\theta_W = \cos\theta_Y + ((½*\varepsilon_0*\varepsilon_r*V^2)/(d*\gamma_{lo}))$ ……..…….…….……..3.29

θ_Y = 132º -Measured contact angle of water in Parylene-C in oil

$\gamma_{lo} = 34*10^{-3}$ N/m

$\cos\theta_Y$ = -.66913

Substituting the constant values and fractional area expressions in *Eqn. 3.29* we get

$\cos\theta_W = -.66913 + (.3515*10^{-3}*V^2)$ ……..…….……..3.30

We can see from *Eqn. 3.30* that the presence of oil has improved the contact angle change. The theoretical and experimental values of the electrowetting on a planar surface in an ambient oil medium are compared in *Fig. 3.26*. We can see that the experimental curve saturates more quickly than the ideal one.

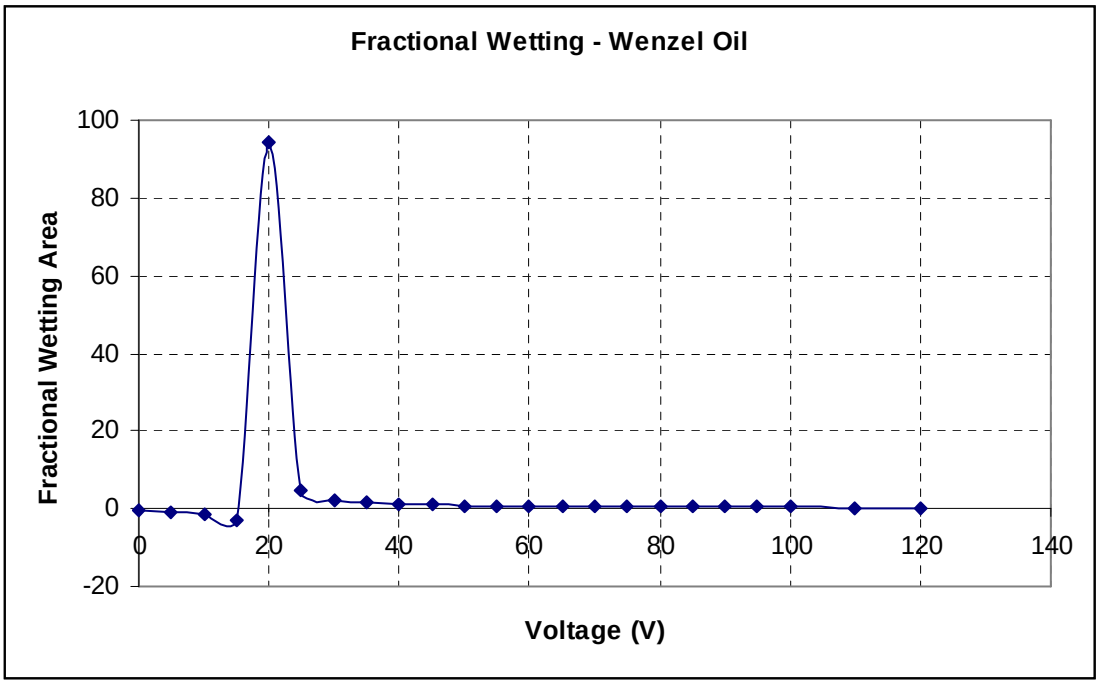

Fig. 3.25 – Fractional Wetting – Wenzel Oil

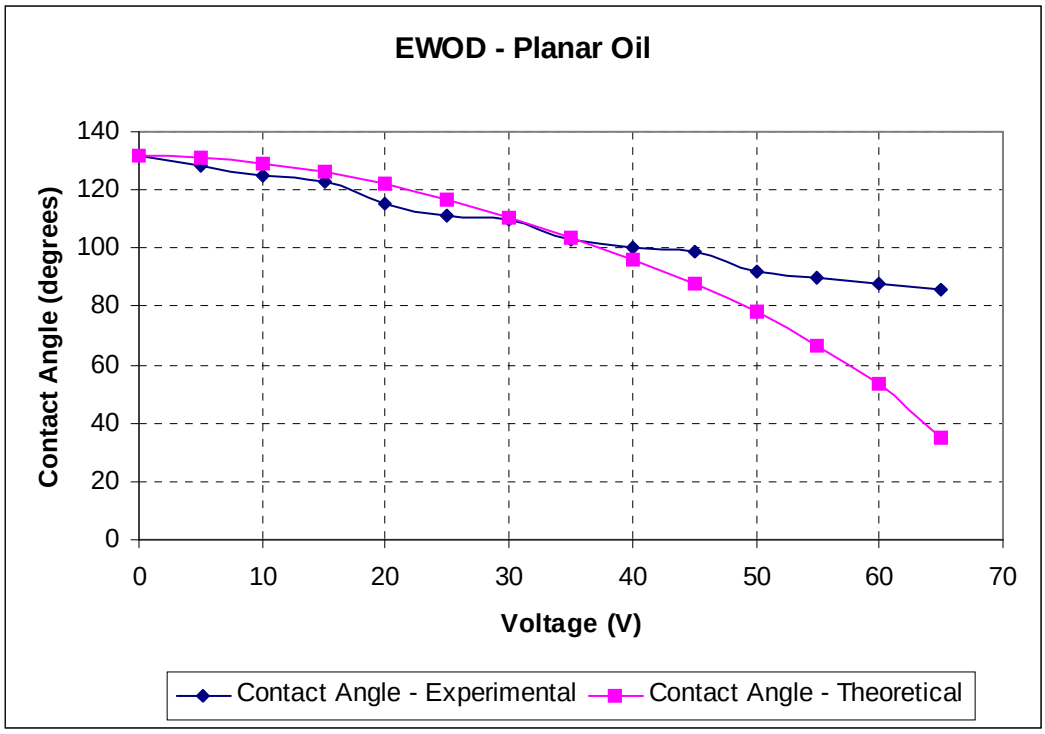

Fig. 3.26 – EWOD – Planar Oil

Performance Analysis

The results discussed in the previous section were analyzed.

Surface properties like interfacial tension and roughness determined factors like the initial contact angle and hysteresis. The breakdown voltage was determined by the dielectric strength and the quality of the dielectric coating on the surface. The current-voltage and the contact angle-voltage *(Fig. 3.27 and 3.28)* can help in estimating the optimal performance parameters.

Maximum Wetting: The maximum wetting is happens for devices that show maximum contact angle change. Oil has certainly helped boosting degree of contact angle change. Though all the wafers are coated with the same dielectric type and thickness, the Wenzel surface in oil showed maximum contact angle change especially when compared to the planar oil surface. Apart from the oil contributing to a reduced hysteresis the dielectric seems to have made a better coating on the Wenzel surface. The presence of a small amount of roughness must have helped the dielectric adhere better to the surface. The repeatability of the EW on this device also seemed to be good

on the Wenzel surface when compared to the planar surface. The Cassie surface shows a lower range accounted by the fractional electrostatic energy.

Reversibility: Degree of reversibility of the wetting and dewetting process is a direct implication of contact angle hysteresis. As already seen hysteresis is contributed by roughness. In the air medium as expected the planar surface shows slightly better reversibility than the Wenzel surface due to the effect of its smoothness. But the presence of oil drastically changes the effects of hysteresis. The Wenzel surface in oil showed complete reversibility when compared to the planar surface that showed only almost complete reversibility. The better reversibility here could again be attributed to a better quality dielectric coating.

Threshold Voltage: A fairly low threshold of ~3-5V was observed in all the wafers with and without oil except for the Cassie surface which seemed to have a higher threshold voltage. A low threshold voltage is very good for actuation and tapping the complete range of wetting on a given device. The lower value for the Cassie surface can be attributed to the greater resistance to the droplet moving down the oil and wetting the surface.

Breakdown Voltages: Breakdown was observed in some of the cases characterized by bubbling and a leakage current in the VI curve. The planar surface in oil seemed to have the lowest breakdown voltage of about 85V. Wenzel surfaces showed a higher breakdown voltage of about 120V. No breakdown was observed in the Cassie surfaces till 180V. Breakdown voltages also varied for different test sets for a given sample. This can be attributed to poor contact or a local damage of the dielectric. The quality of and strength of the dielectric film and the nature of voltage sweep can affect the breakdown process. A smooth sweep or step with delay seemed better than a sharp step up voltage.

Saturation Voltage: The effects of saturation were not observed in all the cases due to the occurrence of early breakdown. But the effects of saturation were most significant in the Cassie surface which seemed to have lower and lower contact angle change for higher voltages. The air based Planar and Wenzel surfaces showed more saturation that the oil-based wafers which showed a sharper decline in contact angle. We can say the presence of air around the droplet can enhance the saturation effects. But for the Cassie drop saturation is contributed by the fractional wetting design.

On the overall we can conclude that the oil based EW setup is advantageous when compared to an air based one in terms of achieving maximum wettability, minimum saturation and better reversibility. Oil also helps in preventing droplets from evaporating though it can cause contamination. The Wenzel surface in the air showed the best wetting characteristics and this can be attributed to ease of better dielectric coating on a rough surface. Since the Parylene was not very hydrophobic a larger range of contact angle change could not be attained. A qualitative comparison of the electrowetting parameters of the surfaces is done in *Table 3.8.*

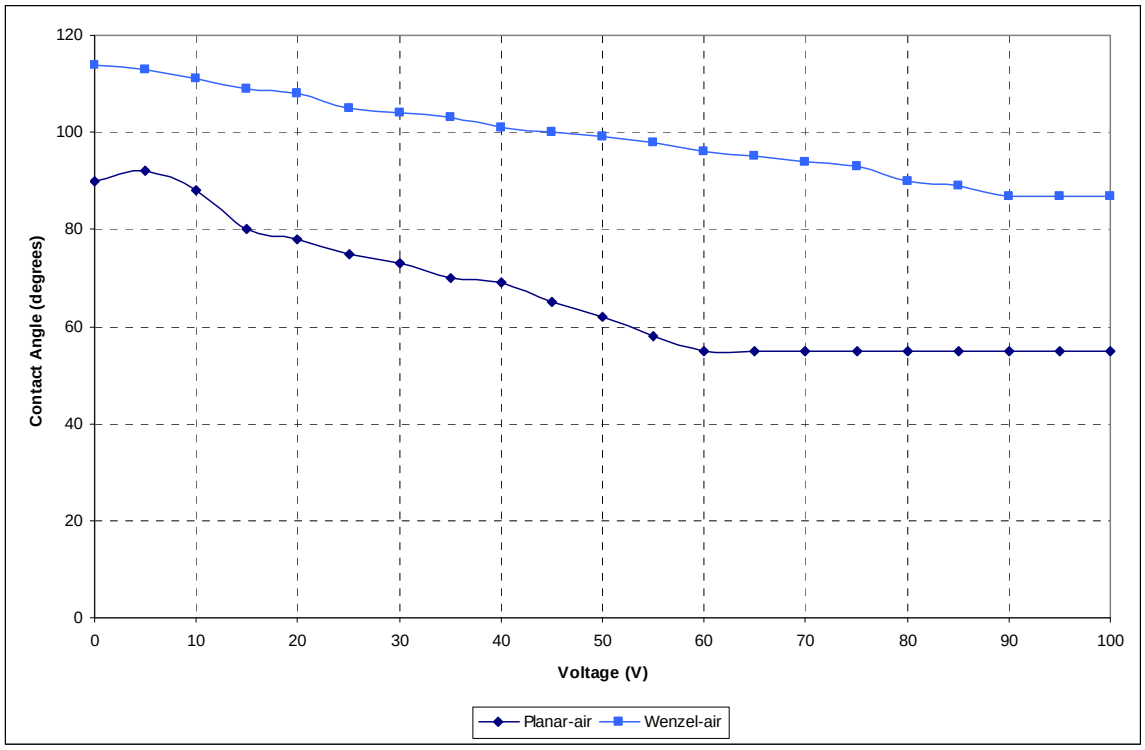

Fig. 3.27 – Contact Angle Vs Voltage for air based devices

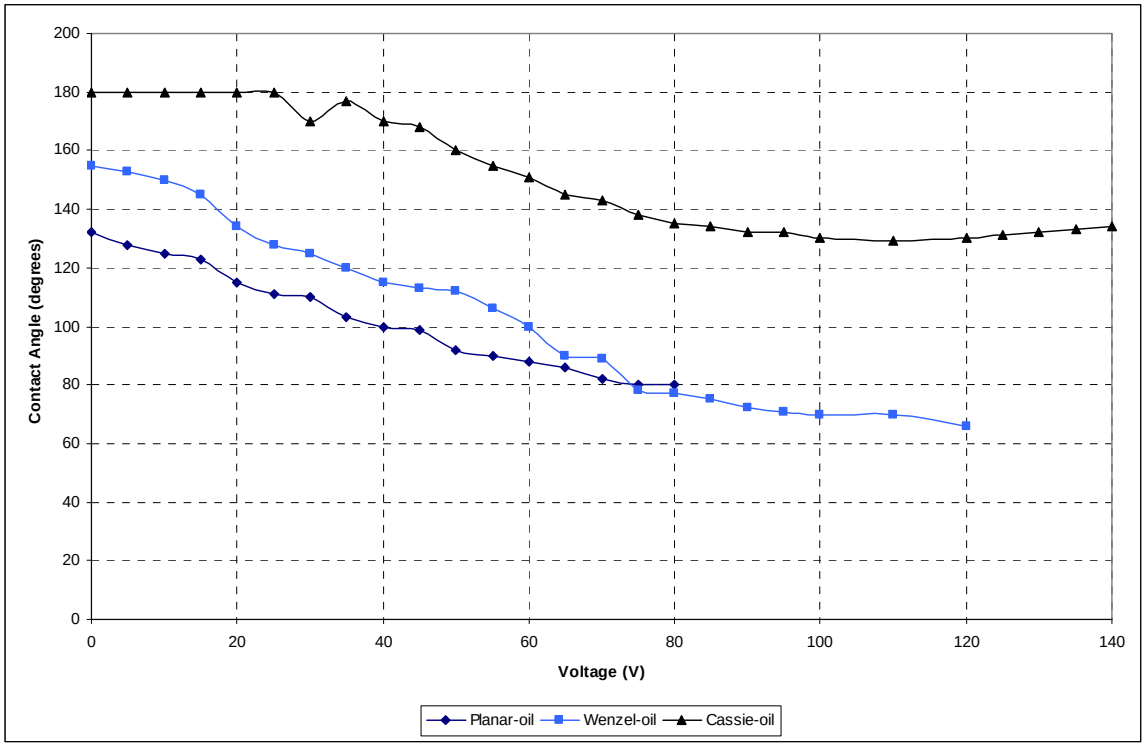

Fig. 3.28 – Contact Angle Vs Voltage for oil based devices

Table 3.8 – Qualitative comparison of EWOD substrates

Parameter	Plane-air	Plane-oil	Wenzel-air	Wenzel-oil	Cassie-oil
Degree of Wettability	Low	Moderate	Low	High	Very Low
Reversibility	Low	Moderate	Absent	Complete	Very Low
Threshold Voltage	Low	Low	Low	Low	High
Breakdown Voltage	Moderate	Low	Moderate	Moderate – High	Very High
Saturation	High	Low	High	Very Low	Very High

Chapter 5
Conclusions

Fabrication

In this thesis we have discussed in detail a novel method of fabricating nanocone glass arrays. The method uses glass as a raw material and a drawing and bundling process. Certain glasses can be easily melted together and can be drawn to the desired size. Glass properties like viscosity, thermal expansion, phase separation and interdiffusion proved to be critical to the selection criteria. The drawing and bundling chain of processes proved to be a very effective technique to obtain surfaces with replicated features. The effectiveness was both in terms of cost as well as efficiency. Commercially available glasses are cheaply available and the draw tower can be used to draw different types of glasses with a good degree of flexibility. Efficient bundling and a good control over the drawing and fusion process can help produce a defect free fusion bundle. Various drawing experiments resulted in wafers of extremely small feature sizes (lattice constant - 1.6μm, 7μm, 40μm). The lattice spacing was mainly controlled by the number of draws and the nature of the glass. The main limitation to going down to smaller feature sizes was set by the glass interdiffusion which dominates during the fusion process. Small lattice spacing proved to be very useful in producing a closely packed array of nanocones.

The next parameter of control was the aspect ratio. The difference in the etch rates of the two starting glasses and the chemistry of various HF based etching solutions were the two factors that produced the nanocone features. The additional phase separation caused by the heat treatment (during the fusion process) also resulted in an enhanced etch rate contrast. This was

inferred by the resulting difference in the observed aspect ratio and the calculated etch rate ratios for the various unprocessed core and cladding wafers.

The nature of the etching solutions and their relationship to the nanocone aspect ratio was analyzed. This analysis was done by calculating the activities of the constituent ions of each of the solutions. Other etching conditions like etching time and presence of ultrasonic agitation proved essential but not critical to obtaining a specific aspect ratio. Nanocones with aspect ratios of .4 - 13 were obtained. Such a process with good control over lattice constant, aspect ratio and tip sharpness has many potential applications. Like nanocones, arrays of nanoneedles, nanowires (glass drawn with metal wires), nanoholes (glass drawn with salt filled cores) can be fabricated. These nanostructured surfaces can be used for a wide range of applications like superhydrophobic surfaces, parallel needle probes for drug delivery and blood withdrawal, filters and field emitters. Altering the chemical composition of the glasses used can also produce features with interesting optical properties that might make them suitable for optical probe arrays.

Superhydrophobic behavior

The fabricated nanocone arrays were coated with hydrophobic material called the SAM (Self Assembled Monolayer) to produce superhydrophobic surfaces. In this thesis the nature and fundamentals of superhydrophobic behavior are discussed. The nanocone arrays were treated as potential superhydrophobic surfaces and were tested and characterized. The close packing of the sharp-tipped features and the high aspect ratio served as the crucial factors.

Simple tests for water-repellency showed increasing hydrophobic behavior with increasing contact angle. A more detailed characterization was done by testing the degree of hydrophobic-superhydrophobic behavior in each of the wafers by measuring the rolling and dynamic contact angles. The advancing and receding angles were measured by experimentally capturing images of the advancing and receding drops on each of the surfaces and fitting the drop shape to a theoretically determined one. A flat glass slide coated with SAM was also tested in the experiments.

The results were also predicted based on a surface tension model. This approach predicts the effects of the forces due to the surface tension of liquid which rests on the nanocone features. The forces may pull the droplet down causing complete wetting as seen in the Wenzel regime or it may reverse and push the droplet out of the nanocone features as seen in the Cassie regime. These forces are mainly controlled by the geometry of the nanocone surface and the Young's contact angle of the hydrophobic coating used. For a given hydrophobic coating (SAM) we have seen how changes in the geometry can affect the forces and the dominance of hysteresis.

A Wenzel-Cassie transition of wetting states as the aspect ratio of the nanocones was increased was predicted by the model and confirmed by the experimental observations. The agreement of the model with the experimental observations serves as a good lead to design optimal superhydrophobic surfaces. An appropriate choice of hydrophobic material and careful design of surface geometry can help producing highly tunable water-repellent surfaces.

Electrowetting on Dielectric

The next property that was explored on the nanocone arrays was electrowetting on dielectric. Two nanocone surfaces were chosen for the experiments. One was a low aspect ratio surface which was expected to exhibit the Wenzel wetting regime based on the model discussed and the other was a high aspect ratio surface expected to exhibit the Cassie wetting regime. A plane glass slide was also used for the experiments.

The surfaces were coated with gold (conducting layer) using an e-beam evaporation process. The evaporation technique gave better control on the amount of gold deposited and the uniformity of the coating when compared to the sputtering process. The dielectric used was Parylene-C which was deposited using a CVD technique. Parylene-C has superior dielectric properties than Teflon and can be coated conformally without pin-holes using the CVD technique. The EWOD experiments were carried out using both air and silicone oil as the ambient medium.

Images of the drops were captured at various step voltages and a rough estimation of the contact angle was done. Challenges in obtaining a conformal coating of dielectric/gold on the high aspect ratio features resulted in poor and inconsistent results on the Cassie surfaces. However, considerable wetting was observed on the Planar and Wenzel surfaces. A large contact angle change was observed with the Wenzel surface in the presence of oil. Oil proved to increase the effective contact angle change and reduce the hysteresis.

An energy based approach was used to model the electrowetting behavior on each of the surfaces both in the presence of air as well as oil as the ambient medium. The nature of electrowetting on dielectric was compared for the Wenzel, Cassie and Planar surface in both air and oil. The comparison was done by taking into consideration various phenomena like contact angle change, saturation, reversibility, threshold and breakdown. Next, the electrowetting equations for each of the surfaces were derived based on the feature geometry and properties of the ambient medium. A comparison of the experimental and theoretical wetting angles was done. The disagreement of the data was mostly due to hysteresis which cannot be accounted by theory. The Wenzel surface in oil was assumed to be in a Cassie-like state and the fractional wetting areas at various voltages were calculated.

A Cassie to Wenzel transition in the Cassie and Wenzel surface (in oil) was expected. However due to the effects of saturation the transition was not observed in the Cassie surface. Several improvements can be done both in the layering process to achieve conformal coatings of

the dielectric and conductive layer. The poor hydrophobic property of Parylene-C also reduced the initial contact angle of the surfaces. This can be improved by using a dielectric which is more hydrophobic than Parylene-C. The contact angle in here was estimated by a rough geometric plot on the drop. This may have led to inaccuracies which can be dealt by using the axisymmetric drop shape analysis to estimate the advancing and receding (wetting and dewetting) angles. More research will be needed in the future to fully understand the electrowetting behavior of water on these surfaces.

The study of electrowetting on dielectric on nanostructured superhydrophobic surfaces is useful for designing various lab-on-a chip devices that are based on hydrophobic substrates. The Cassie-Wenzel transition in electrowetting may serve as useful switching phenomena for microfluidic applications. The nanostructure increases the observed contact angle change relative to a planer surface when there is a transition from the Cassie to the Wenzel state. A low – voltage driven wetting process can be used for various droplet manipulation applications like mixing and separation.

Bibliography

Bibliography

[1.1] B. D'Urso, J. T. Simpson, and M. Kalyanaraman, "Nanocone Array Glass," Journal of Micromechanics and Microengineering, vol. 17, pp. 717-721, 2007.

[1.2] R.J. Tonucci, B. L. Justus, A. J. Campillo, and C. E. Ford, "Nanochannel Array Glass," Science, vol. 258, pp. 783-785, 1992.

[1.3] J. L. Wiza, "Microchannel Plate Detectors," Nuclear Instruments and Methods, vol. 162, pp. 587-601, 1979.

[1.4] C. A. Spindt, I. Brodie, L. Humphrey, and E. R. Westerberg, "Physical properties of thin-film field emission cathodes with molybdenum cones," Journal of Applied Physics, vol. 47, pp. 5248-5263, 1976.

[1.5] L. R. Baylor, V. I. Merkulov, E. D. Ellis, M. A. Guillorn, D. H. Lowndes, A. V. Melechko, M. L. Simpson, and J. H. Whealton, "Field emission from isolated individual vertically aligned carbon nanocones," Journal of Applied Physics, vol. 91, pp. 4602-4606, 2002.

[1.6] Z. Wang, C. Gu, J. Li, Z. and Cui, "A novel method for making high aspect ratio solid diamond tips," Microelectronic Engineering, vol. 78, pp. 353-358, 2005.

[1.7] T. Her, R. J. Finlay, C. Wu, S. Deliwala, and E. Mazur, "Microstructuring of silicon with femtosecond laser pulses," Applied Physics Letters, vol. 73, pp. 1673-1675, 1998.

[1.8] T. Baldacchini, J. E. Carey, M. Zhou, and E. Mazur, "Superhydrophobic Surfaces Prepared by Microstructuring of Silicon Using a Femtosecond Laser," Langmuir, vol. 22, pp. 4917-4919, 2006.

[1.9] H. Jansen, M. Boer, R. Legtenberg, and M. Elwenspoek, "The black silicon method: a universal method for determining the parameter setting of a fluorine-based reactive ion etcher in deep silicon trench etching with profile control," Journal of Micromechanics and Microengineering, vol. 5, pp. 115-120, 1995.

[1.10] C. Choi, and C. Kim, "Large Slip of Aqueous Liquid Flow over a Nanoengineered Superhydrophobic Surface," Physical Review Letters, vol. 96, pp. 066001, 2006.

[1.11] L. Cao, L. Laim, C. Ni, B. Nabet, and J. E. Spanier, "Diamond-Hexagonal Semiconductor Nanocones with Controllable Apex Angle," Journal of the American Chemical Society, vol. 127, pp. 13782-13783, 2005.

[1.12] W. Haller, D. H. Blackburn, F. E. Wagstaff, and R. J Charles, "Metastable Immiscibility Surface in the System Na_2O-B_2O_3-SiO_2," Journal of the American Ceramic Society, vol. 53, pp. 34-39, 1970.

[1.13] H. Doweidar, M. S. El-Shahawi, F. M. Reicha, H. A. Silim, and K. El-Egaly, "Phase separation and physical properties of sodium borosilicate glasses with intermediate silica content," Journal of Physics D: Applied Physics, vol. 23, pp. 1441-1446, 1990.

[1.14] S. Scholes, and F. C. F. Wilkinson, "Glassy Phase Seperation in Sodium Borosilicate Glasses" Discussions of the Faraday Society, vol. 50, pp. 175-181, 1970.

[1.15] M. Tomozawa, and T. Takamori, "Effect of Phase Seperation on HF Etch Rate of Borosilicate Glasses," Journal of the American Ceramic Society, vol. 60, pp. 301-304, 1977.

[1.16] G. A. C. M. Spierings, "Review – Wet chemical etching of silicate glasses in hydrofluoric acid based solutions," Journal of Materials Science, vol. 28, pp. 6261-6273, 1993.

[1.17] S. Verhaverbeke, I. Teerlinck, C. Vinckier, G, Stevens, R. Cartuyvels, and M. M. Heyns, "The Etching Mechanisms of SiO_2 in Hydrofluoric Acid," Journal of the Electrochemical Society, vol. 141, pp. 2852-2857, 1994.

[1.18] K. W. Kolasinski, "The Composition of Fluoride Solutions," Journal of the Electrochemical Society, vol. 152, pp. J99-J104, 2005.

[1.19] K. W. Kolasinski, "The Composition of Fluoride Solutions," Journal of the Electrochemical Society, vol. 152, pp. J99-J104, 2005, Erratum.

[1.20] B. D'Urso, J. T. Simpson, and M. Kalyanaraman, "Emergence of superhydrophobic behavior on vertically aligned nanocone arrays," Journal of Applied Physics, vol. 90, pp. 044102, 2007.

[1.21] An Introduction to Glass Science and Technology by James E. Shelby

[1.22] Glass Science by Robert H. Doremus

[2.1] L. Lacroix, M. Lejeune, L Ceriotti, M. Kormunda, T. Meziani, P. Colpo, and F. Rossi, "Tuneable rough surfaces: A new approach for elaboration of superhydrophobic films," Surface Science, vol. 592, pp. 182-188, 2005.

[2.2] Y. Cheng, and D. E. Rodak, "Is the lotus leaf superhydrophobic," Applied Physics Letters, vol. 86, pp. 144101, 2005.

[2.3] R.N. Wenzel, " Resistance of solid surfaces to wetting by water," Industrial and Engineering Chemistry, vol. 28, pp. 988-994, 1936.

[2.4] A. B. D. Cassie, and S. Baxter, "Wettability of porous surfaces," Transactions of the Faraday Society, vol. 40, pp. 546 551, 1944.

[2.5] Z. Yoshimitsu, A. Nakajima, T. Watanabe, and K. Hashimoto, "Effects of Surface Structure on the Hydrophobicity and Sliding Behavior of Water Droplets,"Langmuir, vol. 18, pp. 5818-5822, 2002.

[2.6] B. He, N. A. Patankar, and J. Lee, "Multiple Equilibrium Droplet Shapes and Design Criterion for Rough Hydrophobic Surfaces," Langmuir, vol. 19, pp. 4999 – 5003, 2003.

[2.7] L. Zhu, Y. Feng, X. Ye, and Z. Zhou, "Tuning wettability and getting superhydrophobic surface by controlling

surface roughness with well-designed microstructures," Sensors and Actuators A, vol. 130, pp. 595 – 600, 2006.

[2.8] T. N. Krupenkin, J. A. Taylor, T. M. Schneider, and S. Hang, "From Rolling Ball to Complete Wetting: The Dynamic Tuning of Liquids on Nanostructured Surfaces," American Physical Society, Langmuir, vol. 20, pp. 3824 –3827, 2002.

[2.9] M. J. Pellerite, E. J. Wood, and V. W. Jones, "Dynamic Contact Angle Studies of Self-Assembled Thin Films from Fluorinated Alkyltrichlorosilanes," Journal of Physical Chemistry B, vol. 106, pp. 4746-4754, 2002.

[2.10] L. M. Lander, L. M Siewierski, W. J. Brittain, and E. A. Wolger, "A Systematic Comparison of Contact Angle Methods," Langmuir, vol. 9, pp. 2237-2239, 1993.

[2.11] L. Gao, and T. J. McCarthy, "Contact Angle Hysteresis Explained," Langmuir, vol. 22, pp. 6234-6237, 2006.

[2.12] M. Miwa, A. Nakajima, A. Fujishima, K. Hashimoto, and T. Watanabe, "Effects of the Surface Roughness on Sliding Angles of Water Droplets on Superhydrophobic Surfaces," Langmuir, vol. 16, pp. 5754-5760, 2000.

[2.13] Y. Rotenburg, L. Boruvka, and A. W. Neumann, "Axisymmetric Drop Shape Analysis," Journal of Colloidal and Interfacial Science, vol. 93, pp. 169, 1983.

[2.14] B. D. D'Urso, "Superhydrophobic Nanopost Glass: Surface Tension Model," 2004

[2.15] N. A. Patankar, "Transition between Superhydrophobic States on Rough Surfaces," Langmuir, vol. 20, pp. 7097-7102, 2004.

[2.16] A. Lafuma, and D. Quere, "Superhydrophobic States," Nature Materials, vol. 2, pp. 457 – 460, 2003.

[3.1] M. G. Pollack, A. D. Shenderov, and R. B. Fair, "Electrowetting-based actuation of droplets for integrated microfluidics," Lab on a Chip, vol. 2, pp. 96-101, 2002.

[3.2] R. B. Fair, A. Khlystov, V. Srinivasan, V. K. Pamula, and K. N. Weaver, "Integrated chemical/biochemical sample collection, pre-concentration, and analysis on a digital microfluidic lab-on-a-chip platform," Lab-on-a-Chip: Platforms, Devices, and Applications, Conf. 5591, SPIE Optics East, Philadelphia, Oct. 25-28, 2004.

[3.3] V. Srinivasan, V. K. Pamula, and R. B. Fair, "An Integrated Digital Microfluidic Lab-on-a-chip for Clinical Diagnostics on Human Physiological Fluids," Lab on a Chip, vol. 4, pp. 310-315, 2004.

[3.4] J. Lee, H. Moon, J. Fowler, T. Schoellhammer, and C. Kim, "Electrowetting and electrowetting-on-dielectric for microscale liquid handling," Sensors and Actuators A, vol. 95, pp. 259 – 268, 2002.

[3.5] F. Mugele, and J. Baret, "Electrowetting: from basics to applications," Journal of Physics: Condensed Matter, vol. 17, pp. R705-R774, 2005.

[3.6] V. Bahadur, and S. V. Garimella, "An energy-based model for electrowetting-induced droplet actuation," Journal of Micromechanics and Microengineering, vol. 16, pp. 1494-1503, 2006.

[3.7] T. B. Jones, "An electromechanical interpretation of electrowetting," Lab on a Chip , vol. 4, pp. 310-315, 2004.

[3.8] F. Saeki, J. Baum, H. Moon, J. Yoon, C. Kim, and R. L. Garrell, "Electrowetting on Dielectrics (EWOD): Reducing Voltage Requirements for microfluidics," Polymeric Materials: Science and Engineering, vol. 85, pp. 12 – 13, 2001.

[3.9] H. Moon, S. K. Cho, R. L. Garrell, and C. Kim, "Low voltage electrowetting-on-dielectric," Journal of Applied Physics, vol. 92, pp. 4080 – 4087, 2002.

[3.10] J. Berthier, P. Dubois, P. Clementz, and P. Claustre, C. Peponnet, and Y. Fouillet, "Actuation potentials and capillary forces in electrowetting based microsystems ," Sensors and Actuators A, vol. 134, pp. 471 – 479, 2007.

[3.11] A. Quinn, R. Sedev, and J. Ralston, "Contact Angle Saturation in Electrowetting," Journal of Physical Chemistry B, vol. 109, pp. 6268-6275, 2005.

[3.12] G. McHale, M. I. Newton, and D. Herbertson, "Electrowetting on super-hydrophobic surfaces," Fifth International Symposium on Contact Angle, Wettability and Adhesion, Toronto, Canada, 2006.

[3.13] M. I. Newton, D. L. Herbertson, S.J. Elliot, N. J. Shirtcliffe, and G. McHale, "Electrowetting of liquid marbles," Journal of Physics D: Applied Physics, vol. 40, pp. 20-24, 2007.

[3.14] A. Torkkeli, J. Saarilahti, A. Haara, A. Harma, H. Soukka, and P. Tolonen "Electrostatic transportation of water droplets on superhydrophobic surfaces," The 14th IEEE International Conference on MEMS, pp. 475-478, 2001.

[3.15] A. Torkkeli, "Droplet microfluidics on a planar surface," Ph.D. Dissertation, Helsinki University of Technology, Espoo, Finland, VTT Publication No. 504, 2003.

Vita

Meenaa Kalyanaraman was born in Coonoor, India on June 26, 1982. After graduating from Vidyodaya Girls Higher Secondary School, Chennai, India she attended Vellore Institute of Technology, Vellore, India where she received her Bachelor of Engineering degree in Electronics and Instrumentation in 2003. She worked as a Programmer Analyst in Cognizant Technology solutions, Chennai, India till 2005. In January 2006 she joined the Masters program in Electrical Engineering at the University of Tennessee, Knoxville, Tennessee. She worked as a graduate research assistant for Dr. Brian R. D'Urso at Oak Ridge National labs, Oak Ridge, Tennessee. She is looking forward to joining a research group in Oak Ridge National labs following her graduation.